Scanning Tunneling Microscopy and X-ray Diffraction of Charge Density Wave Materials and the Rubidium Isotope Effect in Superconducting Rb_3C_{60}

by

Brian D. Burk

B.S. (California Institute of Technology) 1986

A dissertation submitted in partial satisfaction of the requirements for the degree of

DOCTOR OF PHILOSOPHY

in

PHYSICS

in the

GRADUATE DIVISION

of the

UNIVERSITY of CALIFORNIA at BERKELEY

Committee in charge:

Professor Alex Zettl, Chair

Professor John Clarke

Professor Neil Bartlett

1994

The dissertation of Brian D. Burk is approved:

Chair — Date: APRIL 27, 1994

Date: April 27, 1994

Date: April 29, 1994

University of California at Berkeley

1994

Scanning Tunneling Microscopy and X-ray Diffraction of Charge Density Wave Materials and the Rubidium Isotope Effect in Superconducting R_3C_{60}

by

Brian D. Burk

Abstract

Scanning Tunneling Microscopy and X-ray Diffraction of Charge Density Wave Materials and the Rubidium Isotope Effect in Superconducting Rb_3C_{60}

by

Brian D. Burk

Doctor of Philosophy in Physics

University of California at Berkeley

Professor Alex Zettl, Chair

We image the surfaces of $K_{0.3}MoO_3$ and $Rb_{0.3}MoO_3$ with scanning tunneling microscopy (STM) above and below the charge density wave (CDW) transition temperature (T_p). Surprisingly, below T_p real space and Fourier transformed images show no evidence of CDW modulation, suggesting a relatively small CDW amplitude at the sample surface. Furthermore, the lattice images that we obtained below T_p are unaffected by the sliding of the CDW.

With STM and x-ray diffraction we investigate the CDW domain structure of 1T-TaS_2 in the nearly commensurate (NC), triclinic (T), and incommensurate (I) phases. Fourier transformed STM images of the NC phase show fine satellite structure surrounding CDW peaks. The satellite structure confirms that the apparent domain-like modulation seen in real space images results from a true domain structure rather than from a moiré pattern. STM images of the T phase indicate a surface striped domain pattern that is contrary to the previously reported stretched-honeycomb domain structure

for the crystal bulk. In the T phase our x-ray diffraction measurements of CDW wave vectors and examination of fine satellite structure surrounding CDW peaks conclusively demonstrate that the bulk domain pattern is striped. We find that the bulk and surface domain structures are identical. X-ray diffraction of the I phase reveals weak satellites near CDW peaks. The satellite structure indicates a short wavelength, periodic amplitude and phase modulation of the CDW in a case where the CDW is far from commensurability.

We measure the resistive superconducting transition temperature in C_{60} single crystals intercalated with isotopically pure ^{87}Rb and ^{85}Rb and with natural abundance rubidium. We obtain a rubidium isotope effect exponent of $\alpha_{Rb} = -0.028 \pm 0.036$, a result which implies that the Rb-C_{60} optic phonons play at most a minor role in the pairing mechanism of Rb_3C_{60}.

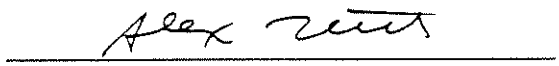

To Mara, with love

Table of Contents

List of Figures

List of Tables

Acknowledgements

First I would like to thank my thesis advisor, Professor Alex Zettl, for the many years of support and encouragement he has given me. He provided an inexhaustible stream of interesting projects and helpful suggestions as well as a stimulating and cooperative laboratory environment. Perhaps most importantly, he gave me the opportunity to fail and then succeed, and the freedom and courage to pursue my own ideas. Also I thank Professor John Clarke for his extended and extremely fruitful collaboration on the scanning tunneling microscopy projects that form the backbone of this thesis. His patience, interest, and guidance are greatly appreciated.

Next I would like to thank my co-worker, Ruth Thomson, who first introduced me to the field of scanning tunneling microscopy. The bulk of the work described in this thesis comes from our collaboration, and she has generously provided me with many figures for this thesis. Out of our daily conversations grew many of the ideas presented in the following chapters. Also, I would like to thank Mark Shattuck and Mats Gustafsson for many helpful discussions about scanning tunneling microscopy.

Among the great number of people who have helped me, two people deserve acknowledgement for their concrete contributions. Fred Hollander provided expert assistance with the x-ray diffraction work presented in this thesis, and Michael Fuhrer produced most of the C_{60} crystals for the rubidium isotope effect experiment discussed in chapter 8.

When I first joined the Zettl lab, Phil Parilla and Mike Crommie gave freely of their time to explain the basic physics of their projects and to teach me to perform the most basic measurements. I am grateful for their instruction. My office mate, Storrs Hoen, and I discussed our ideas and problems concerning every project that either he or I worked on. His insightful questions and useful suggestions aided me enormously. Everyone in the Zettl group has helped me in some way, and I thank them all.

Vita

February 13, 1964	Born in Kansas City, Mo.
September 1982 to June 1986	B.S. in Applied Physics at the California Institute of Technology
August 1986 to May 1994	Teaching and research assistant, Department of Physics, University of California at Berkeley

Publications

1. William K. Marshall, B. Burk. Calculating Optical-Transmitter Radiation Patterns. NASA Tech Briefs **12**, 56 (1988)

2. B. Burk, R.E. Thomson, A. Zettl, and J. Clarke. Charge-density-wave domains in 1T-TaS_2 observed by satellite structure in scanning tunneling microscopy images. Phys. Rev. Lett. **66**, 3040 (1991)

3. U. Walter, R.E. Thomson, B. Burk, M.F. Crommie, A. Zettl, and J. Clarke. Scanning tunneling microscopy of the blue bronzes $(Rb,K)_{0.3}MoO_3$. Phys. Rev. B **45**, 11474 (1992)

4. S. Hoen, B. Burk, A. Zettl, and M. Inui. Metastable length states of a random system: TaS_3. Phys. Rev. B **46**, 1874 (1992)

5. B. Burk, R.E. Thomson, J. Clarke, and A. Zettl. Surface and bulk charge density wave structure in 1T-TaS_2. Science **257**, 362 (1992)

6. B. Burk and A. Zettl. Lattice-induced modulation of a charge density wave far from commensurability. Phys. Rev. B **46**, 9817 (1992)

7. R.E. Thomson, B. Burk, A. Zettl, and J. Clarke. Scanning tunneling microscopy of the charge-density-wave structure in 1T-TaS_2, (accepted for publication in Phys. Rev. B)

8. B. Burk, A. Zettl. Rubidium isotope effect on superconductivity in Rb_3C_{60}. (submitted to Phys. Rev. Lett.)

Chapter 1

Introduction and motivation

1.1 Organization of thesis

The majority of the work described in this thesis consists of a series of scanning tunneling microscopy (STM) and x-ray diffraction investigations of charge density wave (CDW) structure in the blue bronzes and 1T-TaS_2. Chapter 2 serves as a general introduction to the STM work found in chapters 3, 5, 6, and 7. In chapter 2 we briefly summarize STM tunneling theory and then state the elements of our STM experimental procedure that are common to all of our investigations. In chapter 3 we investigate the CDW in blue bronze with STM. Chapter 4 describes the crystal and CDW structure in 1T-TaS_2, summarizes the McMillan theory of CDW domains[1], and introduces important concepts in applying STM and x-ray diffraction to CDW domain study. Chapter 4 provides the background for the investigations of CDW domain structure in 1T-TaS_2 presented in chapters 5, 6, and 7. Finally, chapter 8 stands apart from the other chapters. In chapter 8 we present a determination of the rubidium isotope effect in superconducting Rb_3C_{60}.

1.2 STM of blue bronze

Our motivation for the STM study of the blue bronzes was two fold. First, STM probes only the surface states and so can detect whether the outer most sample layer supports a CDW. Since the alkali intercalant atoms that donate electrons to the conduction band are possibly distributed differently on the surface layer than in the bulk, the surface layer might not support a CDW. Grazing incidence x-ray diffraction has shown that the CDW propagates to within 20 Å of the surface[2]. However, no attempts to observe the CDW on the surface in blue bronze by STM were reported when we began our effort to see whether the CDW propagates to the surface. Second, if the surface were

found to support a CDW, blue bronze would provide an excellent system in which to use STM to observe directly the CDW depinning as voltage across the sample is swept through the CDW conduction threshold voltage. There have been suggestions that a CDW might be pinned strongly at the sample surface[3-5] and therefore exhibit a different voltage threshold for CDW conduction than the bulk. In principle STM could settle this issue conclusively, thus making an important contribution to understanding CDW dynamics near surfaces.

1.3 STM and x-ray diffraction of CDW domain structure in 1T-TaS_2

The notion of competing periodicities finds application to many physical systems, including solid-solid interfaces, defect structure, ferroelectrics[6], adsorbate monolayers on semiconductor surfaces[7], mass density waves in intercalated graphite compounds[8], and CDWs[9]. In the case of CDWs, the periodicity of the density wave is in general dictated by the details of the Fermi surface of the host material and unrelated to the underlying lattice structure. CDW-lattice interactions can, however, modify the CDW structure[1].

The layered compound 1T-TaS_2 is a two-dimensional conductor which supports a rich spectrum of CDW phases[10,11]. We investigate the effect of CDW-lattice interactions on the nearly commensurate (NC), triclinic (T), and incommensurate (I) phases. For the NC phase Nakanishi and Shiba have predicted[12-14] that the CDW-lattice interaction distorts the CDW into a periodically modulated domain structure. The motivation for our STM study of the NC phase was to compare their theory to the domain structure seen by STM on the surface and to provide confirmation of the model independent of the data upon which it was based. For the T and I phases there is no detailed theoretical treatment analogous to the Nakanishi and Shiba theory for the NC phase. Our motivation for investigating these phases was to see whether the CDW-lattice interaction produced domain-like modulation of the CDW in the T and I phases as well. Additionally in the T phase we check how closely surface and bulk CDW structures agree in order to determine

whether the abrupt termination of the crystal lattice at the surface causes a serious perturbation to the CDW. Our work tests whether the CDW-lattice interaction breaks the translational invariance of the incommensurate CDW in the I phase where the CDW is far from commensurability.

1.4 The rubidium isotope effect in Rb_3C_{60}

The A_3C_{60} (A = K, Rb) compounds are an exciting new group of superconductors with relatively high transition temperatures. Several superconducting mechanisms have been proposed including electronic[15,16] and various phonon[17-22] models. Determination of the isotope effect can severely constrain the range of viable models. All but one of the isotope effect experiments prior to our work measured the carbon isotope effect[23-27]. While carbon phonon modes would seem to be the most likely mechanism, a careful determination of the rubidium isotope effect would provide a direct measure of any contribution by rubidium-C_{60} phonon modes. The large experimental uncertainty of the only rubidium isotope effect measurement[28] prior to our work led to only weak constraints on viable models. Our goal was to measure the rubidium isotope effect with sufficient accuracy to distinguish between phonon mechanisms incorporating carbon modes only and phonon mechanisms with significant coupling to both carbon modes and rubidium-C_{60} modes.

References

1. W. L. McMillan, Phys. Rev. B **14**, 1496 (1976).
2. X.-M. Zhu, R. Moret, H. Zabel, *et al.*, Phys. Rev. B **42**, 8791 (1990).
3. P. J. Yetman and J. C. Gill, Solid State Commun. **62**, 201 (1987).
4. J. McCarten, M. Maher, T. L. Adelman, *et al.*, Phys. Rev. Lett. **63**, 2841 (1989).
5. J. C. Gill, Europhys. Lett. **11**, 175 (1990).
6. H. Bestgen, Solid State Commun. **58**, 197 (1986).
7. A. B. McLean, R. M. Feenstra, A. Taleb-Ibrahimi, *et al.*, Phys. Rev. B **39**, 12925 (1989).
8. R. Clarke, J. N. Gray, H. Homma, *et al.*, Phys. Rev. Lett. **47**, 1407 (1981).
9. C. H. Chen, J. M. Gibson and R. M. Fleming, Phys. Rev. Lett. **47**, 723 (1981).
10. S. C. Bayliss, A. M. Ghorayeb and D. R. P. Guy, J. Phys. C. **17**, L533 (1984).
11. C. B. Scruby, P. M. Willaims and G. S. Parry, Philos. Mag. **31**, 255 (1975).
12. K. Nakanishi and H. Shiba, J. Phys. Soc. Jpn. **43**, 1893 (1977).
13. K. Nakanishi, H. Takatera, Y. Yamada, *et al.*, J. Phys. Soc. Jpn. **43**, 1509 (1977).
14. K. Nakanishi and H. Shiba, J. Phys. Soc. Jpn. **53**, 1103 (1984).
15. S. Chakravarty, M. P. Gelfand and S. Kivelson, Science **254**, 970 (1991).
16. S. Chakravarty, S. A. Kivelson, M. K. Salkola, *et al.*, Science **256**, 1306 (1992).
17. C. M. Varma, J. Zaanen and K. Raghavachari, Science **254**, 989 (1991).
18. R. A. Jishi and M. S. Dresselhaus, Phys. Rev. B **45**, 2597 (1992).
19. M. Schluter, M. Lannoo, M. Needels, *et al.*, Phys. Rev. Lett. **68**, 526 (1992).
20. F. C. Zhang, M. Ogata and T. M. Rice, Phys. Rev. Lett. **48**, 3452 (1991).
21. G. H. Chen, Y. J. Guo, N. Karasawa, *et al.*, Phys. Rev. B **48**, 13959 (1993).
22. I. I. Mazin, O. V. Dolgov, A. Golubov, *et al.*, Phys. Rev. B **47**, 538 (1993).
23. C.-C. Chen and C. M. Lieber, J. Am. Chem. Soc. **114**, 3141 (1992).
24. A. P. Ramirez, A. R. Kortan, M. J. Rosseinsky, *et al.*, Phys. Rev. Lett. **68**, 1058 (1992).

25. T. W. Ebbesen, J. S. Tsai, K. Tanigaki, *et al.*, Nature **355**, 620 (1992).

26. A. A. Zakhidov, K. Imaeda, D. M. Petty, *et al.*, Phys. Lett. A **164**, 355 (1992).

27. Auban-Senzier, G. Quirion, D. Jerome, *et al.*, Synth. Met. **56**, 3027 (1993).

28. T. W. Ebbesen, J. S. Tsai, K. Tanigaki, *et al.*, Physica C **203**, 163 (1992).

Chapter 2

STM background

2.1 Introduction

In the work that we describe in chapters 3, 5, 6, and 7, we use STM to investigate CDW materials. Here we provide a brief summary of STM tunneling theory. Also we describe the STM head and variable temperature operation. The experimental procedure for the STM operation is essentially identical in the work described in chapters 3, 5, 6, and 7, and we state it here. Finally we explain the apodization of STM images before Fourier transformation that is applied repeatedly in chapters 3, 5, 6, and 7. As we discuss in the following section, STM probes electronic structure of sample states with energy near the Fermi energy[1,2]. This property of STM makes it ideally suited to CDW electronic structure investigation[3].

When a normal metal undergoes a CDW transition, an energy gap is introduced into the electronic states of the conduction band, and states with wave vector k_F and $-k_F$ are mixed to produce a CDW modulation with wave vector $2k_F$ where k_F is the Fermi wave vector[4]. An STM tip at negative bias voltage, V_{bias}, with respect to a CDW sample will allow electrons to tunnel from the tip into the unoccupied states below the gap. These states just below the gap are precisely the states which exhibit most strongly the $2k_F$ CDW modulation[4].

2.2 STM theory

We summarize briefly Tersoff and Hamann's[1,2] simple STM tunneling theory so that we may explain how to interpret current and topographic STM images. Tersoff and Hamann begin their analysis with the Bardeen tunneling formula[5]. To evaluate the formula one requires only the wave functions of the tip and surface, Ψ_μ and Ψ_ν, and the eigenenergies of the states μ and ν, E_μ and E_ν. Tersoff and Hamann evaluate the

tunneling formula for an "ideal" tip. The tip contains only a single state, μ, and that state is far more localized than the length scale of variations in Ψ_ν. Furthermore the potential of the tip is localized so that it does not perturb the surface. For this ideal tip, the tip properties can be taken out of the problem, and they find for the tunneling current

$$I(r) \propto \sum_{\nu} |\Psi_\nu(r)|^2, \qquad E_F < E_\nu < E_F + e|V_{bias}| \text{ , } (V_{bias} \text{ negative}), \tag{2.1}$$

where $I(r)$ is the tunnel current, $\Psi_\nu(r)$ is the surface wave function at energy E_ν evaluated at the tip position, r, and E_F is the Fermi energy of the sample. Only sample states with energy between E_F and $E_F + e|V_{bias}|$ contribute to the tunnel current. This result is based upon several oversimplifications but provides a qualitative understanding of the STM tunnel current.

In the fast scan (current) mode, the STM tip is scanned rapidly across the surface. Only the time averaged current is maintained at the bias current set point by controlling tip-sample separation. The instantaneous current fluctuates with tip position, r, in accordance with Eq. (2.1). The STM current image is a gray scale depiction of $I(r)$. When occupied, $|\Psi_\nu(r)|^2$ is the contribution of the state ν to the electron density. *Thus the current image is a direct map of electron density for the subset of electron states with energies that lie between E_F and $E_F + e|V_{bias}|$.*

In the slow scan (topographic) mode, the STM tip is scanned over the surface slowly so that the feedback electronics maintain the instantaneous tunnel current at the bias current set point. This is achieved by controlling the tip displacement normal to the sample surface as the tip is scanned across the sample. The topographic image is a gray scale depiction of tip displacement normal to the sample surface, z, as a function of r. For the current image we have given a simple physical interpretation, but the interpretation of the topographic image is more complicated. What physical quantity does

the topographic image gray scale represent if one images a flat material (i.e. all the nuclei of the surface atoms lie in a plane)?

Tersoff[6] has shown how to make a qualitative interpretation if one makes the assumption that sample surface states take the form

$$\Psi_k = \sum_G a(k,G)\exp[i(k+G)x]\exp(-\alpha_G z) \qquad (2.2)$$

where $\alpha_G = [\alpha_o^2 + (k+G)^2]^{1/2}$, $\alpha_o = (2m\phi/\hbar^2)^{1/2}$ and ϕ is the work function, G is a surface plane reciprocal lattice vector, **x** is a vector in the surface plane, and z is distance from the surface. In Eq. (2.2) surface states are assumed to decay exponentially with distance from the surface, and the high frequency components of Ψ_k decay more rapidly. *Thus imaging the surface at large z is equivalent to low pass filtering an image acquired at small z.* This true for both current and topographic images.

Topographic images acquired at large z and small V_{bias} may be simply interpreted. Small V_{bias} means only surface states Ψ_k with k on the Fermi surface are important, and large z means only the lowest frequency components of Eq. (2.2) must be retained. Thus

$$\Psi_{k_F} = a(k_F,0)\exp[i(k_F)x]\exp(-\alpha_{k_F} z) \qquad (2.3)$$

where $\alpha_{kF} = (\alpha_o^2 + k_F^2)^{1/2}$. If we assume $|k_F|$ is constant over the Fermi surface or small compared to α_o, then substituting Eq. (2.3) into Eq. (2.1) yields

$$I(r) \propto \exp(-2\alpha_{k_F} z)\sum_{k_F} |\Psi_{k_F}(x)|^2 \quad . \qquad (2.4)$$

Equation (2.4) is valid for both current and topographic images. Topographic images are obtained at a fixed tunnel current, I_o. Solving Eq. (2.4) for z(**x**) yields

$$z(x) = z_o + \frac{1}{2\alpha} \ln\left[\frac{I(x)}{I_o}\right] \tag{2.5}$$

where I(x) is the tunnel current one would obtain for a current image at set point current I_o which would result in tip height z_o. Thus, at large z and small V_{bias}, *the topographic image is equal to the logarithm of the current image. The topographic image gray scale reflects the logarithm of the charge density at the Fermi energy*, for a flat sample. No simple interpretation of topographic images of flat samples is possible for images acquired at small z or large V_{bias}.

The preceding discussion is based on Eq. (2.1), but Eq. (2.1) seems to imply that tunneling should not occur between a tip and a CDW material at small V_{bias}. According to Eq. (2.1) the range of sample states accessible to the STM is from E_F to $E_F + e|V_{bias}|$ for $V_{bias} < 0$. Typically, $|V_{bias}| \approx 10$ mV when one is imaging CDW samples[3,7-14], but the CDW energy gap is typically about 100 meV[4,11] so that electronic states occur about 50 meV below and above E_F. It should be noted, however, that Eq. (2.1) is a T = 0 K result. Finite temperature allows tunneling of electrons from the tip into CDW states, E_v, outside the range $E_F < E_v < E_F + e|V_{bias}|$ by producing some unoccupied states just below the gap and occupied states just above the gap, and the STM tunnel current reflects the spatial variation of those states.

2.3 Design of STM head

The STM we use is of conventional design using a piezo-electric tube scanner, and the computer control, data acquisition, and feedback control loop are described elsewhere[15,16]. In all but one way the STM head we use is also of conventional mechanical design. The STM head consists of two metal plates separated by adjustment screws that are threaded through one of the plates (see Fig. 2.1). The tip is attached to one of the plates and the sample is attached to the other. The coarse approach of the tip is

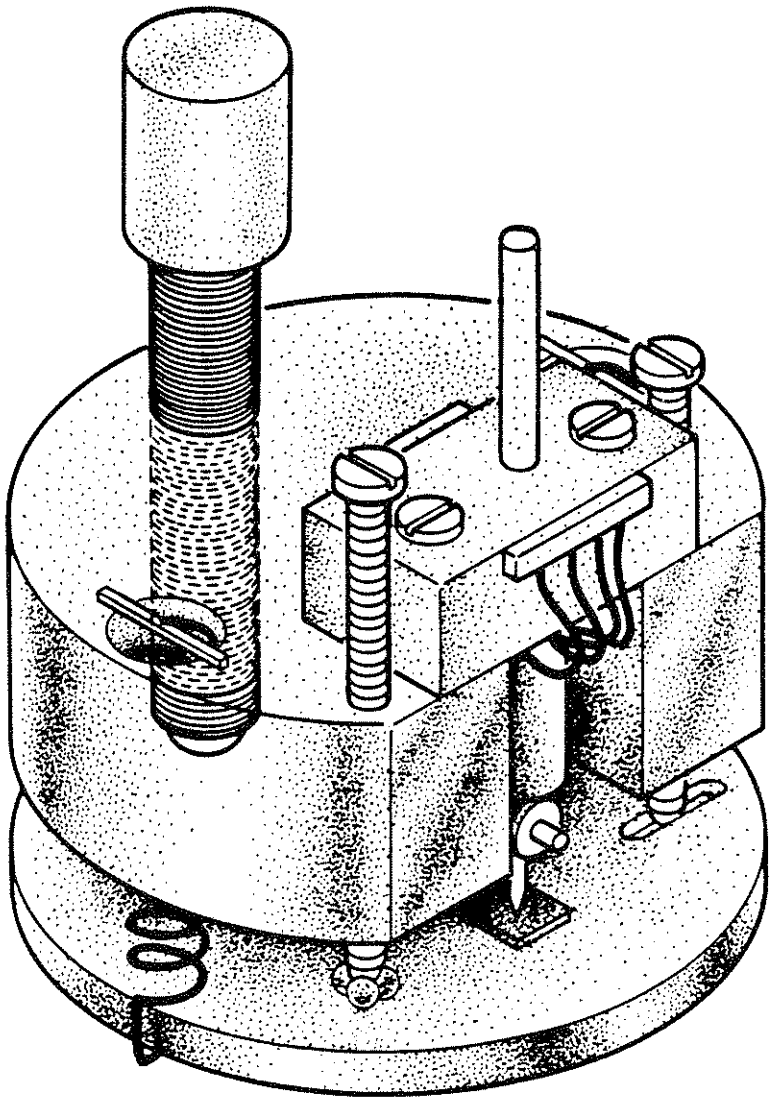

FIG. 2.1 Drawing of the STM head. Two screws in front are used for manual coarse approach of tip to sample. Screw in back is used for computer controlled final approach. (Figure provided by Ruth Thomson.)

XBL 884 7338

performed manually by adjusting the two screws in the front of the STM seen in Fig. 2.1. The final approach is performed by computer control of an electric motor which turns the screw seen in the back of Fig. 2.1 until a tunnel current is detected. The design and operation of the STM head is described in greater detail elsewhere[15,16].

The unique feature of our STM head is that the metal plates are made of Invar. Invar is a special alloy with an exceptionally low coefficient of thermal expansion. The low thermal expansion produces low thermal drift of the tip with respect to the sample. This property is extremely important for the performance of the variable temperature system described below. In order to obtain high quality STM images, the drift must be made as low as possible. At T = 143 K, the temperature control system allows a temperature drift rate of about 3 K/hr. For an earlier aluminum plate STM head we typically found a tip-sample distance drift of 3 Å/mK at T = 143 K which corresponds to a tip-sample distance drift rate of about 3 Å/s in the temperature control system. With the Invar plates we found a drift of less than 0.5 Å/s.

The Invar STM head displayed superior performance at room temperature as well, despite the nominally constant ambient temperature that one might expect to make the thermal coefficient of the plates irrelevant. Because the STM head is warm from handling as the sample is mounted, thermal drift can be a problem until the head has come to thermal equilibrium with the room. Usually twenty minutes were required for thermal gradients to relax sufficiently in the aluminum head so that high quality images could be obtained. With the Invar head, we obtain high quality images with no waiting time.

We also built an STM head with copper plates. In both the temperature control system and in air at room temperature, the copper head displayed drift characteristics superior to those of the aluminum head by a factor of two. While Invar should be superior to copper as an STM head material in most circumstances, Invar is a magnetic material. If one requires STM operation in a magnetic field and therefore cannot use

Invar, then copper should perform somewhat better than aluminum at higher temperatures where thermal expansion can be a problem.

As an aside, we describe a modification to our STM head which allowed us to use the STM as a small displacement sensor. Our goal was to measure the change in length of an o-TaS_3 crystal as the voltage across the sample was swept through the threshold voltage for CDW conduction[17]. We expected a length change of 2 Å in a needle-like sample that was 10 mm in length. In Fig. 2.2 we show a schematic of the modified STM head. We mount the sample in a "C" shaped holder where the top arm of the holder is a weak spring. The sample is mounted under tension, and the spring contains a small piece of freshly cleaved graphite above the sample-spring junction. The holder is fastened to the sample stage of the STM, and the three screws are adjusted to provide clearance for the holder. The STM tip is brought near the graphite manually, then under computer control the tip is brought into tunneling range of the graphite, and the STM is operated in topographic mode without lateral scanning. Thus as the sample changes length the graphite moves, and the tip follows resulting in a z displacement detected by the STM. With this technique we were able to resolve length changes of about 0.5 Å and measure length changes of 200 Å. In principle the axial extension range of the piezo-electric tube scanner would allow measurement of a length change as large as a few tenths of a micron.

2.4 Experimental procedure

Nearly all our STM images are acquired in the fast scan, i.e. current imaging mode rather than in the topographic mode, and the reader should assume any image presented later is a current image unless stated otherwise. We choose the current mode because interpretation of current images as a direct map of the electronic density at the Fermi energy is straightforward. Also on the pragmatic side our STM operates with lower noise in the current mode than in the topographic mode. Usually images were

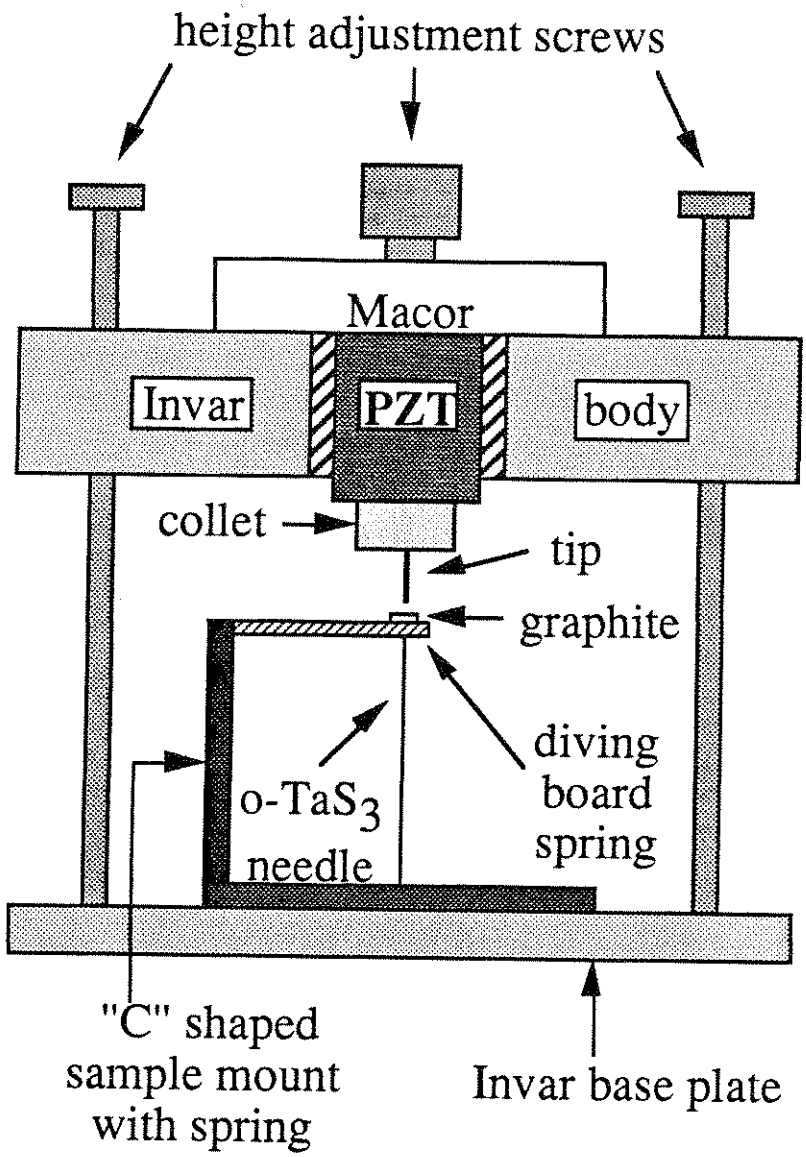

FIG. 2.2 STM head modified to detect small displacements

On computer
Brian, Thesis, chapter 2

obtained with set point currents between 1 nA and 5 nA and bias voltages between -1 mV and -100 mV. Generally the highest resolution images were obtained with higher currents and lower bias voltages i.e. smaller tunneling resistance and therefore smaller tip-sample separation. This observation is consistent with the discussion in section 2.2 where we noted that imaging at large z is equivalent to low pass filtering an image acquired at small z.

We cleave our samples under hexadecane oil or in air before mounting on the STM head. Especially for blue bronze, the oil offers some protection from surface contamination. 1T-TaS_2 has a very inert surface, and the benefit of cleaving it under oil is marginal. We have tried cleaving samples under other oils such as decane and silicone based diffusion pump oil and the results are essentially the same as for hexadecane. Hexadecane is somewhat superior to decane because it evaporates more slowly thus allowing samples to be mounted on the STM head in air for a longer period.

Our tunneling tips our made from 1 mm diameter Pt-20%Rh wire. The tip is made by squeezing the wire with a pair of wire cutters until the wire is almost but not completely cut. Then pulling between the wire cutters and a segment of wire finishes the separation by tearing the squeezed portion. Occasionally the tearing process exposes clean Pt-Rh and makes a good tip.

Vibration isolation is accomplished in three ways. First, the STM is located two stories below ground level on the bottom floor of a building to keep low frequency building vibrations to a minimum. Second, a bell jar covers the STM head and support structure to provide acoustic isolation. Third, the STM is placed on a 70 Kg granite block supported by air jacks to isolate it from floor vibrations.

We operate our STM at temperatures ranging from 75 K to 360 K. In Fig. 2.3 we show a schematic of the temperature control system. We stabilize the STM head at the desired temperature in a temperature bath. We place the STM head inside a copper can either filled with liquid or evacuated. The liquid serves as an efficient thermal coupler

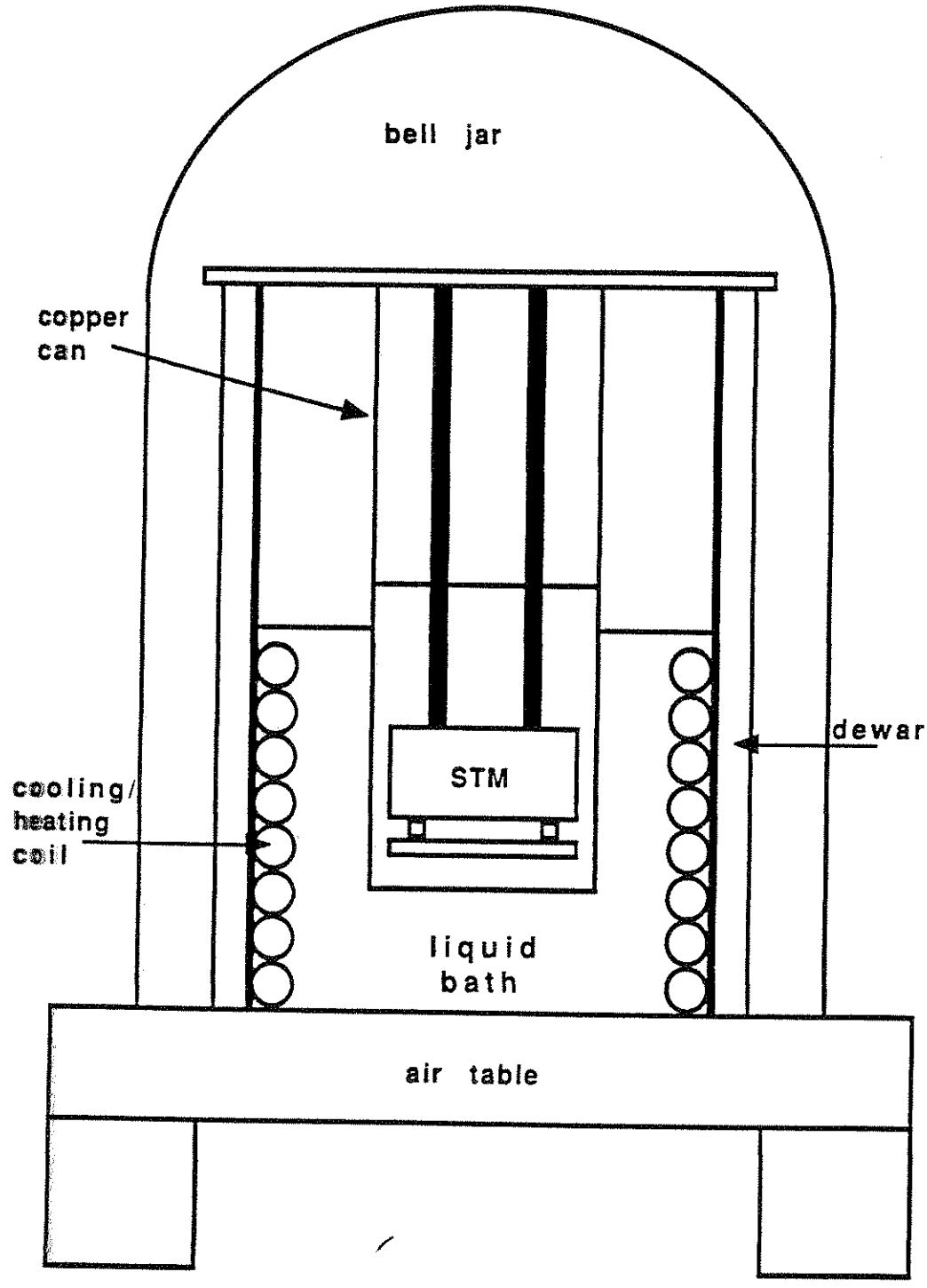

FIG. 223 Schematic of STM temperature control system (Figure provided by Ruth Thomson)

to the copper can and protects the sample surface from any air in the can. The copper can is then immersed in a liquid inside the dewar. The bath provides a stable temperature, and the STM head temperature approaches the bath temperature to within about 0.5 K in 45 minutes.

If the desired temperature is near the boiling point of liquid nitrogen, then we pour liquid nitrogen directly into the dewar and place the evacuated copper can in the dewar with the boiling liquid nitrogen. After the can has cooled, the bell jar is partially evacuated to lower the boiling point of the liquid nitrogen. Then the bell jar is vented to atmospheric pressure, and the nitrogen stops boiling because it is cooler than 77 K. This provides approximately twenty minutes before the nitrogen warms, begins to boil, and causes vibrations which make STM operation impossible.

If the desired temperature is between the freezing point of n-pentane (143 K) and room temperature, then we fill the copper can with n-pentane. The n-pentane dissolves hexadecane from the sample surface if the sample has been cleaved under hexadecane. The liquid bath is cooled to its freezing point by passing liquid nitrogen through the cooling/heating coil. Nitrogen flow is stopped, and a small amount of the cryogenic liquid is left unfrozen. For the cryogenic liquid we use n-pentane to stabilize at T = 143 K, n-octane to stabilize at T = 215 K, and water to stabilize at 273 K. These cryogenic baths typically produced nearly an hour of small temperature drift near the freezing point.

If the desired temperature is above room temperature, then we fill the copper can with hexadecane. The dewar is filled with mechanical pump oil, and an electrical heater tape is placed in the bottom of the dewar. The pump oil is raised to the desired temperature by applying a fixed voltage to the heater tape without feedback from the oil temperature sensor. The STM head temperature stabilizes in about two hours and thermal drifts are tolerable but not as small as drifts for the cryogenic liquid-solid mixtures.

2.5 Apodization of STM images

In our investigations of CDW structure in blue bronze and in 1T-TaS_2 we will need to search Fourier transformed STM images for peaks. In some instances the peaks we seek may be weak and located near stronger peaks. Unfortunately, these stronger peaks can obscure weak peaks. The effect arises from the abrupt real space image boundaries which produces streaking of peaks in Fourier transforms as demonstrated in Figs. 2.4(a) and 2.4(b). The computer simulated real space image in Fig. 2.4(a) contains 24 Fourier components with nearly the same wave vector magnitude (and incidentally also some much higher frequency Fourier components). However it is difficult to see all the Fourier peaks in Fig. 2.4(b). The solution to this problem is to apodize the real space image as shown in Fig. 2.4(c). Then all the Fourier components are easily seen in the Fourier transform shown in Fig. 2.4(d). The apodization window applied to the image in Fig. 2.4(a) to produce the image in Fig. 2.4(c) is a half sine wave. We have tried a variety of apodization windows including a full sine wave, a sinc function, a triangular window, and various exponential windows. We believe that the half sine wave produces the best compromise between compact but wide peaks and narrow but streaked peaks.

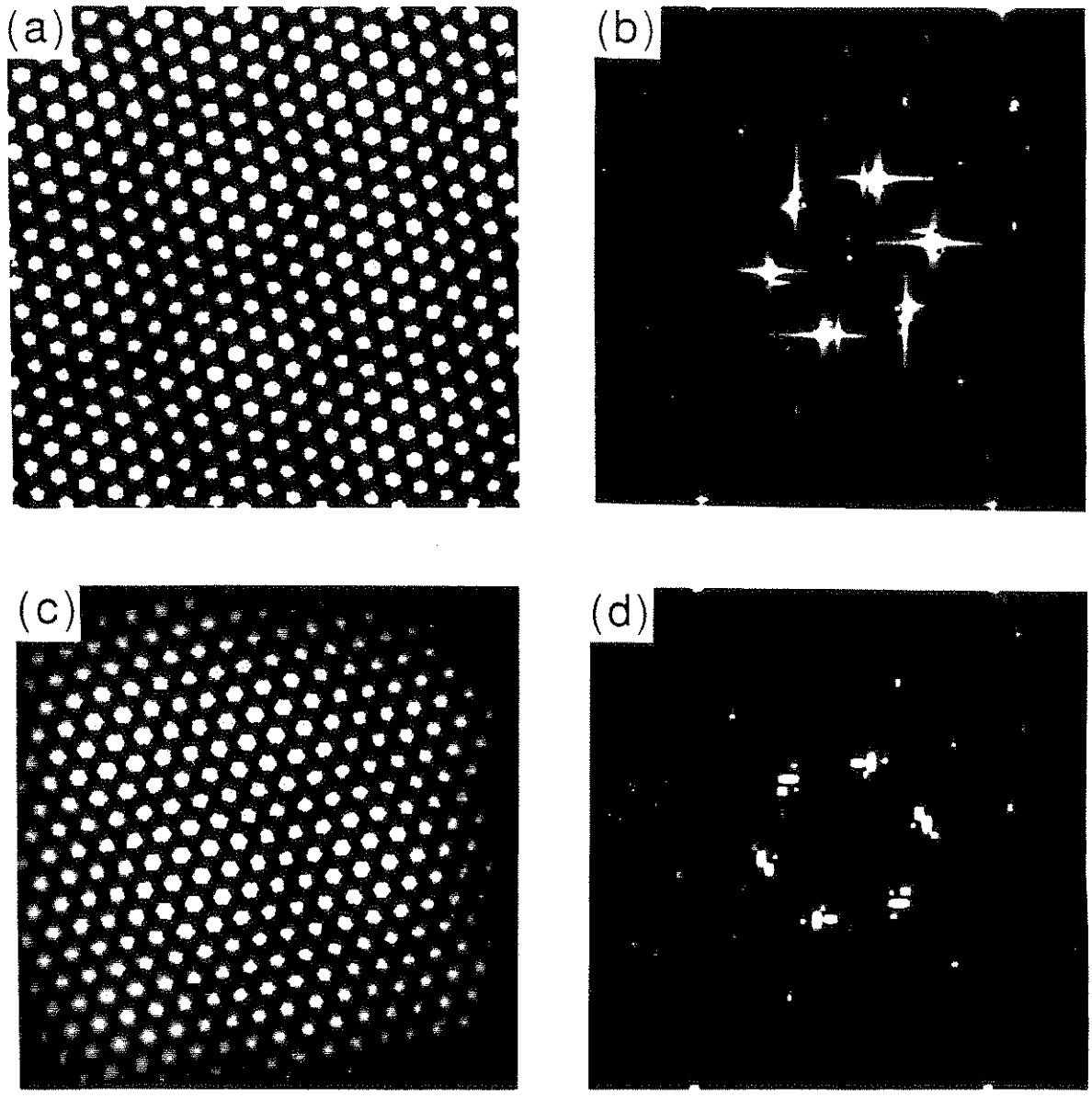

FIG. 2.4 (a) Computer generated image (unapodized) of 1T-TaS_2 in the NC phase (b) Fourier transform of (a) showing bright streaks due to image edges. (c) Same image shown in (a) after application of the apodization window. (d) Fourier transform of (c). Satellite spots are now more clearly visible. (Figure provided by Ruth Thomson)

References

1. J. Tersoff and D. R. Hamann, Phys. Rev. B **31**, 2 (1985).
2. P. K. Hansma and J. Tersoff, J. Appl. Phys. **61**, R1 (1987).
3. R. V. Coleman, B. Drake, P. K. Hansma, *et al.*, Phys. Rev. Lett. **55**, 394 (1985).
4. L. P. Gor'kov and G. Grüner, *Charge Density Waves in Solids*, V. M. Agranovich and A. A. Maradudin, Eds., Modern Problems in Condensed Matter Sciences (North-Holland, Amsterdam, 1989), vol. 25.
5. J. Bardeen, Phys. Rev. Lett. **6**, 57 (1961).
6. J. Tersoff, Phys. Rev. Lett. **57**, 440 (1986).
7. B. Burk, R. E. Thomson, A. Zettl, *et al.*, Phys. Rev. Lett. **23**, (1991).
8. R. V. Coleman, W. W. McNairy and C. G. Slough, Phys. Rev. B **45**, 1428 (1992).
9. G. Gammie, S. Skala, J. S. Hubacek, *et al.*, J. of Microsc. **152**, 497 (1988).
10. B. Giambattista, A. Johnson, W. W. McNairy, *et al.*, Phys. Rev. B **28**, 3545 (1988).
11. B. Giambattista, C. G. Slough, W. W. McNairy, *et al.*, Phys. Rev. B **41**, 10082 (1990).
12. R. E. Thomson, U. Walter, E. Ganz, *et al.*, Phys. Rev. B **38**, 10734 (1988).
13. X. L. Wu and C. M. Lieber, Science **243**, 1703 (1989).
14. X. L. Wu and C. M. Lieber, Phys. Rev. Lett. **64**, 1150 (1990).
15. R. E. Thomson, U. Walter, E. Ganz, *et al.*, J. Microsc. **152**, 771 (1988).
16. R. E. Thomson, Ph. D. Thesis, University of California, Berkeley (1991).
17. S. Hoen, B. Burk, A. Zettl, *et al.*, Phys. Rev. B **46**, 1874 (1992).

Chapter 3

Scanning tunneling microscopy of the blue bronzes $(Rb,K)_{0.3}MoO_3$

3.1 Introduction

The initial success in applying STM to the study of CDW materials was achieved with a layered dichalcogenide[1]. The dichalcogenides' quasi two-dimensional crystal and electronic structure allowed broad freshly cleaved and inert (clean) surfaces to be easily prepared, making them ideal STM specimens. While the dichalcogenides display many interesting static CDW properties, none of them exhibit a Fröhlich mode sliding CDW, and therefore lack the interesting dynamics of the electronically quasi one-dimensional CDW materials. In principle, it is possible to use an STM not only to study the static CDW[1-3], but also to investigate the CDW dynamics. For example, the Fröhlich-mode sliding CDW induced by a bias electric field should be accessible to a STM, provided that the surface CDW is not pinned excessively strongly. Surface pinning effects might cause the surface CDW to depin at a different bias field from that of the bulk. Therefore it would be interesting to image the surface CDW as the bias voltage across the sample is swept through the bulk threshold field for CDW conduction to see whether the surface CDW depins as well.

There are only a few systems known to show Fröhlich conductivity at reasonably low electric fields. These include $(TaSe_4)_2I$, $(NbSe_4)_{10/3}$, $NbSe_3$, TaS_3 and the two blue bronzes $K_{0.3}MoO_3$ and $Rb_{0.3}MoO_3$. The transition-metal trichalcogenides $NbSe_3$ and TaS_3 grow in needle-like crystals typically less than 100 μm in diameter, making them difficult to use as STM specimens. We attempted to image over 60 o-TaS_3 samples with very limited success both at room temperature and below the CDW transition temperature. Often attempts failed because the STM tip failed to be properly aimed at the sample. Nearly all images obtained when the tip did reach the sample were of such low quality that one could rarely discern the chain structure of o-TaS_3. In a few instances we

were able to see the chain structure and hints of atomic structure. However even our very best images were of such low quality that our failure to see the CDW in the low temperature runs is not surprising. A likely explanation for the imaging problems is surface contamination caused by the silver paint used to make electrical contact to the sample or the Stycast epoxy used to hold the sample in place. Both substances appear to wick into the strands of the o-TaS_3 samples and coat the surface. Dry clamped samples had a tendency to be deformed or deflected by the tip resulting in highly distorted images. The halogenated transition-metal tetrachalcogenides $(TaSe_4)_2I$ and $(NbSe_4)_{10/3}I$ have quasi-two-dimensional crystal structure and are therefore candidates for STM studies, but their rapid oxidation complicates surface studies. The blue bronzes, on the other hand, form large cleavable crystals that are relatively inert, making them practical specimens for STM experiments.

Before this work, two groups[4,5] have published STM images of blue bronze at room temperature which is above the CDW transition temperature, T_p = 180 K. We have attempted to image the CDW in blue bronze at temperatures below T_p. Although we obtained images displaying the lattice structure at 295, 143, and 77 K, we were unable to find evidence for the CDW. In this chapter we relate the surface lattice structure to the bulk, describe the surface CDW structure that we expect from x-ray diffraction and neutron-scattering results, and discuss possible reasons why we did not observe the CDW in our STM images.

3.2 Crystal structure and the CDW in blue bronze

The blue bronzes, $M_x MoO_3$ ($0.24 < x < 0.3$, M = Na, K, Rb), crystallize into the monoclinic $C\,2/m$ structure with a_o = 18.25 Å (18.94 Å), b_o = 7.560 Å (7.560 Å), c_o = 9.855 Å (10.040 Å), and γ = 117.53° (118.83°) with 20 formula units per unit cell for $K_{0.3}MoO_3$ ($Rb_{0.3}MoO_3$)[6,7]. These compounds form a layered structure with sheets of distorted MoO_6 octahedra (corner shared) separated by, but also held together by, the

alkali-metal atoms. These sheets are composed of units of ten octahedra, eight of which share edges to form a zig-zag chain in the [102] direction. The extra two octahedra, referred to as the "hump" octahedra[8], share an adjoining edge with two of the chain octahedra, displacing them slightly from the line of the chain octahedra. These units of ten octahedra in turn share corners of the chain octahedra of adjoining unit cells to form infinite Mo-O sheets parallel to the **b** and [102] plane.

Because the bonds between the sheets are weak, the crystals are easily cleaved parallel to the **b** and [102] plane. For concentrations of $x < 0.3$ the blue bronzes are nonstoichiometric because not all of the interstitial (interlayer) positions are occupied by the M atoms. For $x = 1/3$ the neighboring phase of semiconducting red bronze is formed.

Below $T_p = 180$ K an incommensurate CDW is formed in the blue bronzes. This creates a gap in the conduction band and therefore gives rise to semiconducting behavior below T_p[9]. The phase transition affects nearly all microscopic and macroscopic quantities measured below T_p. A CDW in blue bronze was postulated by Travaglini et al.[10] in 1981 and was subsequently confirmed by nonlinear electronic transport measurements[11] and by measurement of a Kohn anomaly in the molybdenum-oxygen octahedra along the $\mathbf{b}^*$ direction[12,13]. From x-ray diffraction and neutron-scattering data[12,14,15], the CDW wave vectors are known to be,

$$\mathbf{q}_{CDW}^{\pm} = \pm\delta\mathbf{b}^* + 0.5\mathbf{c}^* \ , \tag{3.1}$$

where $\delta = 0.737$ (0.74) for $K_{0.3}MoO_3$ ($Rb_{0.3}MoO_3$). From Eq. (3.1) we calculate the projection of the CDW translation vectors onto the cleavage plane in Appendix A. We find that the magnitudes of the two in-plane CDW translation vectors are 10.2 and 11.1 Å with an angle between them of 62.6°. Fleming et al. have suggested that below T = 100 K the CDW undergoes an incommensurate-commensurate phase transition[14], although

the occurrence of such a "lock-in" transition is still controversial. The threshold field for depinning the CDW, E_T, varies from 50 to over 250 mV/cm for T > 25 K[16].

The structural and transport properties of $K_{0.3}MoO_3$ and $Rb_{0.3}MoO_3$ are very similar above and below T_p, which is identical in the two materials. The STM images of the two types of blue bronze are also nearly identical. Thus all results described for $K_{0.3}MoO_3$ in the following discussion also apply to $Rb_{0.3}MoO_3$.

3.3 Experimental procedure and results

Most images were recorded in the current mode, each image being acquired in about 1.5 s. We obtained images above the transition at 295 K, in the incommensurate phase at 143 K (using a pentane ice bath), and in the proposed commensurate phase at 77 K. In addition we imaged $K_{0.3}MoO_3$ below T_p with an electric field across the sample.

We prepared single crystals of both K and Rb blue bronze for the microscope by evaporating three indium contacts onto the crystals before mounting them on copper sample holders with stycast epoxy (Fig. 3.1). One contact on the center of the rear side of the crystal was used for the tunneling bias voltage. The other two contacts on each end of the top side of the crystal enabled us to apply the electric field necessary to induce Fröhlich conductivity at low temperatures. We scored the crystal with a razor blade before cleaving it with tape; the epoxy protected the contacts during the cleaving process.

Initial test runs with samples cleaved in air did not produce images with atomic resolution. We attributed this to surface contamination and subsequently worked with samples either cleaved and handled in clean N_2 gas or cleaved under hexadecane. In the latter case, images at room temperature were obtained with the hexadecane remaining on the surface. We obtained low temperature images by dissolving the hexadecane in pentane and working in a bath of pentane at its melting point (143 K). These cleaner samples yielded images with lattice resolution at all three temperatures (see Figs. 3.2-

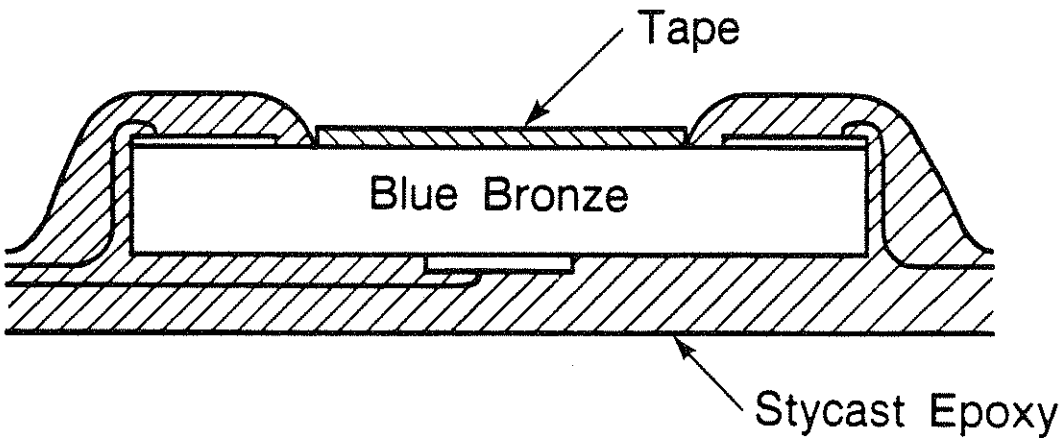

FIG. 3.1 Schematic of the sample mounted for the STM. The stycast epoxy protects the evaporated indium contacts while the sample is cleaved with tape. (Figure provided by Ruth Thomson)

XBL 895-5107

3.4).

Figure 3.2 is an example of the images we obtained at room temperature. The clear periodic structure in this image reflects the periodicity of the rhomboid unit cell of blue bronze. An analysis of 14 images taken at 295 K (from nine samples) yields values of nearest-neighbor distances of 7.4 ± 0.3 and 10.4 ± 0.4 Å and an angle between the two nearest-neighbor directions of 68° ± 3°. Our calculations from x-ray diffraction data on $K_{0.3}MoO_3$ yield a surface unit cell with crystal lattice translation vectors of 7.56 Å in the **b** direction and 10.56 Å in the [112] direction. The angle between these two lattice vectors is 69°. Thus, within our experimental uncertainty, the structure observed in the STM images agrees with the calculated crystal surface lattice translation vectors with regard to both the lattice constants and the angle.

Figures 3.3 and 3.4 are images of the sample in the proposed commensurate phase (77 K) and in the incommensurate phase (143 K), respectively. (Figure 3.4 is the only image shown in this chapter that was taken in the topographic mode and took about 30 s to acquire.) Comparing either figure with Fig. 3.2, we conclude that we are again imaging merely the surface lattice unit cell with no evidence of the CDW. An analysis of seven images (from five samples) taken at 77 and 143 K yielded lattice constants of 7.3 ± 0.6 and 10.7 ± 0.4 Å and an angle of 68° ± 4°. These lengths agree with the distances and angle given for the atomic lattice but do not agree with those calculated for the CDW in the cleavage plane. There is no indication of any superstructure we could attribute to the CDW.

In another attempt to find evidence of the CDW, we Fourier transformed our images as shown, for example, in Fig. 3.5(a), which is a Fourier transform of Fig. 3.4. For comparison, in Fig. 3.5(b) we display a Fourier transform model showing the position of the peaks for the atomic lattice and the CDW calculated from x-ray diffraction and neutron-scattering data[12,14,15]. A careful examination of Figs. 3.5(a) and 3.5(b) shows that the peaks from our STM image agree well with those calculated for the atomic

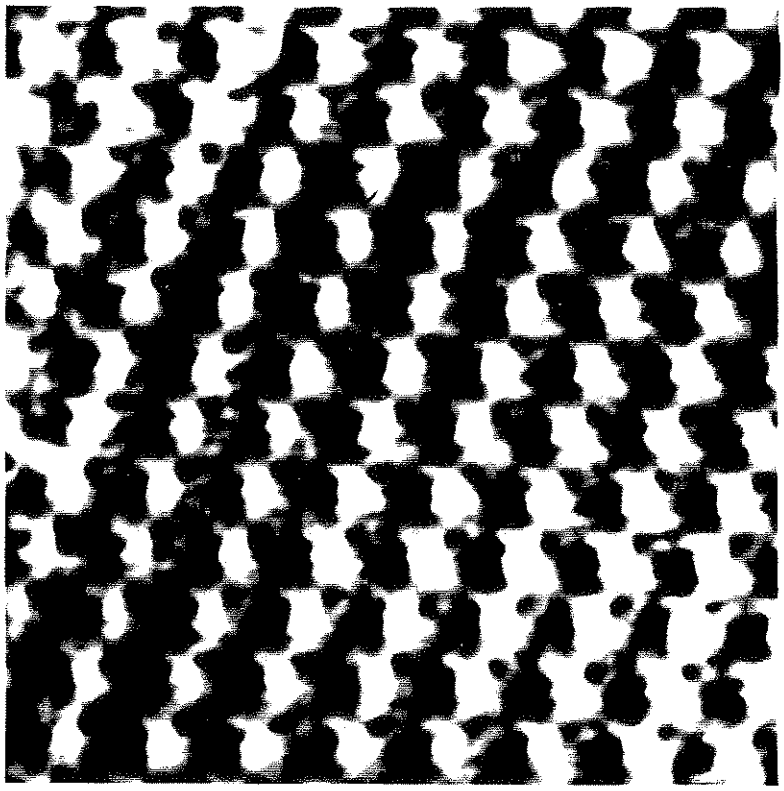

FIG. 3.2 STM image of $K_{0.3}MoO_3$ at 295 K. A single maximum per surface unit cell is resolved. (Figure provided by Ruth Thomson)

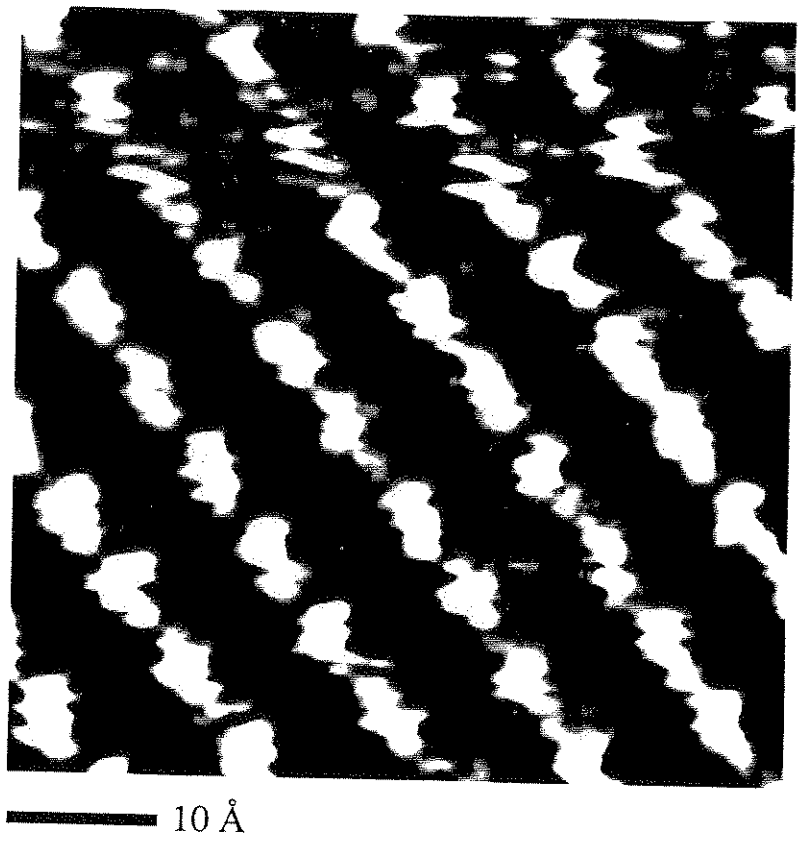

FIG. 3.3 STM image of $K_{0.3}MoO_3$ in the proposed commensurate phase at 77K. The image shows only the periodicity of the surface lattice unit cell and does not display any structure due to the CDW. (Figure provided by Ruth Thomson)

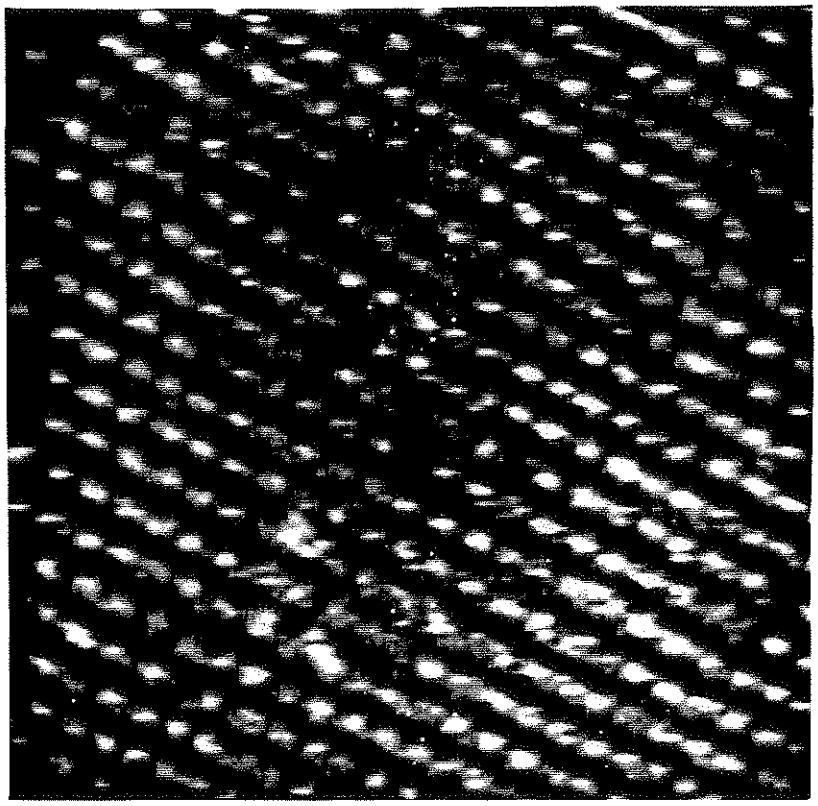

FIG. 3.4 STM image of $K_{0.3}MoO_3$ in the incommensurate phase at 143 K.

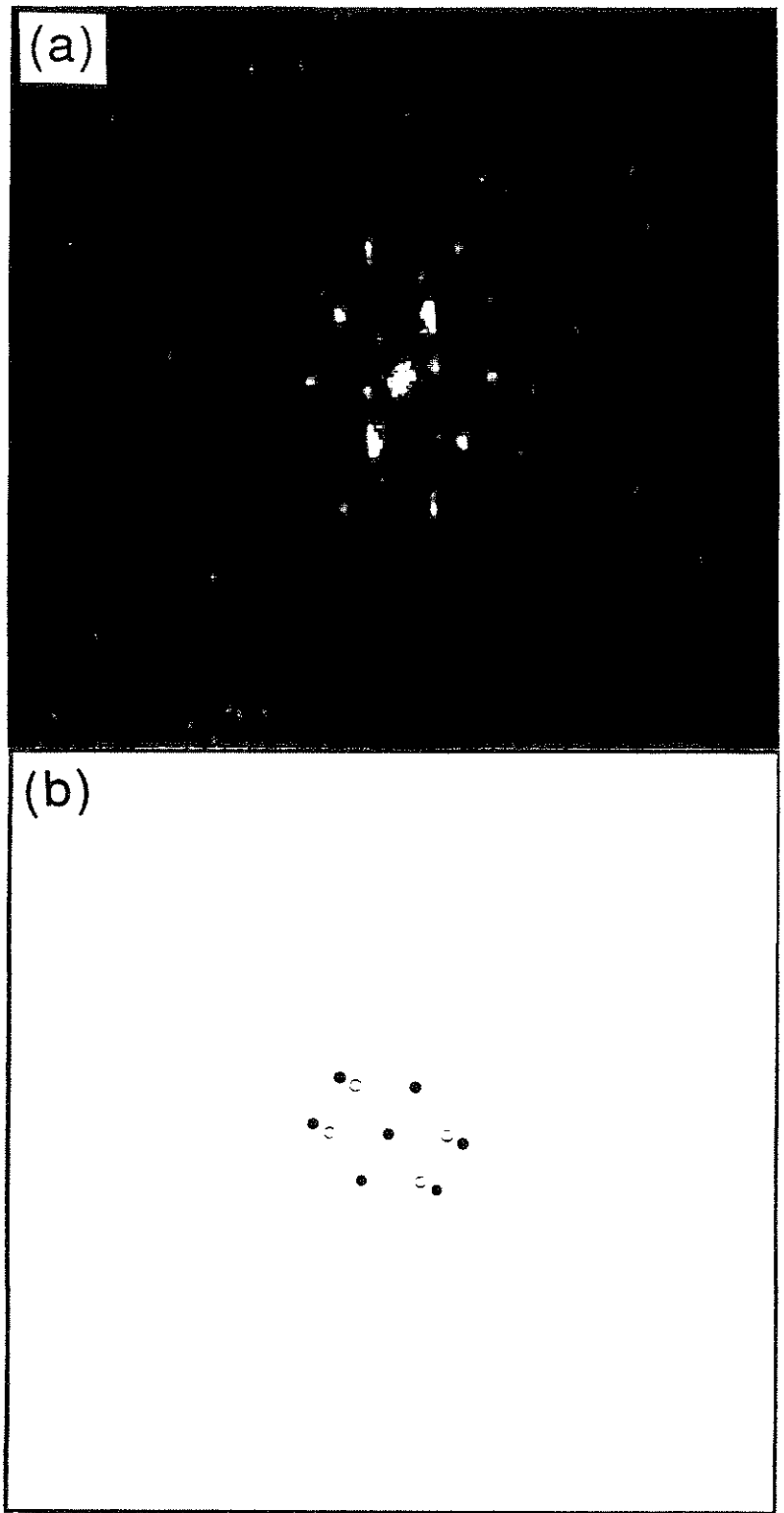

FIG. 3.5 (a) Fourier transform of Fig. 3.4 showing the atomic lattice peaks. The two weak peaks nearest the center of the transform are due to 60-Hz noise on the feedback signal. (b) Schematic showing the calculated positions of the atomic lattice peaks (closed circles) and the CDW peaks (open circles).

Fig 3.5 (a) only

XBB 915-3889

lattice, but that there are no discernible peaks corresponding to the CDW structure.

In a further attempt to see some signature of the CDW, we applied an independently grounded voltage of 200 mV to the two side contacts on the top surface of the crystal to produce an electric field three times the threshold field E_T (determined by a measurement of dI/dV on the same sample). This procedure did not extinguish or modify the structures observed by the STM at either of the lower temperatures. Therefore, we conclude that none of our STM images shows any evidence of the CDW superstructure.

3.4 Discussion

The inability of our STM to detect a CDW in blue bronze implies that the charge modulation at the surface is nonexistent or at least too weak to be detected. There appear to be at least two possible explanations for this observation. The first of these is that the CDW is attenuated near the surface. It is well known that the characteristics and behavior of the CDW at the surface can be significantly different from those in the bulk material[17-20]. In fact, it would be surprising for the CDW to extend unchanged to the surface, since one expects properties that are known to affect the CDW to be quite different on the surface from their values in the bulk. These properties include the impurity concentration and nonstoichiometry of the crystal, as well as the modified electronic structure at the surface. This last effect is especially important in blue bronze, where we expect that half of the alkali-metal atoms do not remain at the surface after cleaving[21]. If all the surface alkali atoms leave (perhaps by reacting with trace amounts of oxygen or water in the hexadecane oil), then the Mo-O layer at the surface could have only half the number of carriers in the conduction band as layers in the bulk have. In this case, if a CDW occurred at all in the Mo-O layer at the surface, it would certainly have different CDW wave vectors (since the shape and size of the Fermi surface that the wave vectors would nest would be drastically different) and possibly a much different transition temperature

than the bulk. Also, several studies have indicated that the pinning mechanisms of CDW motion may be influenced by surface effects[17-19], such as increased scattering of carriers by the surface or pinning by defects.

Alternatively, the CDW, as measured by STM, may be weak or absent on the surface because it is concentrated on those Mo-O octahedra that are significantly below the surface. Figure 3.6 is a schematic of the structure of blue bronze showing the relative displacements (due to the Kohn anomaly) of the atoms in the (010) plane from their room-temperature positions (after Sato et al.[12]). The top edge of the drawing, which we refer to as the "surface," is defined by the positions of the alkali-metal ions (closed circles) before the cleaving process. (The fact that these ions may have been removed during cleaving is not relevant to the argument, which concerns the relative distances of the various atoms from the surface.) The Mo atoms closest to the "surface" are 1.8 Å below the "surface" and those that undergo the largest displacements are 3.5 Å below the "surface." If the CDW is concentrated on the same atoms that are displaced due to the Kohn anomaly, as one would expect, it may be that the greater part of the CDW modulation is too far below the surface to be detected with STM.

Given our result that the CDW on the surface of blue bronze is either weak or nonexistent, it is of interest to consider previous work relevant to this problem. In 1990, Zhu et al.[20] reported that the CDW in blue bronze was easily detected by grazing-incidence x-ray diffraction. In this study, the CDW satellite peak was unchanged at the shallowest incident angle used, which was calculated to have an x-ray penetration depth of 20 Å, corresponding to about 2.5 Mo-O sheets. If our STM fails to image the CDW because it does not propagate to the surface, then to be consistent with the study of grazing-incidence x-ray diffraction we have to conclude that the CDW disappears within the last Mo-O sheet. However, our second proposed explanation for our results, that the CDW is concentrated on the Mo atoms which are too far below the surface for our STM to image the CDW, is also consistent with the x-ray results.

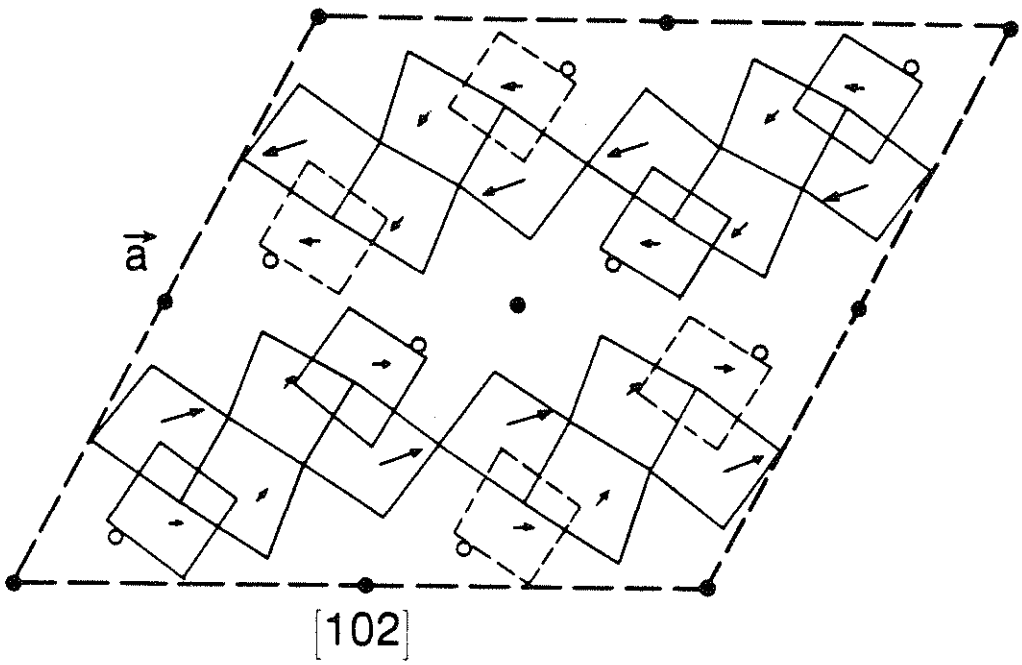

FIG. 3.6 Side view of a single unit cell of blue bronze projected onto the plane perpendicular to the **b** axis. The "surface" of the crystal (defined by the **b** and [102] plane) is along the top of the figure. Closed circles are the K atoms in the uppermost positions. Open circles are the K atoms 1.2 Å below the "surface." The Mo atoms are at the center of the oxygen octahedra and the three highest sets lie at levels 1.8, 2.4, and 3.5 Å below the "surface." The arrows indicate the relative amplitudes and directions of the displacement of the Mo atoms due to the CDW (after Sato et al.[12])

Our failure to detect the CDW appears to contradict the results of Nomura and Ichimura[22], who detected a peak in the frequency spectrum of the STM tunneling current which they attributed to the presence of a sliding CDW on the surface of a sample biased above its CDW conduction threshold field. However, these authors were unable to obtain STM images of either the CDW or the atomic lattice. It is possible that the peak that they observed in the frequency spectrum was due to a time-varying voltage (i.e., narrow band noise) induced across the sample by the sliding CDW. This oscillation voltage could have modulated the tip-sample bias voltage of the STM, and hence the tunneling current.

Finally, one might ask what aspect of the atomic lattice the STM images in blue bronze. The periodicity of the STM images reflects the periodicity of the unit cell of the material, but one would like to know which part of the unit cell, the K atoms or the Mo-O octahedra, is being imaged. An inspection of Figs. 3.7 and 3.8 reveals that the uppermost potassium atoms and the uppermost Mo-O octahedra (the "hump" octahedra of Ref. 8) both produce lattices with identical unit cell vectors (the known surface lattice translation vectors), making it impossible to differentiate between them from their measured periodicities. Since the blue bronzes are generally nonstoichiometric, not all of the interstitial (interlayer) positions are expected to be occupied by alkali-metal atoms. Even in a stoichiometric sample, the K ions represented by large closed circles in Fig. 3.7 can not be arranged at the lattice periodicity over the entire surface after cleaving because , at most, one-half of those ions can remain on the sample surface. Furthermore, without the planes of Mo-O octahedra on both sides of the K ions to hold them in place, the surface K ions might migrate from their sample bulk positions. Thus, if we were imaging the K ions, we would expect a very large number of defects, contrary to our observations. Therefore, we conclude that the periodic structure in our STM images is due to the Mo-O octahedra. In this case, we may be imaging just the uppermost "hump" octahedra (the dark gray octahedra in Fig. 3.8), or, alternatively, each maximum in the

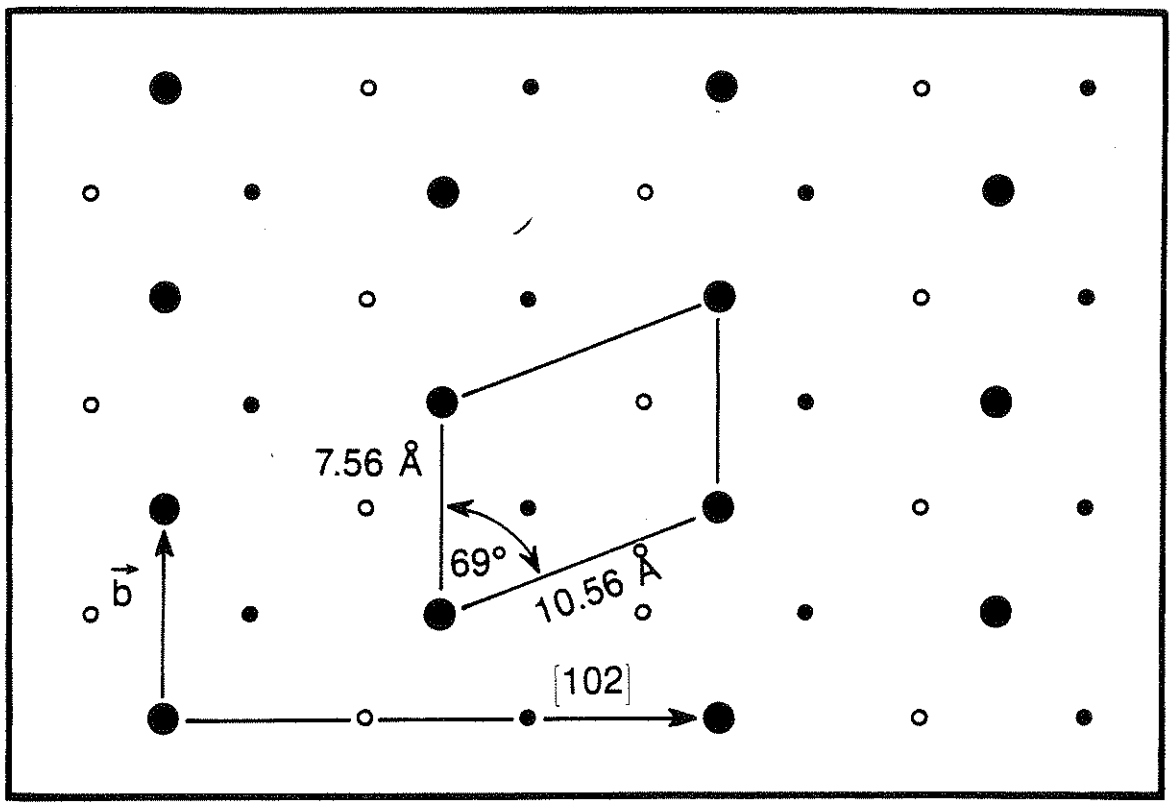

XBL 895-5110

FIG. 3.7 Positions of K atoms projected onto the **b** and [102] plane (the cleavage plane) calculated from x-ray diffraction data. Large closed circles indicate atoms in this plane. Small open circles indicate atoms 1.2 Å below the plane, and small closed circles indicate atoms 1.2 Å above the plane. (Figure provided by Ruth Thomson)

XBL 895-5110

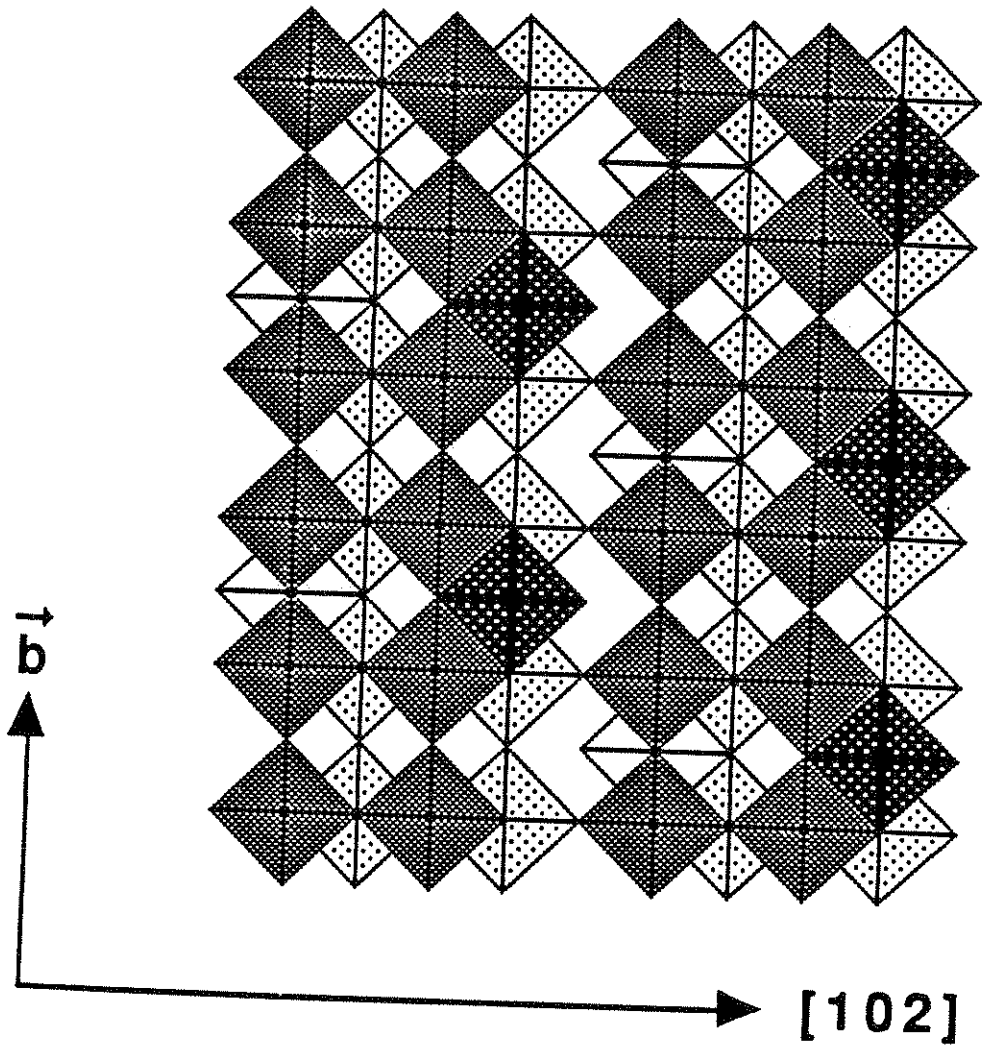

FIG. 3.8 Structure of the idealized Mo-O octahedra in the topmost unit cell of the cleavage plane. The centers of the "hump" octahedra (the rightmost octahedron in a shaded group of three) are 1.8 Å below the "surface" defined by the **b** and [102] plane. The gray octahedra have centers 2.4 Å below the "surface." (Figure provided by Ruth Thomson)

STM image may correspond to a blurred image of a group of three Mo-O octahedra (both the dark and light gray octahedra in Fig. 3.8). The latter option was the hypothesis of Heil et al.[4] for their room-temperature STM data, and Anselmetti et al.[5] concluded that it was at least consistent with their data.

In summary, we have used our STM to image the atomic lattice in the blue bronzes above the CDW transition temperature (295 K), in the incommensurate phase (143 K) and in the proposed commensurate phase (77 K). At all three temperatures the structure imaged by the STM is consistent with the surface crystal structure of the uppermost "hump" octahedra. However, we have not seen any evidence for the CDW's known to exist in these materials at the lower temperatures. The two most likely reasons for this fact are that either the CDW is attenuated at the surface of the crystal, or that the CDW is concentrated on the Mo atoms in the Mo-O octahedra that are too far below the surface to be imaged with our STM.

References

1. R. V. Coleman, B. Drake, P. K. Hansma, *et al.*, Phys. Rev. Lett. **55**, 394 (1985).
2. R. E. Thomson, U. Walter, E. Ganz, *et al.*, Phys. Rev. B **38**, 10734 (1988).
3. R. V. Coleman, B. Giambattista, P. K. Hansma, *et al.*, Adv. Phys. **37**, 559 (1988).
4. J. Heil, J. Wesner, B. Lommel, *et al.*, J. Appl. Phys. **65**, 5220 (1989).
5. D. Anselmetti, R. Wiesendanger, H.-J. Güntherodt, *et al.*, Europhys. Lett. **12**, 241 (1990).
6. J. Graham and A. D. Wadsley, Acta Crystallogr. **20**, 93 (1966).
7. J.-M. Reau, C. Fouassier and P. Hagenmuller, Bull. Soc. Chim. France **8**, 2883 (1971).
8. W. H. Whangbo and L. F. Schneemeyer, Inorg. Chem. **25**, 2424 (1986).
9. W. Fogle and J. H. Perlstein, Solid State Commun. **37**, 599 (1972).
10. G. Travaglini, P. Wachter, J. Marcus, *et al.*, Phys. Rev. Lett. **50**, 757 (1983).
11. J. Dumas, C. Schlenker, J. Marcus, *et al.*, Phys. Rev. Lett. **50**, 757 (1983).
12. M. Sato, H. Fujishita, S. Sato, *et al.*, J. Phys. C **18**, 2603 (1985).
13. C. Escribe-Filippini, J. P. Pouget, R. Currat, *et al.*, in *Charge Density Waves in Solids*, G. Hutiray and J. Solyom, Eds. (Springer-Verlag, Berlin, 1985), vol. 217, pp. 71.
14. R. M. Fleming, L. F. Schneemeyer and D. E. Moncton, Phys. Rev. B **31**, 899 (1985).
15. J. P. Pouget, C. Noguera, A. H. Moudden, *et al.*, J. Phys. (Paris) **46**, 1731 (1985).
16. R.M. Fleming, R. J. Cava, L. F. Schneemeyer, *et al.*, Phys. Rev. B **33**, 5450 (1986).
17. P.J. Yetman and J. C. Gill, Solid State Commun. **62**, 201 (1987).
18. J.McCarten, M. Maher, T. L. Adelman, *et al.*, Phys. Rev. Lett. **63**, 2841 (1989).
19. J.C. Gill, Europhys. Lett. **11**, 175 (1990).

20. X.-M. Zhu, R. Moret, H. Zabel, *et al.*, Phys. Rev. B **42**, 8791 (1990).

21. We expect that at least the K atoms in the **b** and [102] plane (those in the *d* positions; see Ref. 6) will not remain in their precleavage positions since one-half of the electrostatic forces holding them in place have been removed by cleaving.

22. K. Nomura and K. Ichimura, Solid State Commun. **71**, 149 (1989).

Chapter 4

Background for STM and x-ray diffraction of 1T-TaS_2

4.1 Introduction

The purpose of this chapter is to introduce facts and concepts that will be used repeatedly in each of the following three chapters. Chapters 5, 6, and 7 describe our STM and x-ray diffraction investigations of CDW structure in 1T-TaS_2. First we state some basic facts about the material we studied, 1T-TaS_2. Next we discuss STM of 1T-TaS_2. Each of the following three chapters will investigate CDW domain structure and so we provide here a brief summary of the theory of CDW domains. Finally, the investigations described in chapters 6 and 7 rely on x-ray diffraction of CDW materials and so we introduce the theory of x-ray diffraction of modulated structures.

4.2 Crystal structure and CDW structure in the various CDW phases of 1T-TaS_2

Tantalum disulfide is a layered material which forms a number of different polytypes defined by the stacking sequence of the layers. In the 1T polytype, the hexagonal unit cell contains a single three layer sandwich consisting of a middle layer of Ta atoms octahedrally coordinated to the two outer layers of S atoms. The atoms within a single sandwich are covalently bonded, while the bonds between sandwiches are van der Waals bonds, allowing the crystals to cleave easily along these planes.

At all temperatures at which 1T-TaS_2 is stable ($T < 543$ K), it exhibits a triple CDW, with three standing waves oriented at 120° to each other (except in the triclinic phase where the hexagonal symmetry is broken). From 543 - 353 K this material is in the incommensurate (I) phase. In this case the in-layer CDW and lattice translation vectors are aligned and the CDW has a wavelength of 3.53 a_0, where a_0 is the lattice constant of 3.346 Å at 295 K.[1] When the material is cooled below 353 K it enters the nearly commensurate (NC) phase. In this phase the CDW is rotated away from the lattice

[100] by an angle Φ. This angle varies with the temperature, changing from about 11° at 350 K to about 13° at 250 K.[1,2] In this phase the CDW wavelength may vary slightly with temperature, but remains incommensurate with the primitive lattice. When the material is cooled below 183 K, the ∠CDW undergoes another transition entering the commensurate (C) phase, In this case the CDW is at an angle of 13.9° to [100] and has a wavelength of 3.606 a_o, which makes it fully commensurate with the underlying tantalum lattice. Figure 4.1 is a schematic of the registration of the CDW on the atomic lattice in the commensurate phase. When the material is warmed from the commensurate state, it undergoes a transition at 223 K and enters the triclinic (T) phase. In this configuration, the CDW loses its hexagonal symmetry. Finally, when the temperature is raised above 283 K, the CDW again returns to the NC phase. The characteristics of each of the phases of 1T-TaS_2 are summarized in Table 4.1 and Fig. 4.2. For comparison, examples of high-resolution STM images taken in each of the four phases are shown in Fig. 4.3.

4.3 STM of the C phase CDW in 1T-TaS_2

To understand the more complicated and interesting NC, T, and I phases investigated in chapters 5, 6, and 7, it is necessary first to understand the commensurate structure seen in the commensurate (C) phase at temperatures below 180 K. It is well known from x-ray studies[1,3] that in the C phase the CDW forms a hexagonal superlattice with a $\sqrt{13} \times \sqrt{13}$ unit cell rotated 13.9° from the atomic lattice. The CDW maxima are centered on 13 Ta atom clusters arranged on a star-of-David pattern as was shown in Fig. 4.1. Figure 4.4 shows several filtered STM images of 1T-TaS_2 taken in the C phase at 143 K. In these images, both the CDW and the underlying atomic lattice are visible. Moreover, it is evident that the CDW is commensurate with the atomic lattice in these images because the fine structure of each CDW maximum in an image is virtually identical to all the other maxima in that image.

In the C phase as well as the other CDW phases we find that the CDW supercell

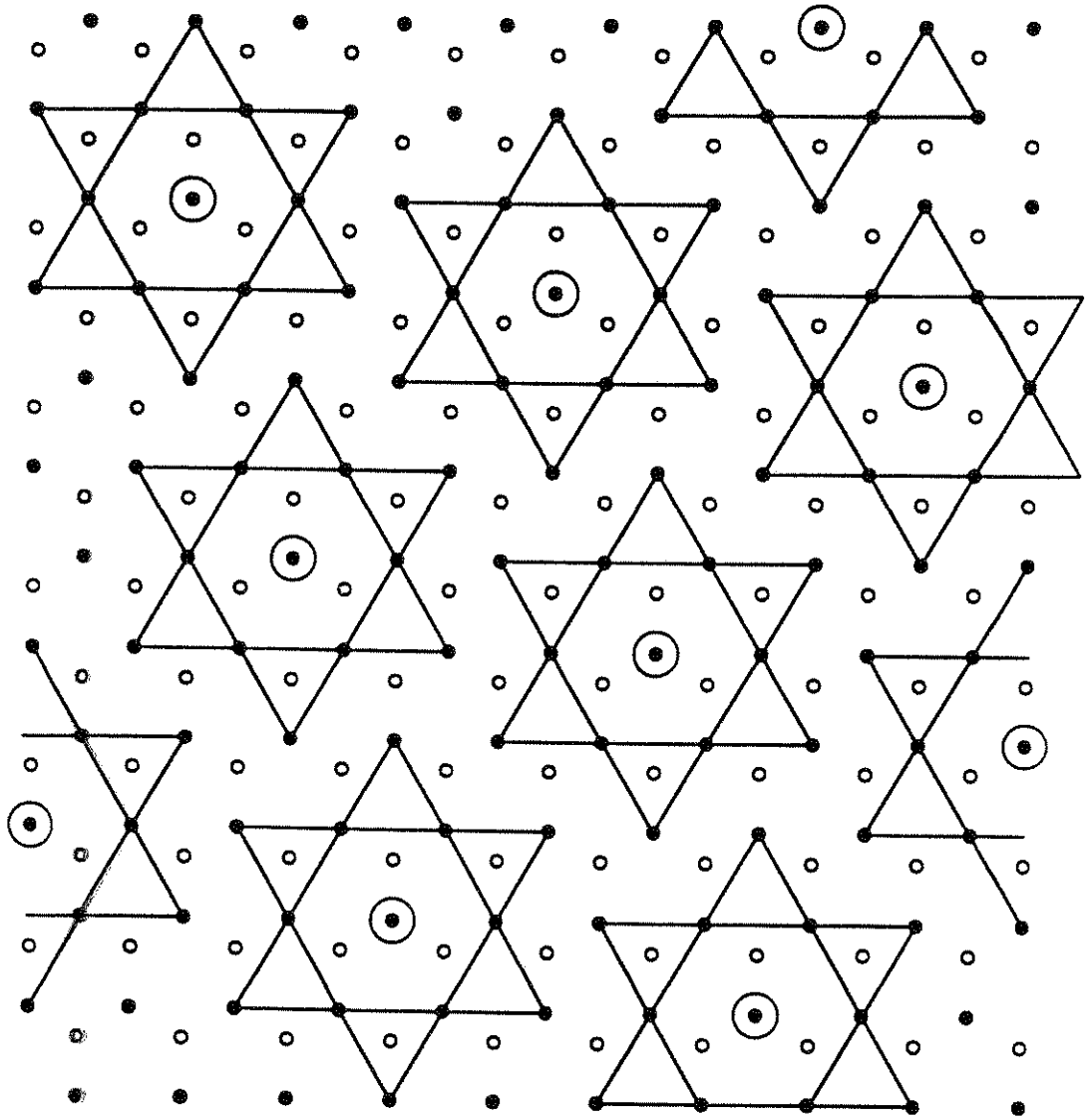

FIG. 4.1 Schematic of the registration of the CDW with the tantalum lattice in the commensurate (C) phase. Small solid circles represent the Ta atomic lattice, small open circles represent the S atoms on the surface, and larger open circles represent the CDW maxima formed by constructive interference of the three CDWs oriented at 120° relative to each other. (Figure provided by Ruth Thomson)

Phase	Temperature (K)	Φ (Degrees)	Comments
Normal	T > 543	NA	No CDW is known to exist. Difficult to study because crystal transforms to 2H polytype
I	543 > T > 353	0	CDW is incommensurate and is aligned with the lattice [100]
NC	T↑ 283 < T < 353 T↓ 353 > T > 183	11° - 13°	CDW is incommensurate and rotated away from the lattice [100]
C	T↑ T < 223 T↓ T < 183	13.9°	CDW is commensurate
T	T↑ 223 < T < 283	12° - 13°	CDW loses hexagonal symmetry.

Table 4.1 The phases of the CDW in 1T-TaS_2

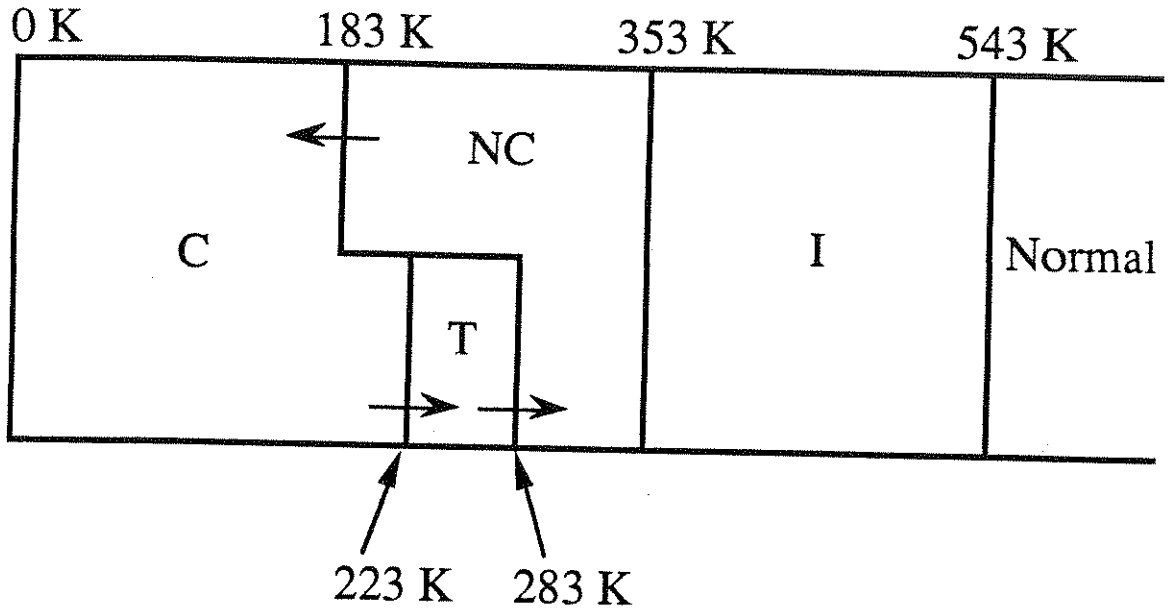

FIG. 42 Temperature regions of the CDW phases in 1T-TaS_2

On Computer Brian, Thesis, Chapter 4

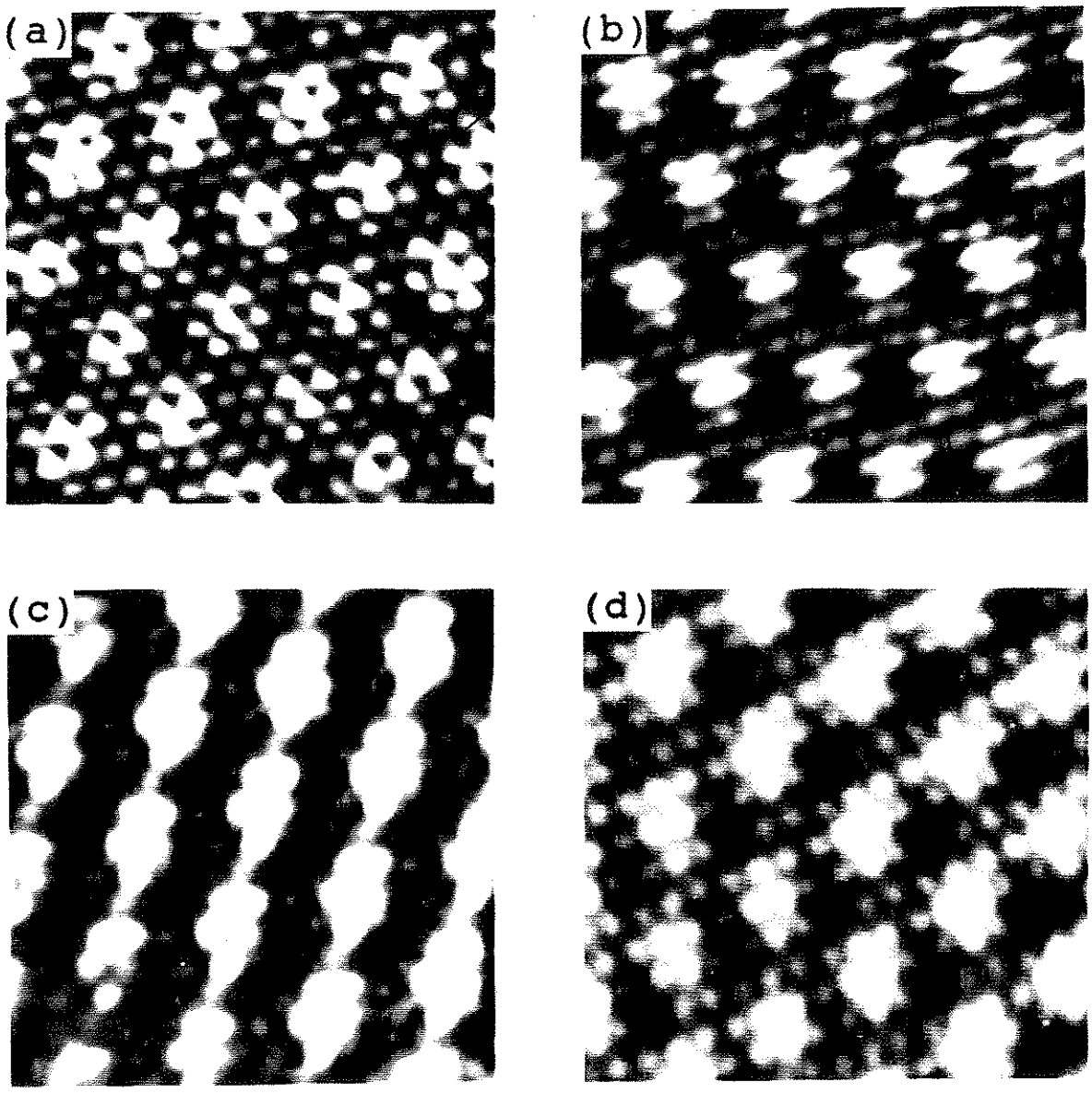

FIG. 4.3 Examples of high-resolution STM images, approximately 50 Å square, taken in the constant height mode for each phase of 1T-TaS_2. (a) I phase at 360 K; note that the CDW is aligned with the atomic lattice. (b) NC phase at 295 K; CDW is rotated away from the atomic lattice but is not yet commensurate. (c) C phase at 143 K; CDW is fully commensurate. (d) T phase at 263 K; similar to the NC phase. (Figure provided by Ruth Thomson)

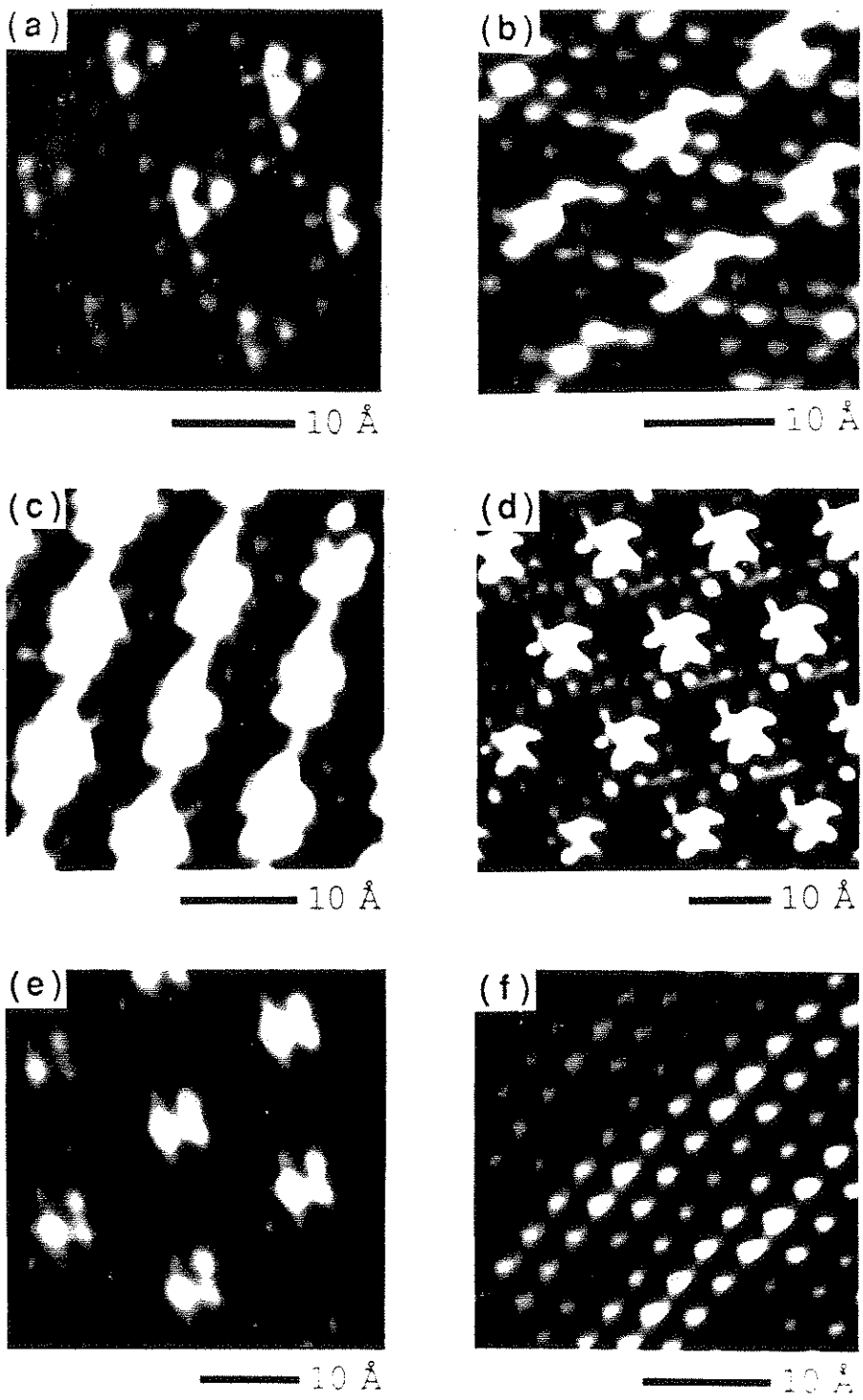

FIG. 4.4 Six examples of the variety of registrations we observe in STM images of the C phase. All images have been peak filtered. (a) and (c) are in the α orientation while (b), (c), (d), (e), and (f) are in the β orientation. (Figure provided by Ruth Thomson)

can be rotated counterclockwise (α rotated in the notation of Wilson et al.[4]), as in Fig. 4.4(a), or clockwise (β rotated), relative to the primitive atomic lattice, as in Fig. 4.4(b). X-ray diffraction experiments show that these two related superstructures can coexist in the same sample[1]. On one occasion we found adjacent areas of α and β rotation, but were unable to image the boundary region. In all other cases, we have observed only one type of rotation across the entire surface area accessible to our microscope (about $1\mu m^2$ at room temperature).

One surprising property observable in Fig. 4.4 is the asymmetry of the CDW maxima. If the CDW in the tantalum layer forms the star-of-David pattern shown in Fig. 4.1, as has been the assumption in the field for many years, then the registration of the CDW in the sulfur layer should have an $a_o/\sqrt{3}$ displacement from the tantalum layer as illustrated in Fig. 4.5(a). This image is a computer-generated model of an STM image of 1T-TaS_2 in the C phase formed by adding three sine waves to represent the atomic lattice and three sine waves to represent the CDW. The wave vectors have been chosen to produce a commensurate CDW with a $\sqrt{13} \times \sqrt{13}$ superstructure. The offset of the atoms relative to the CDW maxima in this image has been chosen to agree with the $a_o/\sqrt{3}$ offset expected between the surface sulfur atoms and the CDW maxima centered on tantalum atoms $c_o/2$ below. Comparison of Fig. 4.4 and Fig. 4.5(a) reveals that the asymmetry in the real STM images of 1T-TaS_2 in the C phase cannot be explained by the phase shift introduced by the $a_o/\sqrt{3}$ displacement between the surface sulfur atoms and the underlying tantalum atoms which support the CDW. It is also clear that such asymmetric maxima can not be explained by assuming that the STM images the tantalum one layer below the sulfur atoms, in which case the CDW maxima would appear to have an atom in the center with the greatest intensity ringed by six atoms of lesser intensity. In addition to the problem of the asymmetric maxima, we also find a wide variety of apparent atomic registrations in our C phase STM images (see Fig. 4.4).

The explanation for these observations comes from a well known property of

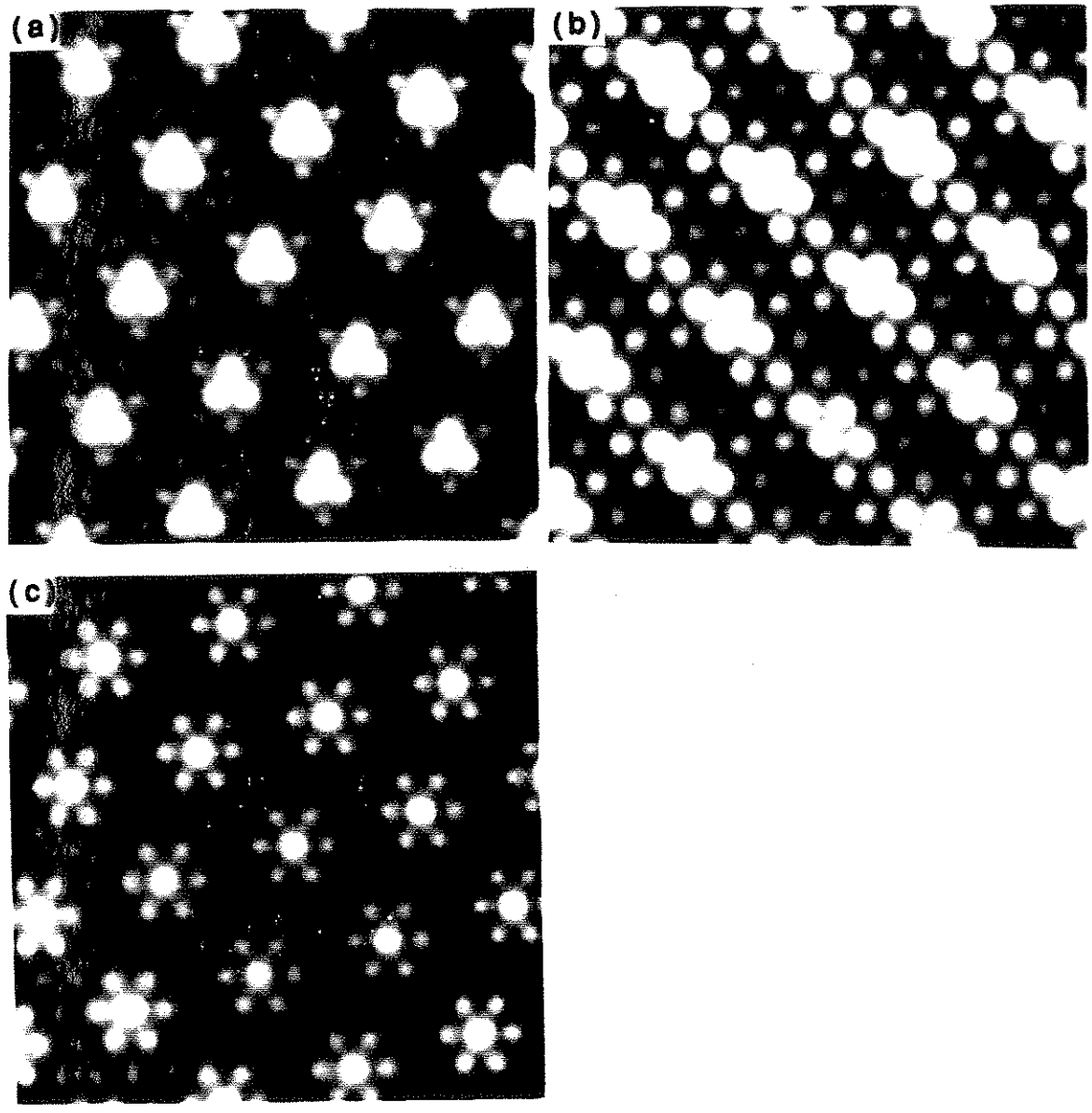

FIG. 4.5 Computer simulations of STM data for the C phase. (a) Simulation showing S atoms and the commensurate CDW. (b) Simulation of double tip data; two images of (a) were offset from each other and added together to generate this image. (c) Simulation of triple tip data, made by superposing three copies of (a) offset by lattice constants. (Figure provided by Ruth Thomson)

XBB 916-434/A

STM images: the STM can produce multiple images that have been superimposed[5]. This occurs when the STM tip terminates in multiple atoms through which the tunneling current passes. Since these two or more atoms can be at an arbitrary distance from and orientation to each other, as well as at different heights above the surface, the effect is to add together multiple STM images with an arbitrary offset and relative amplitude. This effect is present in many STM images of materials such as graphite[5,6].

In order to elucidate the types of effects such multiple tips can have on an STM image, we display computer simulations of multiple tip data in Figs. 4.5(b) and 4.5(c). We generated these images by multiplying Fig. 4.5(a) by an attenuation factor and adding a lateral offset and then adding the result to the original Fig. 4.5(a). This procedure produces images with asymmetrical CDW maxima similar to those seen in the real STM data shown in Fig. 4.4. Similar simulations can produce images that mimic any other atomic registration by simply varying the offset and relative amplitude of at least two separate images which are then added together[7].

We have further verified the fact that multiple tunneling tips produced many of our STM images by a careful examination of the relative phase of the three CDW fundamental peaks in the FTs of our images. The superposition of images offset by an arbitrary amount does not introduce new Fourier components into the resultant image, but rather alters the relative phase of the peaks. By measuring the phase of each of the peaks and adding these numbers together, we calculated a relative phase for the CDWs in that image. We found that this relative phase varied from 0° to 360°, and an analysis of 50 of our best images did not produce a peak in the distribution of these phases. On the contrary, the measured relative phase appeared to be random. From this we conclude that the majority of our images are made with multiple tips. However, we stress that multiple tip effects do not alter the distribution of Fourier peaks. Multiple imaging tips can change the relative phase and amplitude of Fourier peaks but cannot effect their positions or create false peaks.

4.4 Theory of CDW domains

When a system contains two periodic lattices with incommensurate periods, in the simplest case the system will be in a uniformly incommensurate state. However, if there is some interaction between the two periodic structures, the interaction term in the total free energy may be lowered if the two lattices become commensurate. In this case, there is a competition between the terms in the free energy that determine the individual periodicities of the two lattices and the term that promotes their commensurability. For the appropriate magnitudes of these terms, it is possible for such a system to exist in a discommensurate state[8]. In this case, the two periodicities become locally commensurate within domains and undergo phase slips at the domain walls, called discommensurations, that preserve the average incommensurate periodicities. Here we review the McMillan model of CDW domains[8] to provide the theoretical background for the work described in chapters 5, 6, and 7.

In the one dimensional case, McMillan's idea was that a uniform CDW that is close to commensurability would form a periodic beat pattern with the underlying atomic lattice. A presumed commensurability energy drives a phase distortion so that the CDW phase readjusts to maximize the in phase portion of the beat and minimize the out of phase portion thereby producing a phase modulated CDW. In McMillan's view, in phase means that the peak of the CDW lies between the transition metal atoms of the lattice so that the bond charge is maximized. Maximizing the in phase portion is achieved by a local change of the CDW wavelength to the commensurate value through most of the beat period followed by a drastic change of the CDW wavelength away from the commensurate value between commensurate regions. The region of drastic change is called the discommensuration. The change in CDW wavelength in the commensurate region is exactly compensated by the change in the wavelength between commensurate regions so that the average CDW wavelength is unaltered with respect to the uniformly

incommensurate case. Opposing the commensurability energy is an elastic strain energy for the CDW phase distortion. Without the strain energy the CDW could distort to the commensurate wavelength uniformly throughout the entire lattice. The periodic phase modulated domain structure at the beat period is the best compromise between these two competing energies.

The beat frequency, k_b, is determined by the reciprocal lattice frequency, a*, and the uniformly incommensurate CDW frequency, k_{cdw}.

$$k_b = a^* - nk_{cdw} \tag{4.1}$$

where n is an integer such that $nk_{com,cdw} = a^*$ and $k_{com,cdw}$ is a commensurate CDW frequency near k_{cdw}. The beat period, L_b, is $2\pi/k_b$. This leads directly to

$$(k_{cdw} - k_{com,cdw})L_b = k_{com,cdw}a_o \tag{4.2}$$

where a_o is the lattice constant. This means that the phase of the uniformly incommensurate CDW advances by one lattice constant with respect to the phase of a commensurate CDW over a beat period. Also, the phase of the modulated CDW advances by one lattice constant with respect to a commensurate CDW because the modulated and uniformly incommensurate CDW have the same average wavelength. The only difference between the uniform and phase modulated case is that the phase advance occurs suddenly between commensurate regions for the modulated case. Thus a McMillan phase domain exhibits a one atomic lattice constant phase slip of the CDW as the CDW goes from the center of one domain, through the discommensuration, and to the center of the adjacent domain.

So far we have given a qualitative explanation of what phase domains are and why they might occur. Now we describe the McMillan domain theory in more detail.

The theory is essentially one-dimensional. McMillan sought to determine the temperature and spatial dependence of the CDW order parameter through a Ginzburg-Landau type free energy calculation. The starting point is the McMillan free energy,

$$F = \int dx\left(a\,\alpha^2 - b\,\alpha^3 + c\,\alpha^4 + e\left|\left(q_{cdw}\bullet\nabla - i\,q_{cdw}\right)\psi\right|^2 + f\left|q_{cdw}\times\nabla\psi\right|^2\right) \qquad (4.3)$$

where $\alpha(x) = \mathrm{Re}[\Psi(x)]$ and the complex order parameter $\Psi(x)$ represents the CDW. The parameter, a, has a linear temperature dependence and is negative in the CDW state while the parameters b, c, e, and f are temperature independent. The parameter b is periodic with the periodicity of the crystal lattice. b (x) is expanded as $b_o + b_1 \cos(a*x)$. b_1 provides the commensurability energy. c stabilizes the free energy at finite order parameter. The term proportional to e results from the electronic band dispersion parallel to q_{cdw} and the term proportional to f results from band dispersion transverse to q_{cdw}. These last two terms provide stiffness to the CDW so that it resists phase distortion.

McMillan makes the ansatz that

$$\Psi(x) = \exp(i\,k_{cdw}x)\exp[i\,\theta(x)] \qquad (4.4a)$$

$$\theta(x) = \sum_n A_n \sin(nk_D x) \quad . \qquad (4.4b)$$

The phase modulation is periodic with period L_D because the beat pattern has that period. It is assumed that only phase modulation occurs because the energy to create a long wavelength phason is much less than the energy to create an ampliton. He expands the phase modulation function, $\Theta(x)$, in a Fourier series at multiples of the domain frequency, k_D, which is equal to the beat frequency. The A_n are variational parameters determined by substituting $\Psi(x)$ into Eq. (4.3) and minimizing with respect to A_n. McMillan finds that the phase transition from the commensurate state to the phase

modulated-discommensurate state is second-order. It should be emphasized that his ansatz guaranteed only phase modulation in the discommensurate state. The CDW order parameter $\Psi(x)$ contains Fourier components at $k_{cdw} \pm mk_D$ for m = 1, 2, 3, etc. McMillan's treatment showed that periodic domain structure should exist but contained the inappropriate restriction that amplitude modulation is absent.

In order to explain the x-ray diffraction data of Yamada and Takatera, Nakanishi and Shiba theoretically treated domain structure in the NC phase of 1T-TaS_2[9-11]. They began with the McMillan free energy incorporating the two-dimensional hexagonal symmetry of the triple CDW in the NC phase. They generalized the Fourier series expansion of the trial function $\Psi(x)$ to allow both phase and amplitude modulation. They found that amplitude and phase modulation of the CDW are equally important in creating the NC phase domain structure and that the commensurate to modulated-discommensurate phase transition is first-order. They calculated the amplitudes of the Fourier components of $\Psi(x)$ which occur at $k_{cdw} + lk_{D1} + mk_{D2} + nk_{D3}$ for l, m, n = 1, 2, 3, etc. The domain wave vectors k_{D1}, k_{D2}, and k_{D3} are determined from the periodicity of the two dimensional moiré pattern formed between the atomic lattice and the incommensurate CDW in direct analogy with the determination of the beat frequency of the one-dimensional McMillan treatment.

We will provide a pictorial representation of the domain structure calculated by Nakanishi and Shiba in chapter 5 where we describe our STM investigation of the NC phase of 1T-TaS_2. Detailed theoretical treatments of domain-like structure for the T and I phases do not exist, but two basic principles should apply: (1) the domain periodicity is the same as the moiré pattern periodicity, and (2) in addition to the fundamental CDW Fourier component, k_{cdw}, domain modulation induces Fourier components in the CDW order parameter at $k_{cdw} + nk_D$ for some integral values of n.

4.5 X-ray diffraction of modulated structures

Because the work described in chapters 6 and 7 relies heavily on x-ray diffraction of 1T-TaS_2, we explain the calculation of the diffraction pattern for a CDW material so that we can demonstrate two points that will be crucial to understanding our results. Calculating the structure factor for a one-dimensional CDW in a monatomic one-dimensional lattice will suffice:

$$S(k) = \sum_L f(k)\exp(i\,kr_L), \tag{4.5}$$

where S(k) is the structure factor and f(k) is the atomic form factor at wave vector k and r_L is the position of the atom at lattice site L. The CDW induces, through a linear electron-phonon coupling, a sinusoidal periodic lattice distortion (PLD)[12]. Thus

$$r_L = L + A\sin(k_{cdw}L) \tag{4.6}$$

where A is the amplitude of the PLD. Substituting Eq. (4.6) into Eq. (4.5) yields

$$S(k) = \sum_L f(k)\exp(i\,kL)\exp[i\,kA\sin(k_{cdw}L)]. \tag{4.7}$$

The trick that allows evaluation of Eq. (4.7) is the mathematical identity[12]

$$\exp[i\,z\sin(\phi)] \equiv \sum_{m=-\infty}^{\infty} J_m(z)\exp(i\,m\phi) \tag{4.8}$$

where J_m is a Bessel function of order m. Using this identity produces

$$S(k) = f(k)_m \sum_{m=-\infty}^{\infty} J_m(kA)\delta[G - (k - mk_{cdw})] \qquad (4.9)$$

where G is any reciprocal lattice vector.

Equation (4.9) shows that the diffraction pattern will have peaks at $k = G \pm mk_{cdw}$, $m = 0, 1, 2$, etc. Each Bragg peak is surrounded by CDW peaks. Surprisingly, *even a purely sinusoidal PLD produces second and higher-order CDW peaks.* We investigate higher than first-order CDW peaks in the T and I phase in later chapters. The mere presence of a higher than first-order peak does not prove that the CDW deviates from a perfect sine wave. Therefore the existence of higher-order CDW peaks demonstrates modulation of the CDW only if the intensity of the higher-order peaks exceeds that calculated for a purely sinusoidal PLD.

The second point we wish to make concerns the magnitude of higher-order CDW peaks. From Eq. (4.9) the intensity can be evaluated at a particular peak.

$$I(G + mk_{cdw}) = [f(G + mk_{cdw})]^2\{J_m[(G + mk_{cdw})A]\}^2. \qquad (4.10)$$

If we ignore the k dependence of f(k) and assume A is small, then[1]

$$\frac{I(G + mk_{cdw})}{I(G)} \approx \left\{\frac{[(G + mk_{cdw})A]^m}{m!2^m}\right\}^2 . \qquad (4.11)$$

Thus the ratio for a second-order CDW satellite with parent Bragg peak at G_a (but located near a Bragg peak at G) is

$$\frac{I(G_a + 2k_{cdw})}{I(G)} \approx \frac{[(G_a + 2k_{cdw})A]^4}{64} \qquad (4.12)$$

and for a third-order satellite with parent Bragg peak G_b the ratio is

$$\frac{I(G_b + 3k_{cdw})}{I(G)} \approx \frac{[(G_b + 3k_{cdw})A]^6}{2304} \quad . \tag{4.12}$$

In 1T-TaS_2, the PLD amplitude, A, is about 0.2 Å for Ta atoms[3,13] and the reciprocal lattice vector magnitude, a*, is about 2 $Å^{-1}$.[1] Therefore $(G_a + 2k_{cdw})A$ and $(G_b + 3k_{cdw})A$ are approximately equal to 0.4 (In each case we chose G_x so that $G_x + mk_{cdw} \approx a^*$). Finally,

$$\frac{I(G_a + 2k_{cdw})}{I(G)} \approx 4 \times 10^{-4} \qquad \text{and} \tag{4.13a}$$

$$\frac{I(G_b + 3k_{cdw})}{I(G)} \approx 2 \times 10^{-6} \quad . \tag{4.13b}$$

In the sinusoidal PLD case, a second-order satellite, though weak, is not necessarily insignificant. This will be of great importance in chapter 7 where we measure first and second-order CDW peaks in the I phase to determine whether there is a modulation of the CDW. The calculated third-order peak intensity is infinitesimal. In our investigation of the T phase we measure with x-rays satellites near first-order CDW peaks. These peaks may be indexed as third-order CDW peaks with a different parent Bragg peak from the first-order CDW peak. Given the exceedingly small intensity for third-order CDW peaks in the sinusoidal PLD case, any significant intensity at the third-order peak is evidence of a nonsinusoidal CDW.

References

1. C. B. Scruby, P. M. Willaims and G. S. Parry, Philos. Mag. **31**, 255 (1975).
2. T. Ishiguro and H. Sato, Phys. Rev. B **44**, 2046 (1991).
3. L. D. Chapman and R. Colella, Phys. Rev. B **32**, 2233 (1985).
4. J. A. Wilson, F. J. DiSalvo and S. Mahajan, Adv. Phys. **24**, 117 (1975).
5. H. A. Mizes, S. Park and W. A. Harrison, Phys. Rev. B **36**, 4491 (1987).
6. R. J. Colton, S. M. Baker, R. J. Driscoll, *et al.*, J. Vac. Sci. Tech. A **6**, 349 (1988).
7. The reader may be curious about the appropriateness of the choice of a lattice constant as the offset vector to the two images. This choice is justifiable for the same reasons that the choice of the graphite lattice constant was justifiable in the original work of Mizes et al. (1987). First of all, it produces images most like those observed in real STM data. Second, it is reasonable that a small flake of the sample material adhered to the tip and acted as the tunneling tip, thereby providing several atoms separated by the sample lattice constants.
8. W. L. McMillan, Phys. Rev. B **14**, 1496 (1976).
9. K. Nakanishi and H. Shiba, J. Phys. Soc. Jpn. **43**, 1893 (1977).
10. K. Nakanishi, H. Takatera, Y. Yamada, *et al.*, J. Phys. Soc. Jpn. **43**, 1509 (1977).
11. K. Nakanishi and H. Shiba, J. Phys. Soc. Jpn. **53**, 1103 (1984).
12. G. F. Giuliani and A. W. Overhauser, Phys. Rev. B **23**, 3737 (1981).
13. L. D. Chapman and R. Collela, Phys. Rev. Lett. **52**, 652 (1984).

Chapter 5

Nearly commensurate CDW domain structure in 1T-TaS_2

5.1 Introduction

As discussed in chapter 4, theoretical calculations based on x-ray diffraction data of 1T-TaS_2 for the NC phase predict that the CDW is arranged in domains separated by discommensurations (see Fig. 5.1). The model[1,2] predicts hexagonal domains with a period of about 70 Å at room temperature. The size of the predicted domains is a function of temperature because the CDW wave vector varies with temperature. The calculations show that the CDW will exhibit amplitude as well as phase modulations, with the CDW amplitude greater in the center of the domains where it is commensurate and lower at the discommensurations where the CDW undergoes a phase slip of one atomic lattice unit (a_o). Although the model includes adjustable parameters, it should be noted that the main attributes of the model are fixed, and it makes explicit predictions for the modulation of the CDW amplitude and phase. However, the model does not require a CDW that locks in to the commensurate wave vector inside the domains. The model can encompass cases ranging from very slight variations from a uniform orientation to a fully locked-in orientation where the CDW becomes fully commensurate within the domains.

Many experiments looking for evidence of these domains and discommensurations have been performed. Before the invention of STM, x-ray diffraction studies[3,4] not only supported the domain models, but also provided the original data upon which these models were based. The x-ray photoemission study of Hughes and Pollack[5] was for many years the only other piece of experimental evidence supporting the domain model. Their study showed that the x-ray photoemission spectrum of the 4*f* lines of the Ta atoms are split in the NC phase (as they are in the C phase), indicating at least two distinct inequivalent sites for the Ta atoms, rather that a continuum of sites (which should produce unsplit 4*f* Ta lines broader than those seen in

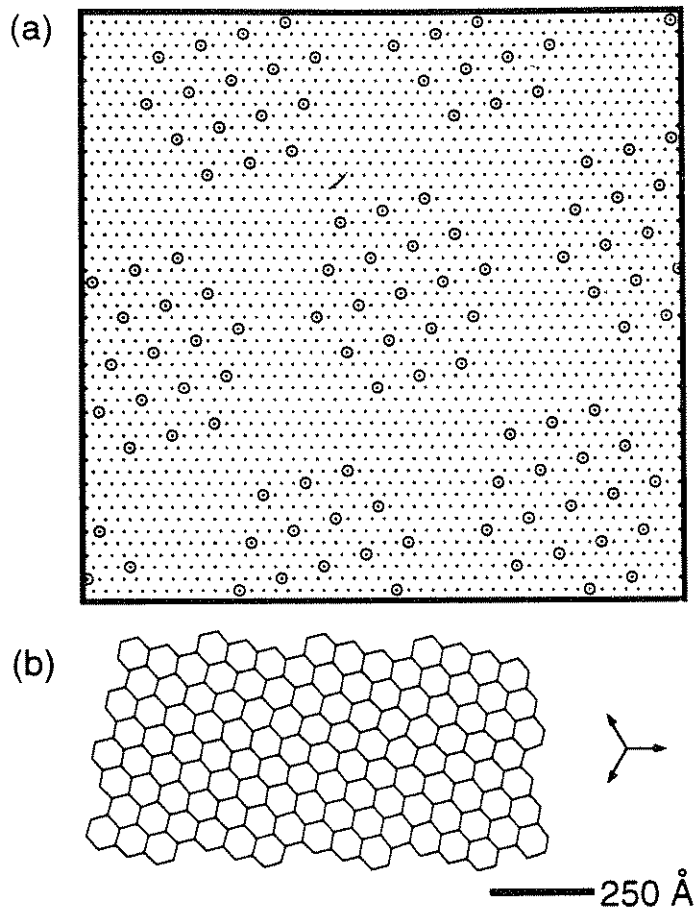

FIG. 5.1 Schematic of model proposed by Nakanishi and Shiba[1,2]. (a) Small scale structure of NC phase model showing registration of CDW maxima (open circles) relative to the Ta lattice (small dots). (b) Large scale structure of NC phase model illustrating size and orientation of domains; solid lines are domain walls. Crystal lattice vectors are indicated at right. (Figure provided by Ruth Thomson)

the C phase) that one would expect for a uniformly incommensurate CDW. However, three high resolution electron microscopy studies[6-8] that achieved atomic resolution on the NC phase of 1T-TaS_2 reported that the CDW was locally incommensurate in contradiction with the discommensuration theories.

In 1988 the first STM study that considered the question of the existence of domains in 1T-TaS_2 was published[9,10]. This study found no clear evidence for domains in the NC phase. In a subsequent study, Gammie et al.[11] reported observing point discommensurations in the NC phase, in contrast with both the domain theory of Nakanishi and Shiba[1,2] and the previous idea of a uniformly incommensurate CDW. Later, Wu and Lieber[12-14] observed domain-like structure in real space STM images of the NC phase with amplitude and phase modulation in apparent agreement with the theoretical predictions. More recent STM and atomic force microscopy measurements by Giambattista et al.[15], Slough et al.[16,17], and Garnæs et al.[18] showed evidence for an amplitude modulated domain structure in the NC phase but suggested that the CDW in this phase is continuously incommensurate across most of the sample and thus does not exhibit sharp discommensurations. However, all of these studies analyzed real space STM images which are inadequate to distinguish true CDW modulations from interference between the CDW and the atomic lattice.[19] Finally, Coleman et al.[20] argued that the relative phases of the CDW maxima and the atomic lattice in the center of the apparent domain structure demonstrate that the observed domains are true domains and not interference effects.

Below we describe extensive STM studies of 1T-TaS_2 over the full temperature range of the NC phase. We use computer generated simulations of STM images both with and without a superimposed domain structure to elucidate the most important features for distinguishing between the two cases. We show that an examination of the fine satellite structure in the Fourier transform is an unambiguous method for conclusively proving the presence of the true phase and amplitude modulation in the NC

phase. We determine the temperature dependence of the domain size and orientation which we use to evaluate proposed domain superstructures.

5.2 Computer simulations

We have generated computer simulations of STM images of the NC phase with and without the presence of domains and discommensurations. First we consider the case where there are no amplitude or phase modulations present in the simulated CDW. Figure 5.2(a) shows such an image. This image was generated by superimposing three sine waves that represent the atomic lattice and three additional sine waves that produce the uniformly incommensurate CDW. The atomic lattice constant (a_o = 3.346 Å) and the CDW wavelength (λ_{CDW} = 11.74 Å) have been chosen to agree with those in the NC phase at room temperature measured by x-ray diffraction. We constructed the CDW to be at an angle relative to the lattice of Φ = 11.8°, which is the value of Φ at room temperature measured by x-ray diffraction[21], and chose the amplitude of the CDW sine waves to be three times the amplitude of the atomic lattice sine waves, in agreement with the amplitude ratio suggested by real STM images[22].

The method of construction of this image becomes more clear upon examination of the Fourier transform, shown in Fig. 5.2(b). This figure clearly shows that the only Fourier components in the image are at the fundamental frequencies of the CDW and the lattice. Nevertheless, by modifying the gray scale in the real space image, we resolved apparent "domains", caused by the beating of these two sets of frequencies. Figure 5.2(c) is identical to Fig. 5.2(a) except that the cut-off level for the gray scale on the computer screen was adjusted to emphasize only the brightest points in the image. This procedure of modifying the computer gray scale to emphasize certain important properties of STM images has been routinely applied to real sample data by many authors, and has resulted in most of the published STM images used for investigating domains in 1T-TaS_2.

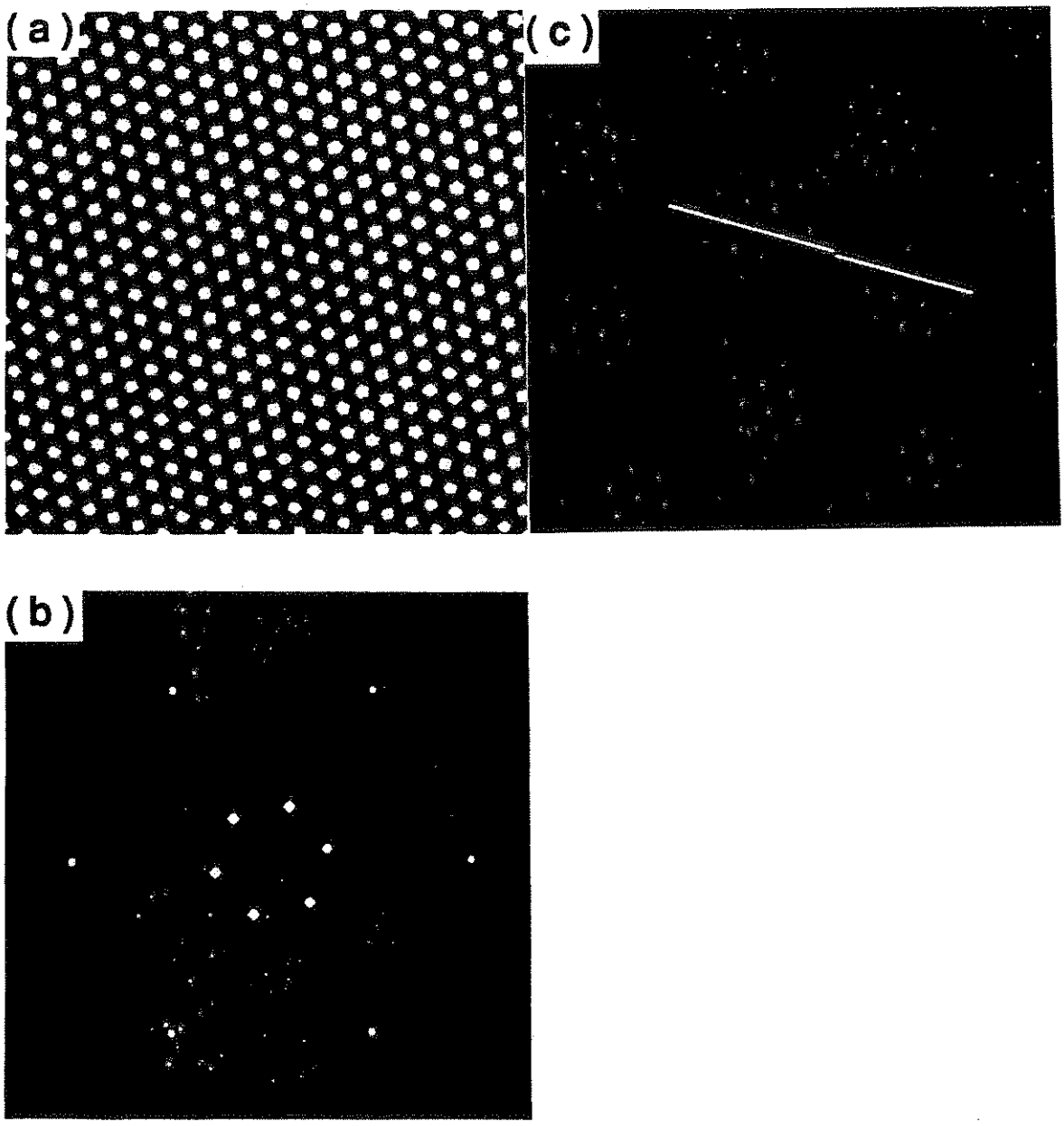

FIG. 5.2 Computer generated simulation of STM image for the case where there are no domains or discommensurations in the NC phase. (a) Real space image. (b) Fourier transform of (a). The six spots near the center of the transform correspond to the CDW in the real space image, whereas the six fainter spots further from the center correspond to the atomic lattice in the real space image. (c) Identical to (a) except that computer gray scale has been modified to emphasize false "domains". White lines have been drawn through CDW maxima in adjacent domains to illustrate the phase shift of one lattice constant. (Figure provided by Ruth Thomson)

XBB 900-10069B

A close inspection of Fig. 5.2(c) will reveal that the CDW appears not only to exhibit amplitude domains, but the moiré pattern also produces apparent phase slips between the false domains. Apparent domains and phase slips are present even though the image represents a uniformly incommensurate CDW with no inherent domain structure whatsoever. These false "domains" and apparent phase slips are solely due to the interference (or beating) between the CDW and the underlying lattice which produces the observed moiré pattern.

Indeed, all of the characteristics of CDW amplitude and phase modulations that have been described in previous STM studies can be observed in the moiré pattern in Fig. 5.2(c). The apparent amplitude modulations can be observed by adjusting the computer gray scale. The apparent phase modulation can be seen by sighting along a line of CDW maxima at a glancing angle. The maxima in adjacent false domains do not appear to be collinear; the interference of the two lattices creates an apparent phase shift of one lattice constant between each "domain" and an adjacent one. This effect is emphasized by the lines drawn on Fig. 5.2(c) in two adjacent false domains. The size and orientation of the domains in the moiré pattern both agree with the values predicted by Nakanishi and Shiba's discommensuration model. This is in no way unexpected. These values are dictated by the values of the CDW wave vectors known from x-ray diffraction studies and used in the calculation of the discommensuration model. The moiré pattern even causes the CDW to appear at the commensurate angle (13.9°) inside a single "domain" [this is determined by measuring the angle relative to the lattice of the lines in Fig. 5.2(c)].

It is illuminating to contrast Fig. 5.2 with Fig. 5.3. Figure 5.3(a) is a computer simulation generated in the same way as Fig. 5.2 except that now the amplitude and phase modulations predicted by Nakanishi and Shiba have been added to the image. These are most easily seen in Fig. 5.3(b), which is a Fourier transform of the real space image shown in Fig. 5.3(a). In this case, a set of reasonably intense satellite spots ring

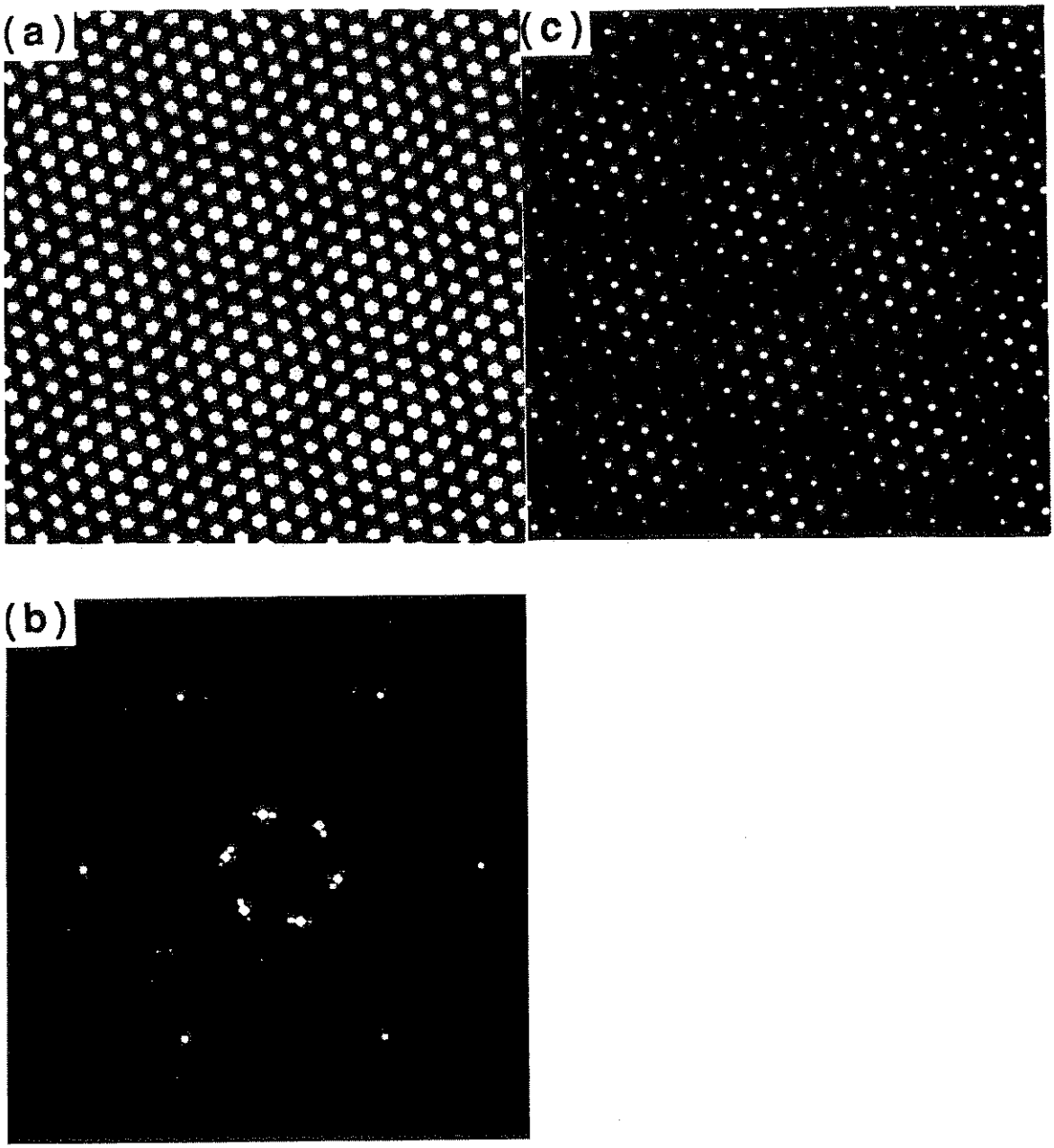

FIG. 5.3 Computer generated simulation of STM image for the case where there are true domains and discommensurations in the NC phase. (a) Real space image. (b) Fourier transform of (a). (c) Identical to (a) except that computer gray scale has been modified to emphasize domains. (Figure provided by Ruth Thomson)

each of the fundamental CDW peaks[23]. Such satellites are always present when the CDW exhibits true domains and discommensurations. These satellites vary in intensity, and not all six possible first-order satellites are present. Those present in Fig. 5.3(b) were chosen to agree with those predicted from the honeycomb model of Nakanishi and Shiba in both location and intensity.

Figure 5.3(c) is the same as Fig. 5.3(a) except for an adjustment of the computer gray scale. By comparing Fig. 5.2(c) and 5.3(c), one sees that unequivocal determination of the presence of amplitude domains and discommensurations in the CDW in 1T-TaS_2 from real space STM images is extremely difficult. However, it is equally apparent from Figs. 5.2(b) and 5.3(b) that the Fourier transform of the real space image provides an easy method for reliable discrimination between the two cases.

Previous STM studies by other workers have relied solely on real space STM images to attempt to identify CDW amplitude and phase modulations. Since the authors did not adequately account for the interference effect of the two lattices, the conclusions are questionable. The tests used for the determination of the presence of domains have included: (1) looking for variations in the CDW amplitude[12-18,20], (2) sighting along rows of CDW maxima in the real space image to look for phase slips[11-14], (3) measuring the local angle of the CDW relative to the lattice of the real space image and comparing it to the commensurate angle of 13.9°[9,10,12-14,16,17], (4) examining the fine structure of the real space images of the CDW to find areas where the CDW maxima or minima appear identical thus proving local commensurability[9,10,12-15], (5) measuring the apparent domain size and orientation to see that they agree with those predicted theoretically[12-14], (6) examining the Fourier transform of the real space data for a peak at the commensurate wave vector[18], and (7) examining the apparent phase of the CDW and the atomic lattice at the center of the apparent domains to distinguish between true domains and interference artifacts[20].

Of these tests, (1), (2), and (3) fail because, as shown in Fig. 5.2(c), the moiré pattern passes them so they do not prove the existence of true domains. In addition, tests (3) and (4), are faulty because they check only for a fully locked-in domain structure. It is interesting to note that different authors have reached opposite conclusions about the real space images using these second two tests[24]. Test (5) fails because the apparent domains produced by the moiré pattern must have the same size and orientation as true domains would, so this test cannot be used to differentiate between them. Test (6) fails because a peak at the commensurate wave vector is not expected even in the domain model. Test (7) generally fails because the apparent phase of the CDW and the atomic lattice can be altered in a indeterminate way in an STM image that is produced by simultaneously tunneling to several atoms on the tip, a common occurrence, as explained in the section on the C phase CDW in chapter 4. Indeed, the first published[12-14] atomic resolution image purporting to show the domain structure in the NC phase does not show the expected registration at the domain centers [as shown in Fig. 4.5(a)], but instead shows a four atom CDW maximum similar to that shown in Fig. 4.5(b).

5.3 Identification of true domain structure in the NC phase

We have imaged 1T-TaS_2 with an STM (constant height mode, typically with tip bias = -10 mV, tunnel current = 3 nA), using high quality samples grown in our laboratory and at Cornell University. Figure 5.4(a) is an unfiltered image of 1T-TaS_2 in the NC phase at T = 295 K. On the scale of this image, atoms are not clearly visible; the smallest discernible features are CDW maxima. A periodic brightness variation is observed, similar to that reported in previous studies (and attributed there to domain-like modulations). As emphasized previously, these real space modulations do not in themselves demonstrate true CDW domain structure. Figure 5.4(b) shows the two-dimensional Fourier transform of the data of Fig. 5.4(a). In the Fourier transform image of Fig. 5.4(b), a hexagonal reciprocal lattice is observed with the six large peaks,

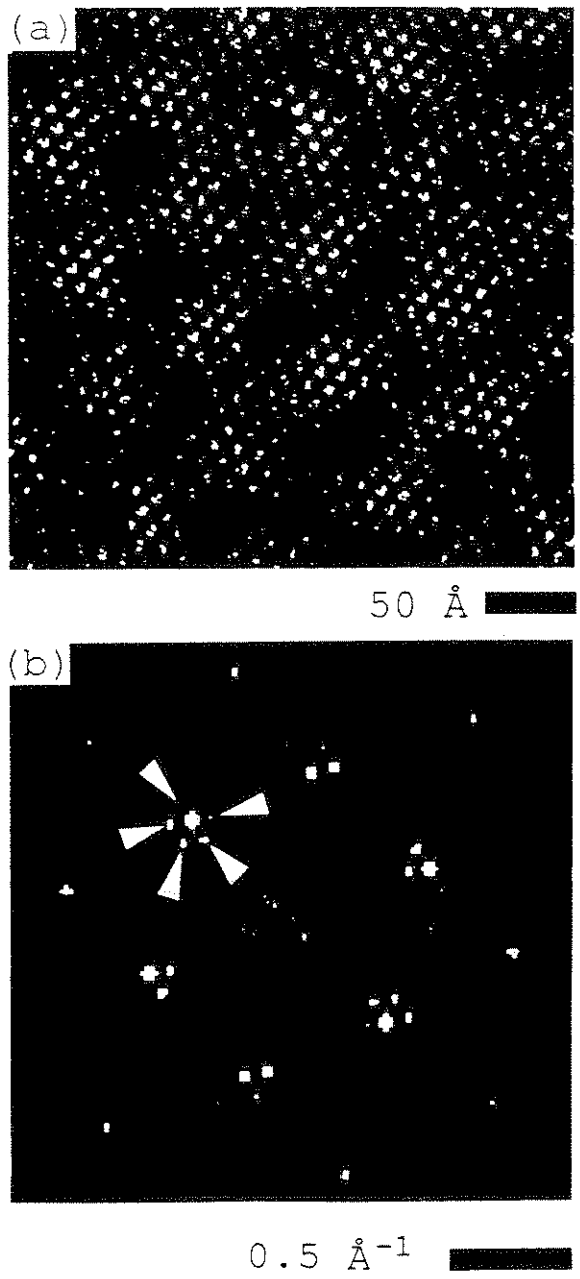

FIG. 5.4 (a) STM image of 1T-TaS_2 obtained at T = 295 K in NC phase. (b) Fourier transform of (a). Satellite spots near hexagonally arranged CDW peaks are clearly evident; arrows identify five such spots. Different satellite spots have different intensities, consistent with theoretical predictions.

corresponding to the fundamental CDW frequencies, surrounding the center (the hexagon is slightly distorted due to thermal drifts and imperfections in the piezoelectric scanning tube). Surrounding each fundamental CDW peak, there are several satellite spots, some of which are identified by small arrows in the figure. Satellite spots are also evident around higher order CDW peaks. It is important to note that different satellite peaks associated with a given CDW fundamental have different intensities. This is not an imaging artifact, but rather implies an amplitude *and* phase modulation of the CDW and that the CDW amplitude modulation envelope is not purely sinusoidal.

Using the measured Fourier coefficients of a first order CDW peak and its first order satellites together with the CDW peak and satellite positions, we can reconstruct the real space phase and amplitude modulation function of one of the three simultaneously occurring CDW's, as shown in Figs. 5.5(a) and 5.5(b) (See Appendix B for an explanation of this procedure). Figures 5.5(a) and 5.5(b) show that the domain structure has a real space wavelength (measured through the centers of domains) of 72 ± 3 Å, and that the CDW is close to being commensurate over an appreciable part of the domain. The CDW amplitude is modulated with a fractional modulation amplitude of about 0.44. The troughs of the amplitude modulation envelope are distinctly narrower than the crests. Hence, as already demonstrated by the satellite intensity pattern, the CDW amplitude modulation is not strictly sinusoidal. The domain boundaries are not sharp, but rather comprise more than 50% of the domain dimension. In going from one domain to the next, the CDW phase slips by a factor of $\delta\phi = 0.61\pi \pm 0.03\pi$ rad, which corresponds favorably with the theoretically predicted[1,2] phase slip of $\delta\phi = 0.615\pi$ rad. To compare our data with the theory further, we have calculated the real space phase and amplitude variations from the theory of Nakanishi and Shiba, using their predictions for the Fourier coefficients of the modulation function[1,2] at 295 K. The results of those calculations, shown in Figs. 5.5(c) and 5.5(d), are in excellent agreement with those reconstructed from our data.

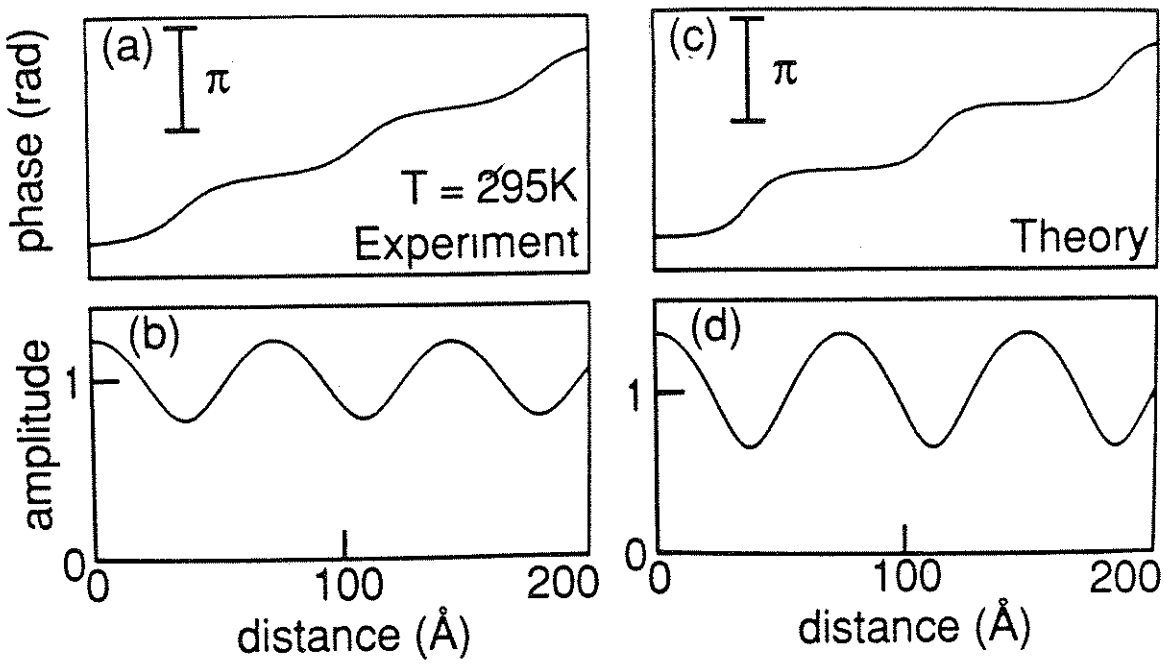

FIG. 5.5 (a) Real space phase variation and (b) amplitude modulation A/A_{avg} of the CDW in 1T-TaS_2 in the NC phase reconstructed from the Fourier coefficients and wave vectors extracted from the Fourier transform of Fig. 5.4(a). (c) Real space phase variation and (d) amplitude modulation A/A_{avg} of the CDW predicted by the Nakanishi and Shiba theory.

To test for a true lock-in of the CDW in the commensurate region inside domains, we have examined our FTs for second-order satellite spots. These second-order spots would have to be present for a complete lock-in to exist, because then the total complex modulation envelope (as distinguished from the amplitude or phase part of the modulation envelope) would have to deviate from a sine wave. We found that at the locations of the potential second-order satellites, the amplitude of the FT is < 2% of the amplitude of the CDW fundamental peak. This value is five times smaller than the expected amplitude of the strongest second-order satellite in the case where the CDW has locked-in over the entire domain[1,2]. From this we conclude that the CDW phase varies over a significant portion of the domain in the NC phase and therefore should not be considered to exhibit true lock-in. This conclusion can be verified by a close examination of Fig. 5.5(a). Although the CDW amplitude clearly varies from inside the domain to the domain wall, it never flattens out at a constant height inside the domain, as would be the case for a locked-in CDW. Likewise, as illustrated in Fig. 5.5(b), the CDW phase does not become constant inside the domains, although its phase does change much more slowly in the center of the domains than at the discommensurations.

We have Fourier analyzed STM images of 1T-TaS_2 from different preparation batches and find results consistent with those described above. Although the modulation functions displayed in Figs. 5.5(a) and 5.5(b) are representative of the NC phase at room temperature, there are variations of roughly 10% in the phase slip, modulation amplitude, and domain boundary size evaluated from different images. Gross sample defects tend to destroy the domain structure. We have also performed similar Fourier transform analyses on STM images obtained on 1T-TaS_2 at different temperatures. For the NC phase, the domain structure is found to be temperature dependent in a manner consistent with predictions of the domain model[1,2].

5.4 Temperature dependence of NC phase domain structure

In the NC phase, the CDW is oriented relative to the atomic lattice at an average angle Φ that is less than the commensurate angle of 13.9°. This temperature dependent angle and the CDW wavelength are the factors which determine the size of the domains predicted by Nakanishi and Shiba[1,2]. At the higher temperatures, the predicted domains are only a few CDW wavelengths across, reducing the number of CDW maxima or minima inside the domain to about seven. This can be seen in Fig. 5.6(a), an STM image of 1T-TaS_2 taken at 343 K. Figure 5.6(b) is the FT of Fig. 5.6(a). Similarly, Figs. 5.6(c), (e),(g), and (i) are the real space STM images at 295 K, 275 K, 225 K, and 215 K, respectively, and Figs. 5.6(d), (f), (h), and (j) are their respective FTs. These figures clearly prove that the CDW in the NC phase is arranged into domains separated by diffuse discommensurations as predicted by Nakanishi and Shiba *at all temperatures* within the NC phase. Strong satellite spots are discernible in each of the Fourier transforms, unequivocally proving the existence of a discommensurate structure. The locations of the satellites, and even which of the satellites is the most intense, are consistent with those expected from the honeycomb model[1,2] [see Fig. 5.3(b)]. In addition, as shown in Fig. 5.7, by using the coordinates and intensities of the satellites, we have constructed graphs of the CDW amplitude, phase relative to a commensurate CDW, and the derivative of the phase at each temperature. These graphs clearly show areas where the CDW phase is nearly constant (i.e. the CDW is commensurate) and the CDW amplitude is enhanced, separated by regions of decreased CDW amplitude and rapidly changing phase (the discommensurations)[25].

Using the graphs of the derivative of the CDW phase vs. distance we have extracted the domain periodicity for each temperature (averaging over at least five images at each temperature). The data at 225 K were not included in this and the following figures because we had too few high-quality images. Figure 5.8(a) is a graph of the

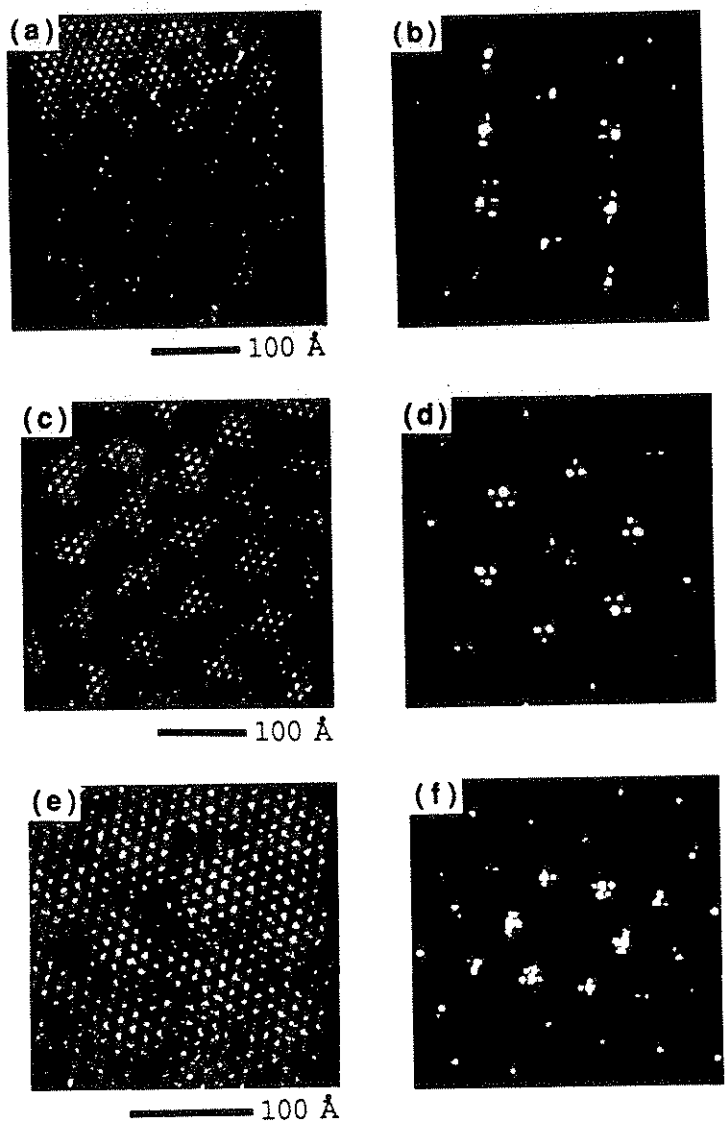
(a)
(b)
100 Å
(c)
(d)
100 Å
(e)
(f)
100 Å

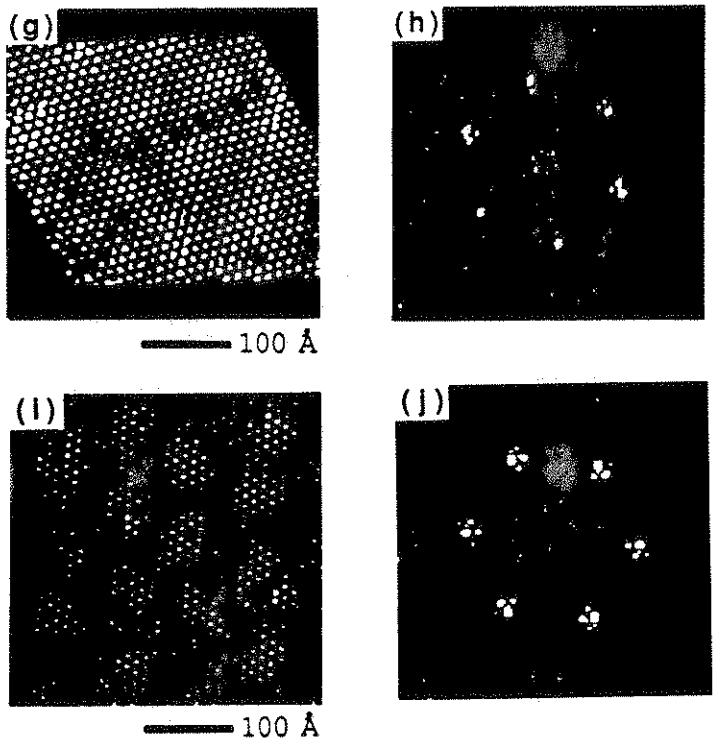

FIG. 5.6 (a) STM data at 343 K. (b) FT of (a). (c) STM data at 295 K. (d) FT of (c). (e) STM data at 273 K. (f) FT of (e). (g) STM data at 225 K. (h) FT of (g). (i) STM data at 215 K. (j) FT of (i). Central regions of the FTs are enlarged by a factor of two for better clarity of the satellite spots. (Figure provided by Ruth Thomson)

XBB 915-3954B (a–j)

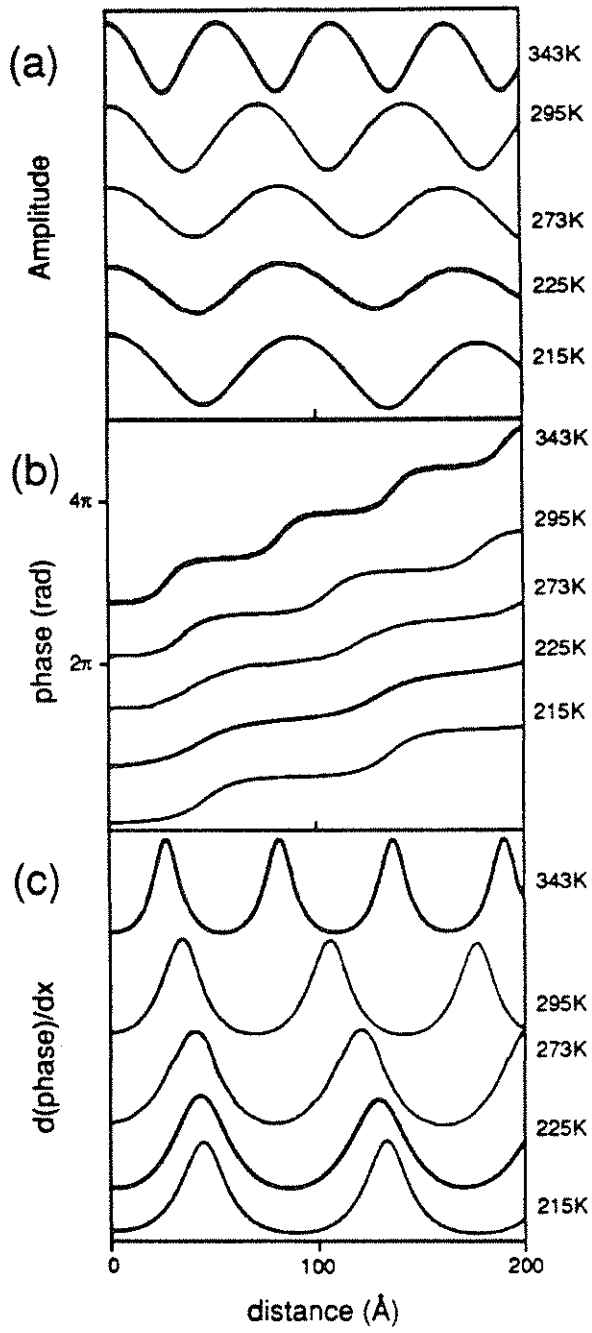

FIG. 5.7 Graphs generated from coordinates and intensities of the satellites in the FTs shown in Fig. 5.6; (a) CDW amplitude vs. distance, (b) CDW phase vs. distance, (c) derivative of CDW phase vs. distance. (Figure provided by Ruth Thomson.)

XBL 934-432

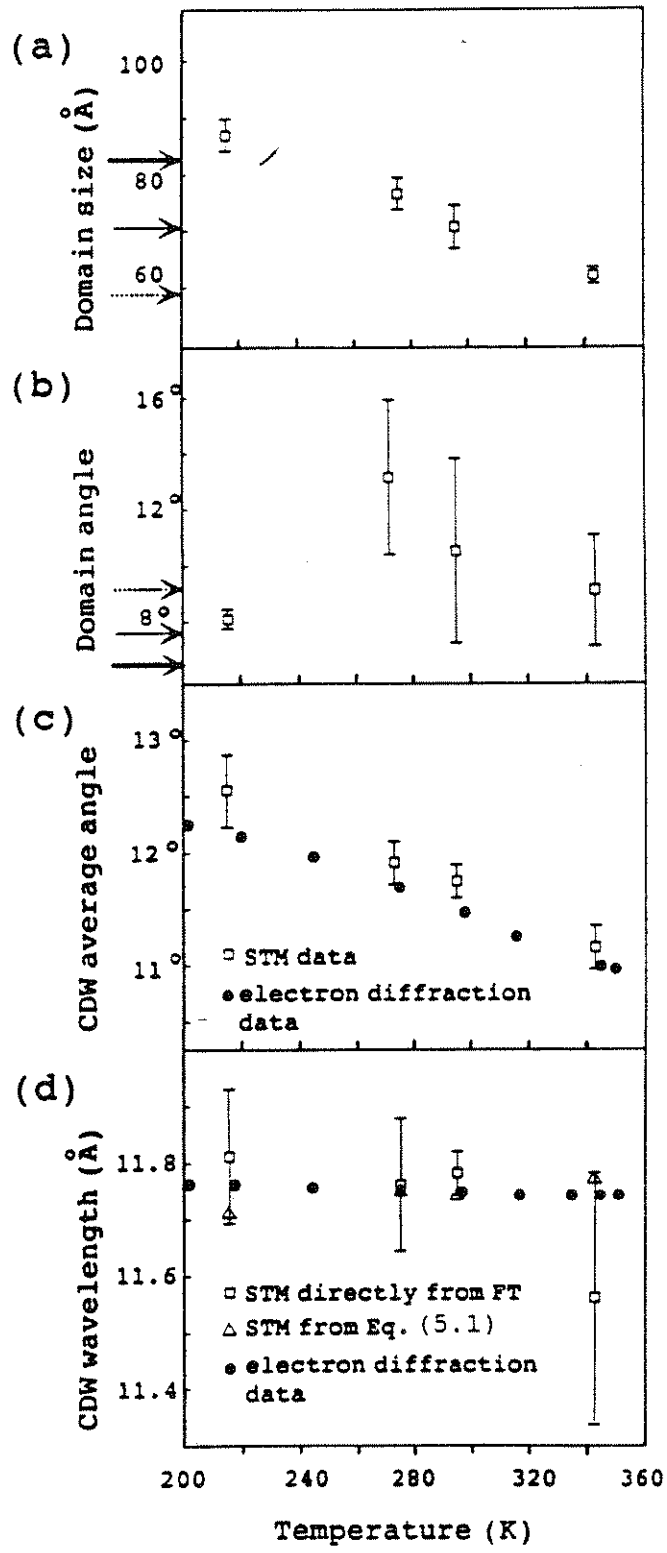
(a)
Domain size (Å)
100
80
60
(b)
Domain angle
16°
12°
8°
(c)
CDW average angle
13°
12°
11°
STM data
electron diffraction data
(d)
CDW wavelength (Å)
11.8
11.6
11.4
STM directly from FT
STM from Eq. (5.1)
electron diffraction data
200
240
280
320
360
Temperature (K)

FIG. 5.8 Plots of CDW parameters for the NC phase measured from STM FTs. (a) Domain period versus temperature. (b) Domain angle versus temperature. (c) Average angle of the CDW relative to the lattice as a function of temperature (open squares) compared with previously published electron diffraction measurements (solid circles)[6]. (d) Wavelength of the CDW measured directly from the FT (open squares), and calculated from the measured CDW angle and domain periodicity (open triangles). Also plotted are results of an electron diffraction study (solid circles)[6]. Significance of the arrows in (a) and (b) is explained in text. (Figure provided by Ruth Thomson.)

domain period vs. temperature for our data. Within experimental uncertainty, the domain period increases linearly with decreasing temperature.

Besides domain period, the other characteristic that completely specifies the nature of the CDW domains is domain orientation. We have attempted to measure the orientation of the satellite spots relative to the CDW fundamental spots in the FTs. Unfortunately, because of the small distances between the satellites and the CDW fundamental spots, there is a large degree of uncertainty in these measurements, which are shown in Fig. 5.8(b). However, as will be explained shortly, despite the large uncertainties these measurements are still valuable in determining the precise nature of the CDW domain structure.

We have also measured the locations of the fundamental CDW wave vectors directly from the FTs. A comparison of our measurements (again averaged over at least five images at each temperature) of the CDW angle relative to the lattice with the measurements of Ishiguro and Sato's electron diffraction study[6] is shown in Fig. 5.8(c). Note in Fig. 5.8(c) that , if the linear trend that we observe down to 215 K continues down to the transition temperature T = 183 K, the CDW angle Φ will not make a continuous transition to the commensurate angle of 13.9° at the transition temperature. This is in agreement with the work of Ishiguro and Sato[6], who measured a sharp jump in Φ at 183 K when they lowered the temperature of the sample.

Assuming that the domain periodicity occurs at the lattice and CDW beat frequency, a simple relation between the domain periodicity, the CDW angle, and the CDW wavelength is given by

$$\text{Domain Period} = \frac{a_o}{\sqrt{\left(\frac{2\pi\delta\Phi}{360}\right)^2 + \left(\frac{\delta\lambda}{\lambda}\right)^2}} \ , \qquad (5.1)$$

where $\delta\Phi$ is the difference between Φ and $\Phi_{commensurate} = 13.9°$ and is given in degrees, and $\delta\lambda$ is the difference between the observed λ and $\lambda_{commensurate} = 12.06$ Å. This formula is derived in Appendix C. We can check the consistency of our results by comparing the CDW wavelength obtained from direct measurements of the FT and that calculated from Eq. (5.1). This comparison is plotted in Fig. 5.8(d). The wavelengths obtained by these two methods agree to within our experimental uncertainty; in addition these agree with those measured by electron diffraction[6]. Within our experimental uncertainty, the CDW wavelength does not appear to vary with temperature and has an average value of 11.73 ± 0.11 Å which is in excellent agreement with the results of Ishiguro and Sato[6], who found the CDW wavelength was nearly constant in the NC phase with a value of about 11.75 Å.

By combining Fig. 5.8(a) and 5.8(c) we discover a subtle but interesting point about the nature of the discommensurations present in these images. To understand this point, however, it is first necessary to discuss the two possible configurations for a CDW discommensuration: the discommensuration that "compresses the CDW wavelength and the one that "expands" the CDW wavelength.

When the CDW undergoes a discommensuration, it is required to slip one atomic lattice unit. However, the exact direction of this slip is not necessarily determined. Figure 5.9(a) is a schematic illustrating the two most likely choices for the direction of the slip. At the phase slip between adjacent domains, the CDW maximum which would have coincided with the atomic position labeled 0 if the CDW had continued in a commensurate manner, will most likely slip to either the atomic position labeled 1 or that labeled 2. (A continuation of the CDW from the center of a domain to the phase slip at the average CDW periodicity would place a CDW maximum roughly in the center of the triangle defined by the atomic positions labeled 0,1, and 2.) If it goes to position 1, the CDW wavelength is compressed compared to the commensurate wavelength, whereas if it slips to position 2 the CDW wavelength becomes expanded. Both choices cause the average

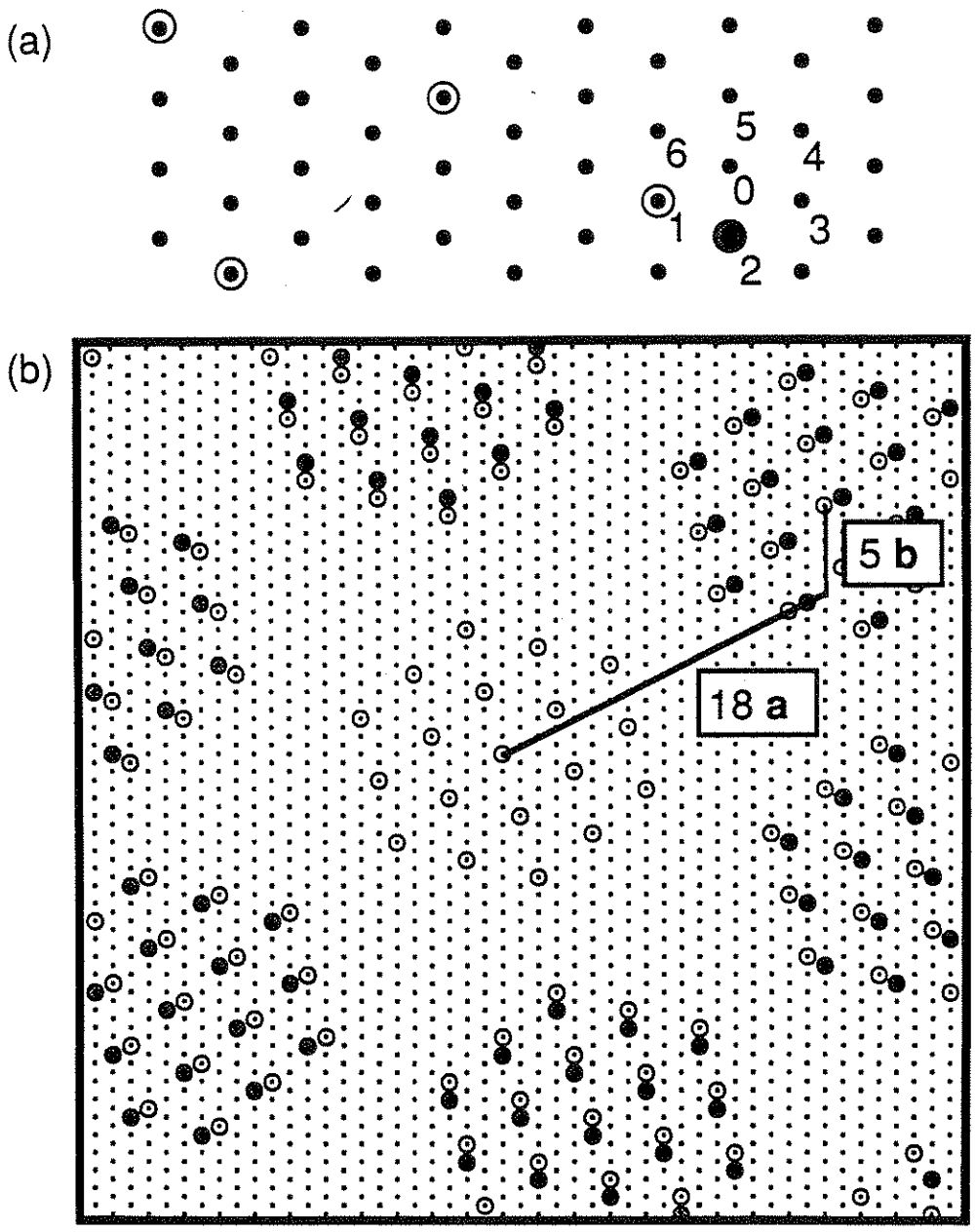

FIG. 5.9 (a) Schematic illustrating possible types of discommensurations. If the CDW maximum slips to atomic position labeled 1, a discommensuration which "compresses" the CDW wavelength results. If the CDW maximum slips to atomic position labeled 2, a discommensuration which "expands" the CDW wavelength results. (b) Schematic illustrating (18 × 5) structure employing compressed discommensurations (open circles) and the (19 × 5) structure employing expanded discommensurations (gray circles). (Figure provided by Ruth Thomson.)

XBL 934-433

CDW angle, Φ, measured over several domains, to be less than the 13.9° commensurate angle, but the different angles resulting from each choice vary slightly. In their analysis of real space STM data, Wu and Lieber concluded that the majority of the discommensurations they observed were of the compressed type[12-14].

If all of the discommensurations of the CDW are of the compressed type, one possibility for the NC phase at room temperature is the (18 × 5) structure, which is technically commensurate with a repeat spacing of 18 lattice units in the **a** direction and 5 in the **b** direction. This is the structure that was shown in Fig. 5.1(a) and is redrawn in Fig. 5.9(b) using the open circles. The similar (19 × 5) structure employs expanded discommensurations and produces a slighty different CDW angle and domain periodicity. This structure is also shown in Fig. 5.9(b) using the gray circles. There exist two families of discommensurate superstructures, one related to the (18 × 5) structure using compressed discommensurations and one related to the (19 × 5) structure using expanded discommensurations. Within one family, the different members differ from each other only by the number of commensurate CDW wavelengths contained within each domain. For example, the next larger member in the (18 × 5) family is (18+3 × 5+1) = (21 × 6) because a commensurate CDW translation is 3**a** + 1**b**. These two families are plotted in Fig. 5.10, [the (18 × 5) compressed family plotted as solid squares and the (19 × 5) expanded family as solid triangles] along with our measurements of the actual CDW angle and domain period that were plotted in Fig. 5.9(a) and (c).

Examination of Fig. 5.10 reveals that the actual discommensurate CDW structure involves both types of discommensurations. Each point plotted in the figure is taken from our data at a different temperature. The highest temperature point (that with the smallest domain periodicity) appears to lie closer to the family of expanded wavelength structures, while the other points lie closer to the compressed wavelength structures. The fact that the lowest temperature point (that with the largest domain periodicity) lies above the line connecting the compressed wavelength structures is not particularly disturbing.

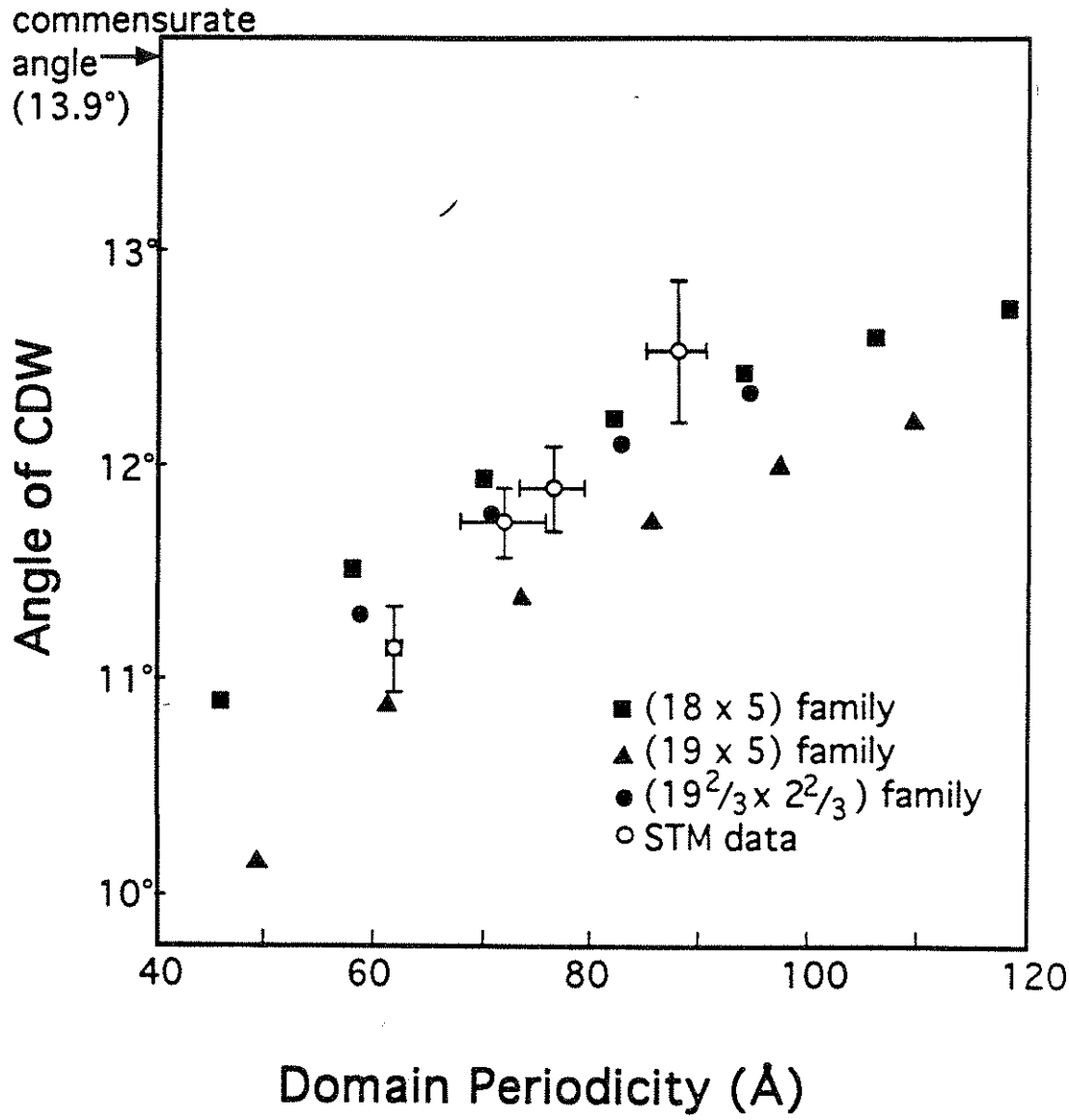

FIG. 5.10 Plot of the experimentally measured angle of the CDW relative to the lattice (determined by the positions of the fundamental CDW peaks in the Fourier transforms of the STM images) versus the domain periodicity (determined from the positions of the satellite spots in the Fourier transforms) compared to several possible domain families. (Figure provided by Ruth Thomson.)

XBL 934-434

There are several other possible discommensurations, including one in which the CDW shown in Fig. 5.9(a) would slip to the atomic lattice position labeled 3. This choice would result in a structure with an angle much closer to the commensurate angle of 13.9° at the same domain periodicity when compared to the other two families described. A combination of different types of discommensurations between different domains would produce an intermediate structure with angle and domain periodicity values similar to those we measure.

The last question to consider in the analysis of the precise nature of the domain structure in the NC phase is the orientation of the domains. Wilson[26] has published an exhaustive theoretical study analyzing previous STM and electron diffraction data to determine the precise superstructure of the CDW in the NC phase. He concludes that the CDW at room temperature is arranged in a (19 2/3 × 2 2/3) rotated honeycomb array which is closely related to the (18 × 5) array shown in Fig. 5.9(b). The most striking difference between these two superstructures is the orientation of the domains relative to the CDW, but the precise values of the average CDW wavelength and orientation are also different. The parameters for the two structures are given in Table 5.1 along with the values we measure for these properties from our STM images at 295 K. It is clear that, to within our experimental uncertainty, our room temperature STM data agree with the (19 2/3 × 2 2/3) structure proposed by Wilson[26].

However, this agreement is not maintained at the other temperatures at which we have taken data. To illustrate this point we have placed small arrows at the values of the domain size and orientation for the (19 2/3 × 2 2/3) family in Figs. 5.8(a) and 5.8(b) to compare with our experimental measurements. In both figures, the bold arrow shows the expected value for the (22 2/3 × 3 2/3) structure (presumably present below room temperature), the middle arrow that of the (19 2/3 × 2 2/3) structure (proposed by Wilson[26] to be present at room temperature), and the dashed arrow shows that of the (16 2/3 × 1 2/3) structure (presumably present above room temperature). The particular

Domain structure	CDW angle, Φ	CDW wavelength, λ(Å)	Domain orientation, relative to CDW
(18×5)	11.93°	11.68	1.96°
$(19\ 2/3 \times 2\ 2/3)$	11.76°	11.72	7.62°
STM data at 295 K	11.73° ± 0.16°	11.78 ± 0.12	10.6° ± 3.3°

Table 5.1 Comparison of STM data at 295 K with domain superstructure models.

discrepancies that we wish to point out are (1) the domain period at 273 K falls exactly between two of the choices of the (19 2/3 × 2 2/3) family, and (2) the two lower temperature domain orientation measurements do not agree with that of the (22 2/3 × 3 2/3) structure. Even so, it should be noted that the domain orientation angles of the (19 2/3 × 2 2/3) family are much closer to the observed angles than those of either the (18 × 5) or the (19 × 5) families, which would all be 3°. As a further check, the family of superstructures related to the (19 2/3 × 2 2/3) superstructure is also plotted in Fig. 5.10 using the small solid circles. When these two parameters (domain period and orientation) are taken together, except at room temperature, none of these structures is within the experimental error of our data points.

In addition, both our STM data and the electron diffraction data of Ishiguro and Sato[6] indicate that the CDW domain structure changes more or less continuously as the temperature is lowered. If the CDW were to adhere strictly to a specified family of superstructures, such as those related to the (19 2/3 × 2 2/3), not only would the size and orientation of the domains be constrained to increase in discrete jumps as one more commensurate CDW wavelength was added to each domain, but, since the CDW average angle and wavelength are also specified for each member of the family, these quantities are also constrained to increase in discrete jumps. Based on the measurements of domain period, we would expect at most four members of the (19 2/3 × 2 2/3) family to be present over the NC phase temperature range. However, the electron diffraction measurements, shown in Fig. 5.8(c), clearly show that the CDW average angle increases smoothly as the temperature is lowered. In addition, the CDW wavelength is expected to vary from 11.67 Å for the (16 2/3 × 1 2/3) structure to 11.80 Å for the (25 2/3 × 4 2/3) structure, while the electron diffraction measurements shown in Fig. 5.8(d) show that the CDW wavelength actually stays between 11.74 Å and 11.76 Å.

Therefore, we believe that, although the CDW domain superstructure appears more closely related to the (19 2/3 × 2 2/3) family than to other structures such as the (18

$\times$ 5) family, our STM data do not support the conclusion that the CDW superstructure adheres to any particular family of superstructures, or that it jumps discontinuously from one to the next in a family of superstructures. On the contrary, even in the real space STM images the CDW domains appear to be nonuniform [see Figs. 5.6(a), (c), (e), (g), and (i)], with some domains appearing to be of unusual sizes or off-center relative to the other domains in a single image.

One final point about the CDW structure in the NC phase is that, contrary to Ishiguro and Sato[6], who described the NC phase as having domains only on warming from the T phase, we find that the domains and discommensurations as evidenced by the satellite structure are present in the NC phase both when the sample is cooled from the I phase and when it is warmed above the T phase. We heated a single sample to 390 K for 48 hours to insure that the CDW would be in the I phase and then allowed it to cool to room temperature. After verifying the existence of the satellite spots in the FT, we then cooled it to 77K for 48 hours and again checked for satellite spots after warming it up to room temperature. Two examples of our FTs showing clear satellite spots both upon warming and cooling are shown in Fig. 5.11[27]. Our measurements are not precise enough to discern the differences in the CDW wavelength and angle when data are taken at the same temperature but on different sides of the hysteretic curve of 1T-TaS_2, as reported by Ishiguro and Sato[6]. However, we can confidently say that domains and discommensurations are present at room temperature regardless of the thermal history of the sample.

5.5 Conclusion

In summary, in the NC phase of 1T-TaS_2 we have shown unequivocally that a true discommensurate domain structure exists in close agreement with that predicted by Nakanishi and Shiba, and have analyzed this structure at 215 K, 225 K, 273 K, 295 K, and 343 K. The domain size increases monotonically with decreasing temperature, but

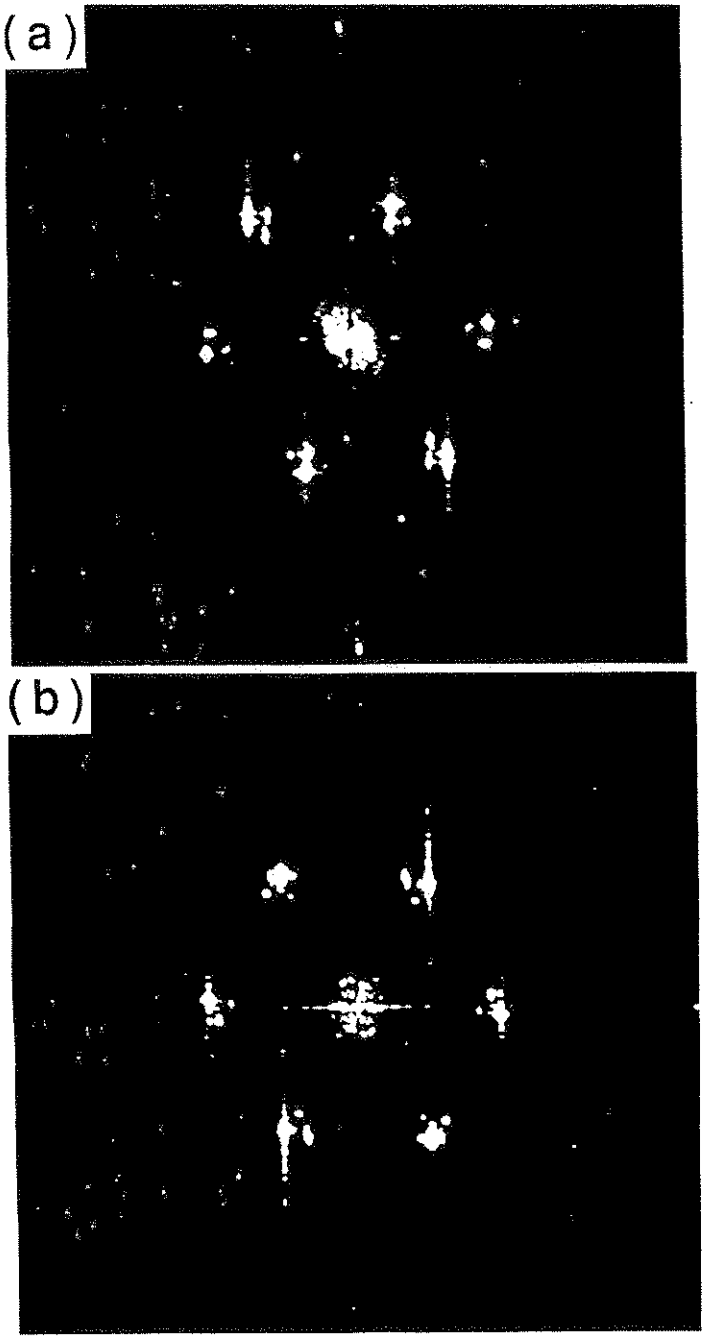

FIG. 5.11 (a) Fourier transform of STM data in the NC phase at 295 K just after sample was cooled from the I phase. (b) Fourier transform of STM data of 1T-TaS_2 in the NC phase at 295 K just after sample was warmed from the T phase. Satellite spots are clearly visible in both FTs. (Figure provided by Ruth Thomson.)

XBB 934-2160

the angle of the CDW relative to the lattice does not continuously approach the commensurate angle at the transition temperature. In addition, we found it unlikely that the (19 2/3 × 2 2/3) structure, or any other rigorously commensurate superstructure, adequately describes the complicated domain superstructure observed in the STM images.

References

1. K. Nakanishi and H. Shiba, J. Phys. Soc. Jpn. **43**, 1893 (1977).
2. K. Nakanishi, H. Takatera, Y. Yamada, *et al.*, J. Phys. Soc. Jpn. **43**, 1509 (1977).
3. S. Tanda and T. Sambongi, Synth. Metals **11**, 85 (1985).
4. Y. Yamada and H. Takatera, Solid State Commun. **21**, 41 (1977).
5. H. P. Hughes and R. A. Pollack, Commun. Phys. **1**, 61 (1976).
6. T. Ishiguro and H. Sato, Phys. Rev. B **44**, 2046 (1991).
7. M. Kuwabara, M. Tomita, H. Hashimoto, *et al.*, Phys. Status Solidi A **96**, 39 (1986).
8. G. v. Tendeloo, J. v. Landuyt and S. Amelinckx, Phys. Status Solidi A **64**, K105 (1981).
9. R. E. Thomson, U. Walter, E. Ganz, *et al.*, J. Microsc. **152**, 771 (1988).
10. R. E. Thomson, U. Walter, E. Ganz, *et al.*, Phys. Rev. B **38**, 10734 (1988).
11. G. Gammie, S. Skala, J. S. Hubacek, *et al.*, J. of Microsc. **152**, 497 (1988).
12. X. L. Wu and C. M. Lieber, Science **243**, 1703 (1989).
13. X. L. Wu and C. M. Lieber, Phys. Rev. Lett. **64**, 1150 (1990).
14. X. L. Wu and C. M. Lieber, J. Vac. Sci. Technol. B **9**, 1044 (1991).
15. B. Giambattista, C. G. Slough, W. W. McNairy, *et al.*, Phys. Rev. B **41**, 10082 (1990).
16. C. G. Slough, W. W. McNairy, R. V. Coleman, *et al.*, Phys. Rev. B **42**, 9255 (1990).
17. C. G. Slough, W. W. McNairy, C. Wang, *et al.*, J. Vac. Sci. Technol. B **9**, 1036 (1991).
18. J. Garnæs, S. A. C. Gould, P. K. Hansma, *et al.*, J. Vac. Sci. Technol. B **9**, 1032 (1991).
19. B. Burk, R. E. Thomson, A. Zettl, *et al.*, Phys. Rev. Lett. **23**, (1991).

20. R. V. Coleman, W. W. McNairy and C. G. Slough, Phys. Rev. B **45**, 1428 (1992).

21. C. B. Scruby, P. M. Willaims and G. S. Parry, Philos. Mag. **31**, 255 (1975).

22. B. Giambattista, A. Johnson, W. W. McNairy, *et al.*, Phys. Rev. B **28**, 3545 (1988).

23. Strictly speaking, even a uniformly incommensurate sinusoidal CDW could display "satellite" spots near each of the fundamental CDW peaks. This arises because each lattice Bragg peak will have associated with it not only first order CDW peaks, but also a series of higher-order CDW peaks which originate from local atomic charge density distortions due to the presence of the PLD. High order CDW peaks associated with a given Bragg peak can appear as "satellite" spots belonging to a fundamental CDW peak tied to an adjacent Bragg peak. Calculations show, however, that such "satellites" have a very low intensity and are easily distinguished from the much more intense satellites associated with a true domain structure. For a more complete discussion of the subtle point see chapter 4.

24. Wu and Lieber (1989) conclude that the CDW maxima are identical and are at an angle of 13.9° inside the domains, while Thomson et al. (1988) and Giambattista et al. (1990) conclude that the maxima are not identical and Thomson et al. (1988) and Slough et al. (1990) measure the angle of the CDW from the real space images at room temperature to be around 12° inside the domains.

25. The images in Fig. 5.6 and the derived graphs in Fig. 5.7 are representative of our highest quality images; however, significant variation exists among images from a given temperature. The measured ratio of the strongest satellite amplitude to the CDW fundamental amplitude varies from about 0.75 to 0.25. The variation of this ratio leads to a corresponding variation of the strength of the derived modulation envelopes such as those shown in Fig. 5.7. Multiple tip effects are the most likely

explanation of this variation. Although multiple tip effects do not alter the distribution of the satellites, they may alter their relative intensities.

26. J. A. Wilson, Condens. Matter **2**, 1683 (1990).

27. These two images were taken at NIST, Boulder, Colorado. The software available at NIST does not allow for the apodization of the data before Fourier transforming, so these two FTs are not as clear as the others contained in this thesis.

Chapter 6

Surface and Bulk CDW Domain Structure in the T phase of 1T-TaS_2

6.1 Introduction

In this chapter we continue the investigation of CDW domain structure in 1T-TaS_2. In chapter 5 we described the Nakanishi and Shiba model of CDW domains in 1T-TaS_2 in the NC phase[1,2] and we compared the model to our experimental evidence of true domain structure. As we mentioned in chapter 5, there was some experimental evidence suggesting that domains existed in the NC phase[3,4] although there were some studies which found no evidence of domains[5-7]. However, in the T phase both the theoretical and experimental body of work pertaining to possible domain structure was less developed than in the NC phase case when we began our investigation. On the theoretical side, Nakanishi and Shiba proposed a stretched honeycomb domain model[8] for the T phase based upon the x-ray diffraction work of Tanda and Sambongi[9,10]. On the experimental side, Thomson et al.[11,12] found evidence for domains in the T phase in an early STM study of the CDW phases of 1T-TaS_2

Thomson et al.[11,12] used the technique of comparing the fine structure of CDW maxima within a suspected domain to show that the phase of the CDW, relative to the atomic lattice, was unaltered across the domain to demonstrate a true phase modulation of the CDW wave vector away from its average (incommensurate) value towards the commensurate value within a domain. However, as explained in chapter 5, the way to determine unequivocally the presence of CDW domains and discommensurations is to examine the FT for satellite spots[13]. Nevertheless, careful scrutiny of the STM images shows that the apparent domains are not entirely consistent with the generally accepted stretched honeycomb model[8-10]. This discrepancy suggests that the surface CDW structure (probed by STM) and the bulk CDW structure (probed by x-ray diffraction) are significantly different in 1T-TaS_2 (and perhaps in other CDW materials as well). To

ascertain whether domains exist in the T phase and, if they do, to determine the geometrical structure of the domains and whether or not they are identical on the surface and in the bulk, we have performed detailed STM and x-ray diffraction studies of the T phase.

6.2 The stretched honeycomb T phase domain model

Here we describe the stretched honeycomb model[8-10] that was widely accepted when we began our investigation. Unlike the NC phase, the CDW in the T phase [present only on warming 1T-TaS_2 from the commensurate phase (T < 180 K)] loses its hexagonal symmetry. This means that the moiré pattern formed from the hexagonal atomic lattice and the CDW lattice is not hexagonal, but rather it is long and narrow. The calculation of the moiré pattern periodicity from the x-ray diffraction derived CDW wave vectors and atomic lattice is the essence of the proposed stretched honeycomb model by Nakanishi, Shiba, Tanda, and Sambongi[8,10]. They used the measured CDW wave vectors to infer the domain period and orientation. In a sense it is more of a conjecture than a model because: (1) there is no Ginzburg-Landau like free energy calculation of the CDW order parameter and its higher order Fourier components which would modulate the CDW into domains (as Nakanishi and Shiba have calculated for the NC phase[1,2]), and (2) the x-ray diffraction study upon which the model is based measures only fundamental and second order CDW wave vectors but makes no attempt to identify satellite structure[10] (As discussed in chapters 4 and 5 satellites must be present if there is true domain structure.)

In Figs. 6.1(a) and 6.1(b) we present a schematic of the stretched honeycomb model of the T phase domain structure. At T = 225 K the domain width is 38 Å, the length is 250 Å, and the long dimension of the stretched honeycomb makes an angle of 1° with the CDW translation vector $\mathbf{T}_2$[10], defined in the section 6.3. This schematic

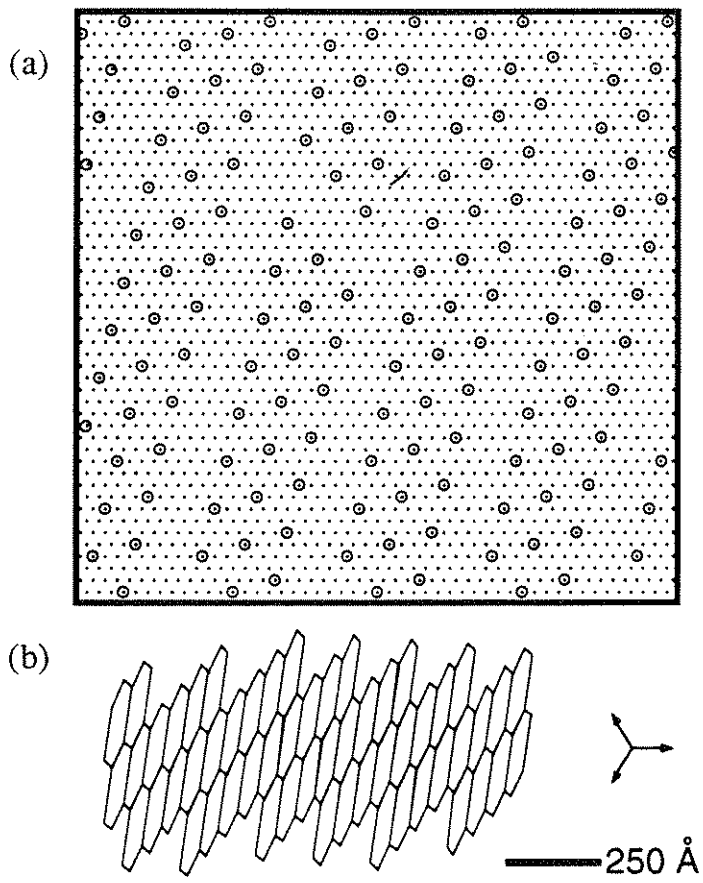

FIG. 6.1 Schematic of stretched honeycomb T phase domain model (a) Small scale structure of model showing registration of CDW maxima relative to the Ta lattice. (b) Large scale structure of model illustrating size and orientation of domains. (Figure provided by Ruth Thomson)

illustrates only a phase modulation of the CDW in which CDW maxima are perfectly aligned with the atomic lattice within a domain and undergo a phase slip of one atomic constant between domains. Because Tanda and Sambongi did not measure satellite structure, not only is the existence of the domain structure in doubt, but also whether the possible domain structure results from a phase modulated only, an amplitude modulated only, or both a phase and amplitude modulated CDW is undetermined.

6.3 STM of 1T-TaS_2 in the T phase

With an STM we imaged the surface of 1T-TaS_2 in the T phase at 225 K [Fig. 6.2(a), obtained in the current mode, with tip bias = -20mV and tunnel current = 5nA]. The smallest visible periodic features in the figure are CDW maxima. Although surface defects obscure any obvious CDW domain structure, close inspection reveals long stripes running diagonally across the image from the upper left to the lower right. We interpret these stripes as CDW domains, where the bright stripes represent regions of enhanced CDW maxima, separated by dark lines of diminished CDW amplitude. From an analysis of six images from three samples we find an average stripe width of 68 ± 5 Å and that the stripe boundary makes an angle of 28° ± 5° with the CDW translation vector direction, $\mathbf{T}_2$ [upper right corner of Fig. 6.2(a)]. Here the CDW translation vectors, $\mathbf{T}_i$, are defined as

$$\mathbf{T}_i = 2\pi \frac{\mathbf{Q}_i \times \mathbf{z}}{|\mathbf{Q}_1 \cdot \mathbf{Q}_2 \times \mathbf{z}|} \tag{6.1}$$

where $\mathbf{z}$ is a unit vector normal to the cleavage plane. The stripes appear to be at least as long as the largest scan (500 Å) we can obtain.

Unambiguous identification of CDW domain structure is possible by analysis of satellite structure in Fourier transformed STM images[13] [Fig. 6.2(b)]. The transform shows three pairs of strong peaks, labeled $\mathbf{Q}_1$, $\mathbf{Q}_2$, and $\mathbf{Q}_3$, which are the CDW

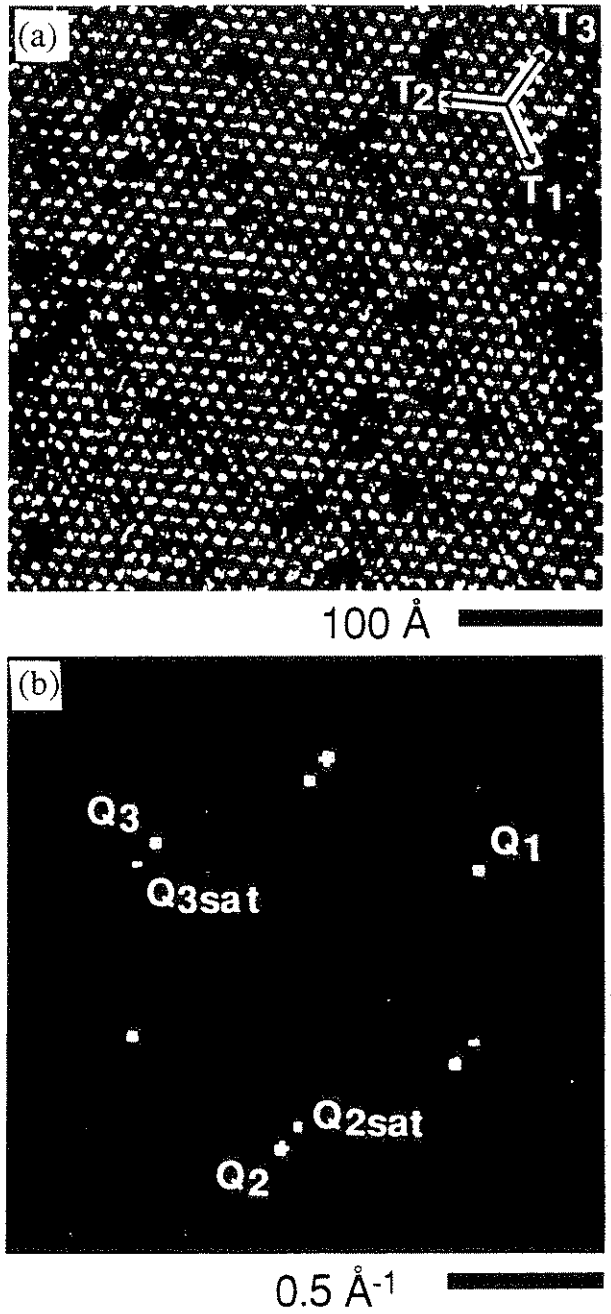

FIG. 6.2 (a) STM image of 1T-TaS_2 at T = 225 K in the T phase. (b) Center of the Fourier transform of (a). CDW peaks are labeled $\mathbf{Q}_1$, $\mathbf{Q}_2$, and $\mathbf{Q}_3$, and satellite peaks are labeled $\mathbf{Q}_{2sat}$ and $\mathbf{Q}_{3sat}$. (Data provided by Ruth Thomson)

XBB 910-8772C

fundamental peaks. Clear satellite peaks, labeled Q_{2sat} and Q_{3sat}, occur near two of the three opposing pairs of CDW peaks. This fine satellite structure demonstrates a true domain modulation of the T phase CDW. Because the satellite distribution around the CDW fundamental peaks is asymmetric, the CDW is both amplitude and phase modulated. The CDW wave vectors may be used to define a lattice and the satellite peak positions may be expressed in terms of the CDW wave vectors. From an analysis of the six Fourier transformed STM data sets, we have determined the average satellite wave vectors and intensities relative to the CDW peak intensities. The uncertainties are ± 0.02 for the Q_1 and Q_2 components of Q_{2sat} and Q_{3sat} (Table 6.1).

6.4 Comparison of Tanda and Sambongi's x-ray data with our STM result

Our finding of a surface striped domain configuration is inconsistent with the previous x-ray diffraction study by Tanda et al. [10] who, for the bulk material, found a stretched honeycomb domain configuration. In order to provide a convenient visual comparison between our STM result and the x-ray diffraction result of Tanda et al., we have constructed a computer generated model of an STM image consistent with their diffraction measurement (Fig. 6.3). The method of construction is similar to that described in chapter 5 used for computer simulations. The gray scale indicates CDW electronic density. The image is formed from a superposition of a set of three sine waves using values of Q_1, Q_2, and Q_3 measured by Tanda and Sambongi[10] to represent the CDW fundamental frequencies with a set of two sine waves using values of Q_{2sat} and Q_{3sat} consistent with, but not uniquely determined by, the measured CDW wave vectors. The amplitude of the two additional sine waves is arbitrarily chosen to be one-fourth that of the CDW sine waves. The additional sine waves would produce satellites near two of the CDW peaks in the FT of the simulated STM image. Although Tanda et al. made no attempt to determine whether satellites exist, they must exist if the stretched honeycomb model correctly describes the true domain structure of the crystal bulk.

Property	Tanda et al. x-ray (225 K) Bulk	Burk et al. STM (225 K) Surface	Burk et al. x-ray (235 K) Bulk
Q_{2sat}	not measured	$0.075Q_1 + 0.908Q_2$	$0.086Q_1 + 0.891Q_2$
Q_{3sat}	not measured	$-1.072Q_1 - 0.908Q_2$	$-1.072Q_1 - 0.891Q_2$
Q_{2sat} rel. intensity	not measured	0.19	0.085
Q_{3sat} rel. intensity	not measured	0.21	0.031
Domain width	38 ± 3 Å	68 ± 5 Å	63 ± 3 Å
Domain length	250 ± 80 Å	> 500 Å	> 600 Å
Domain orientation	1° ± 3°	28° ± 5°	24.5° ± 3.5°
Domain config.	stretched honeycomb	striped	striped

Table 6.1 Comparison of the surface and bulk T phase CDW domain properties as measured by Tanda et al. with x-ray diffraction, Burk et al. with STM, and Burk et al. with x-ray diffraction.

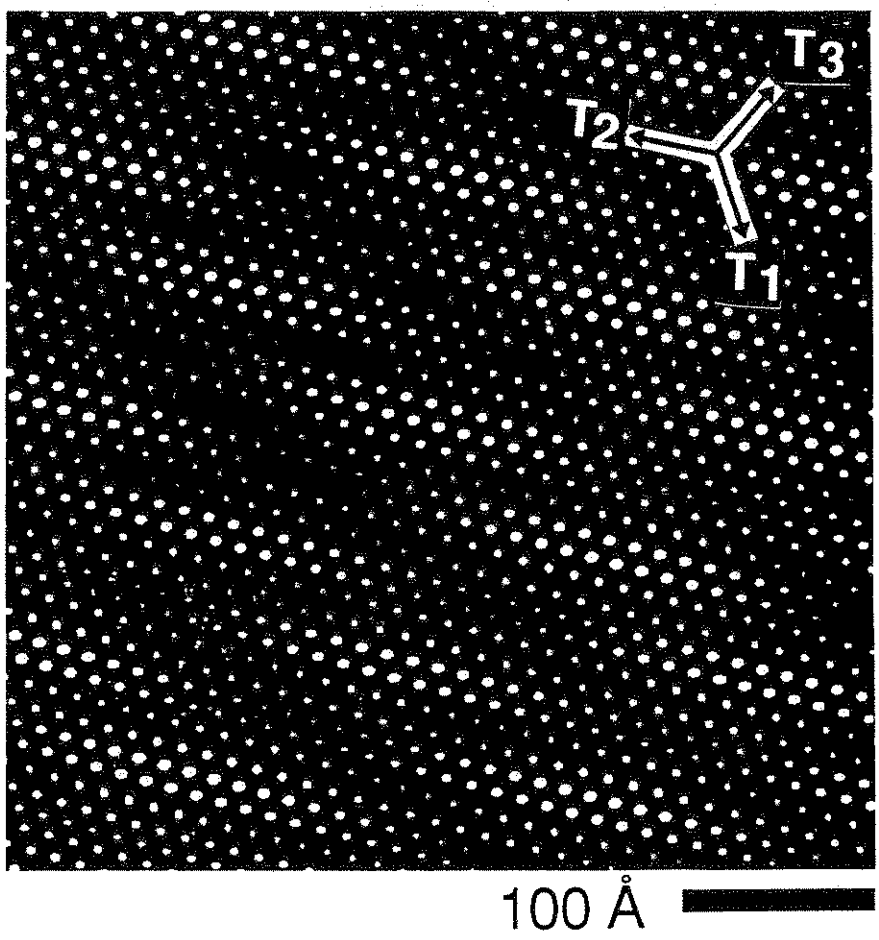

FIG. 6.3 Computer simulation of STM data of a CDW in the stretched honeycomb domain model.

XBB 926-4241

The domain configuration seen in the real STM image in Fig. 6.2(a) and in its highly filtered derivative [Fig. 6.5(b) discussed latter] differs dramatically from the simulated domain configuration constructed in Fig. 6.3. The domain characteristics extracted from the x-ray data of Tanda et al. and from our STM data are summarized in Table 6.1. The discrepancies between the two sets of measurements greatly exceed the quoted experimental uncertainties.

6.5 X-ray diffraction of 1T-TaS_2 in the T phase

In order to establish if this discrepancy reflects an intrinsic difference between the surface and bulk CDW structure in 1T-TaS_2, we have undertaken a careful x-ray diffraction study of the T phase CDW. For our x-ray diffraction experiments we used a four angle diffractometer to measure the CDW wave vectors and to search for fine satellite structure. A 1T-TaS_2 crystal (dimensions $0.2 \times 0.2 \times 0.05$ mm) from a different batch than that used in our STM study was first cooled to the C phase at 150 K and held at that temperature for one hour before warming to the T phase at 235 K . We measured CDW peaks positioned near the Bragg 110 peak [see Fig. 6.4(a)]. The position of the Bragg 110 peak was measured as well to provide a local reference. All peak parameters were determined by a "point and shoot" technique in which x-ray counts were sampled for a fixed time interval on a $9 \times 9 \times 9$ three dimensional grid centered on the approximately known peak positions. A three-dimensional Gaussian peak function was then fitted to the grid of points to extract peak coordinates, widths, and intensities.

In Fig. 6.4 we display our results. Figure 6.4(a) indicates the regions where we measured CDW peaks and satellites. Because of the in-layer hexagonal symmetry of the atomic lattice, there are regions of the crystal in which each of the three CDW wave vectors $\mathbf{Q}_1$, $\mathbf{Q}_2$, and $\mathbf{Q}_3$ makes an angle of 11° - 13° with respect to the $\mathbf{a}^*$ axis. This is the reason we were able to measure all CDW and satellite peaks by examining only the circled regions in Fig. 6.4(a). In Fig. 6.4(b) we show the commensurate CDW wave

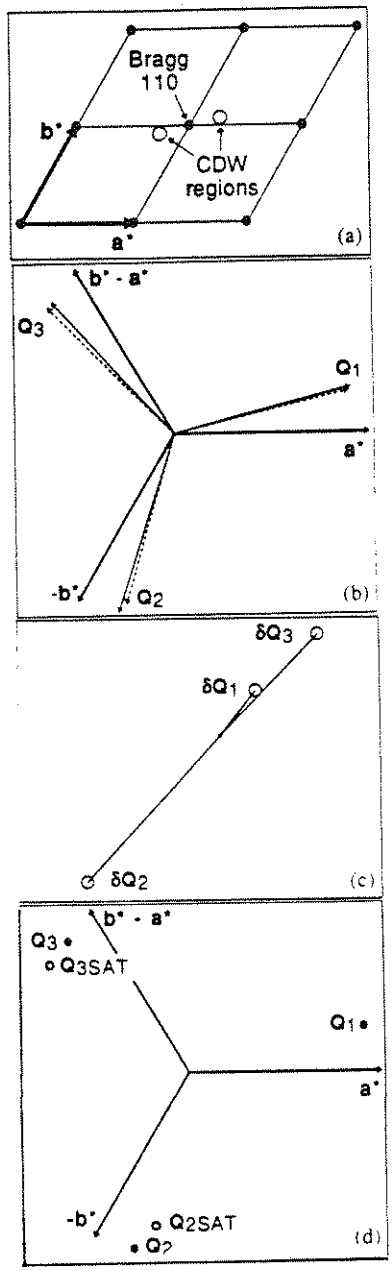

FIG. 6.4 X-ray diffraction of the T phase at T = 235 K. (a) Schematic of the in-layer reciprocal lattice indicating regions probed. (b) Measured CDW wave vectors (dashed arrows) and the commensurate CDW wave vectors (solid arrows). (c) Deviations of measured wave vectors from the commensurate ones. (d) Locations of observed satellites (open circles) relative to the CDW peaks (solid circles).

vectors as solid arrows and the measured CDW wave vectors as dashed arrows. With respect to the commensurate case, $\mathbf{Q}_1$ is rotated clockwise and both $\mathbf{Q}_2$ and $\mathbf{Q}_3$ are rotated counterclockwise. In Fig. 6.4(c) we show the deviations of the T phase wave vectors from the commensurate values, $\delta\mathbf{Q}_i = \mathbf{Q}_{i,\,\text{commensurate}} - \mathbf{Q}_i$. The size of the open circles at the ends of the deviation vectors reflects our uncertainties. To within our experimental uncertainty the deviation vectors are collinear. This is important because it shows that the moiré pattern formed by the CDW lattice and the atomic lattice is striped, not a stretched honeycomb[10].

The measured in-layer CDW wave vectors are shown as solid circles in Fig. 6.4(d). For the T phase CDW wave vectors, following the notation of Tanda and Sambongi[9,10], we find

$$\mathbf{Q}_1 = 0.231\mathbf{a}^* + 0.081\mathbf{b}^* + 0.437\mathbf{c}^* \qquad (6.2a)$$

$$\mathbf{Q}_2 = 0.073\mathbf{a}^* - 0.321\mathbf{b}^* + 0.258\mathbf{c}^* \qquad (6.2b)$$

$$\mathbf{Q}_3 = -0.305\mathbf{a}^* + 0.240\mathbf{b}^* + 0.305\mathbf{c}^* \qquad (6.2c)$$

where the uncertainties are ±0.001 for $\mathbf{a}^*$ and $\mathbf{b}^*$ components and ±0.002 for the $\mathbf{c}^*$ components.

In order to characterize the bulk domain configuration, we searched for fine satellite structure about each of the three CDW peaks. We found one near $\mathbf{Q}_2$ and one near $\mathbf{Q}_3$ [open circles in Fig. 6.4(d)]. Their positions are

$$\mathbf{Q}_{2sat} = 0.085\mathbf{a}^* - 0.279\mathbf{b}^* - 0.074\mathbf{c}^* \qquad (6.3a)$$

$$\mathbf{Q}_{3sat} = -0.313\mathbf{a}^* + 0.199\mathbf{b}^* + 0.627\mathbf{c}^*. \qquad (6.3b)$$

The uncertainties on the **a*** and **b*** components are ±0.002 and on the **c*** components ±0.005. The observation of fine satellite structure by x-ray diffraction demonstrates that a periodic domain modulation of the CDW occurs in the bulk. The satellite wave vectors may be expressed in terms of the CDW wave vectors, as was done for the STM data, so that we can compare the two measurements directly. The results along with the x-ray derived satellite intensities relative to the CDW intensities are included in Table 6.1; the agreement between the two sets of data is very good except for satellite intensities. The direct comparison of the intensities is complicated by x-ray structure factors which we have not attempted to include.

6.6 Comparison of our STM (surface) and x-ray diffraction (bulk) results

The bulk domain configuration extracted from the x-ray CDW and satellite peak positions and intensities is striped, not stretched honeycomb. A real space reconstruction of the in-layer bulk domain configuration is obtained from the measured x-ray data [Fig. 6.5(a)]. The gray scale indicates CDW electronic density. The image is formed from a superposition of a set of three sine waves using measured values of $\mathbf{Q}_1$, $\mathbf{Q}_2$, and $\mathbf{Q}_3$ to represent the CDW fundamental frequencies with a set of two sine waves using measured values of $\mathbf{Q}_{2sat}$ and $\mathbf{Q}_{3sat}$ and their relative intensities to represent the satellite frequencies. The reconstructed stripe width is 60 ± 5 Å, the length is greater than 600 Å, and the orientation of the long dimension of the stripe forms an angle of 24.5° ± 3.5° with the CDW translation vector direction, $\mathbf{T}_2$, indicated in the figure. In an electron diffraction study of the T phase, Withers and Steeds[14] identified "split peaks" (here called the CDW fundamental and satellite peaks), but they misinterpreted them as evidence that the T phase domain is <u>not</u> striped. In fact, the diffraction data of Withers and Steeds are consistent with the reconstruction in Fig. 6.5(a).

The difference between the striped domain structure implied by our data and the

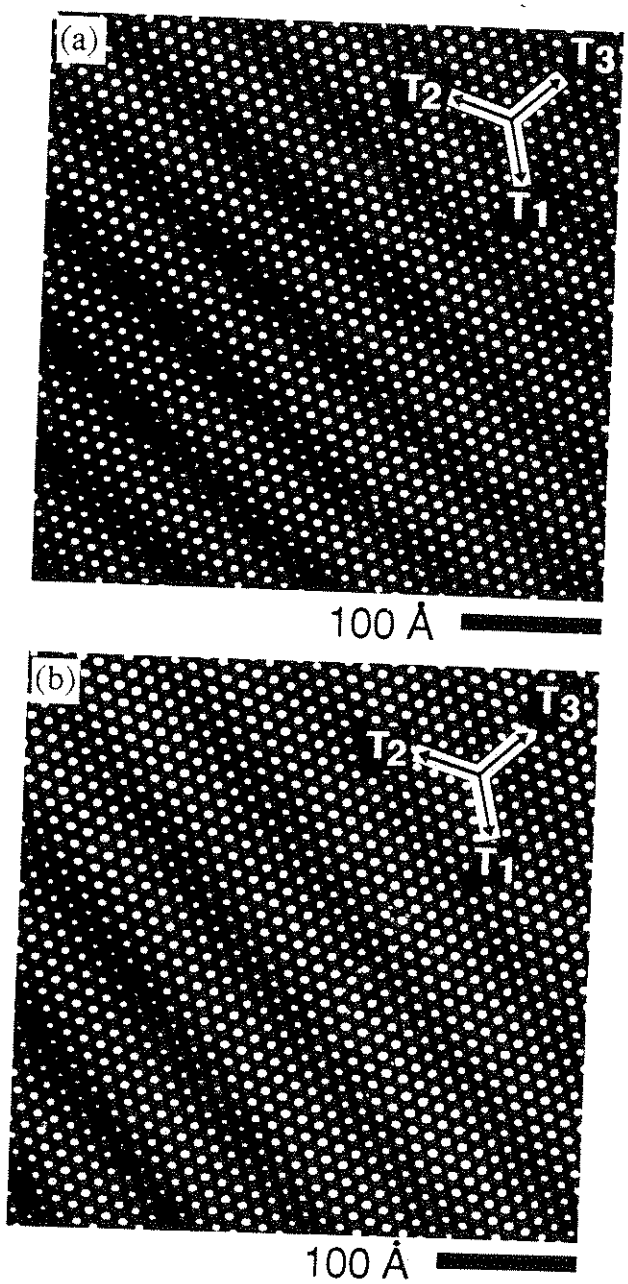

FIG. 6.5 Real space reconstruction of the T phase in-layer CDW domain configuration (a) from the x-ray data and (b) from the measured Fourier components of the STM image [Fig. 6.2(b)]

XBB 910-10000A

stretched honeycomb structure obtained from the x-ray diffraction work of Tanda et al.[9,10] may be traced to a slight disagreement in the measured CDW wave vectors. Our measurements differ from those of Tanda et al. by only a few thousands of a reciprocal lattice vector. The major result of the discrepancy is a rotation of the calculated domain structure by about 27° as well as an increase in the domain width and length. The domain configuration is exceedingly sensitive to the precise values of the CDW wave vectors. However, we can independently test the accuracy of our measured CDW wave vectors by calculating the expected positions of the satellites from the CDW wave vectors alone. If the true domain structure has the same periodicity as the moiré pattern, then potential satellite positions are given by $\mathbf{Q}_i \pm \mathbf{k}_l$ for i, l = 1, 2, 3. Here $\mathbf{k}_l = 3\mathbf{q}_l - \mathbf{q}_m$ for cyclic permutations of l,m,n where $\mathbf{q}_l = \mathbf{Q}_l - \mathbf{Q}_{l,commensurate}$.[1,2,8,13] The calculated and observed positions agree to within our experimental uncertainties.

The bulk domain configuration derived from our x-ray diffraction data is in close agreement with the surface domain configuration observed by STM. A real-space reconstruction of the surface in-layer domain configuration, from the Fourier components measured by STM, is shown in Fig. 6.5(b). This image was generated with the same reconstruction method used for Fig. 6.5(a). This reconstruction is equivalent to filtering the Fourier transform shown in Fig. 6.2(b) at the satellite and CDW peak frequencies and performing an inverse Fourier transformation. With the frequency components due to the defects [Fig. 6.2(a)] filtered out, the striped domain configuration is readily apparent in Fig. 6.5(b). The good agreement between Figs. 6.5(a) and 6.5(b) is striking. As summarized in Table 6.1, the domain configuration parameters of length, width, and orientation that we determined for the surface agree with those that we find for the bulk.

6.7 Interlayer correlation of domains

Because 1T-TaS_2 is both electronically and structurally a quasi-two-dimensional material, it may not seem too surprising that the surface and bulk CDW domain structures

agree. In a material with weak interlayer coupling the absence of coupling from one side for a surface layer should not cause a serious perturbation to the CDW. However, x-ray diffraction studies[10,15] have established a high degree of correlation of the CDW fundamental frequency across layers in the I, NC, and T phases. Therefore, interlayer coupling is significant, yet its absence from one side does not alter the CDW at the surface.

We expect significant interlayer coupling to correlate CDW domains across layers. Because the domain structure arises from the beating of the CDW frequencies with the satellite frequencies, the coherence of the domain structure along the **c** axis is determined by the coherence of both the CDW and satellite frequencies. A lower bound for the coherence of each frequency may be obtained from the peak widths. From our Gaussian fits to the CDW and satellite peaks measured by x-ray diffraction, we obtain full width at half-maximum values, projected onto the **c*** axis, of about 0.035**c*** for both cases. Roughly, this implies that domains are correlated across 20 layers in the T phase of 1T-TaS_2. The domain frequency along the **c** axis is simply the difference, about **c***/3, between the **c*** components of a CDW wave vector and its satellite. Thus the striped domain configuration exhibits a three layer stacking.

6.8 Conclusion

By analyzing the bulk CDW wave vectors and associated satellites by x-ray diffraction, it is found that the bulk contains three-dimensionally ordered striped domains rather than the previously accepted stretched honeycomb domain configuration. The crystal bulk domains are correlated across at least 20 layers in the T phase. The Fourier transforms of STM images yield the same satellite positions as the x-rays. Within experimental error, the surface domain structure observed with STM is identical to that of the bulk, indicating that the CDW striped domain configuration propagates unaltered to the crystal surface.

References

1. K. Nakanishi and H. Shiba, J. Phys. Soc. Jpn. **43**, 1893 (1977).
2. K. Nakanishi, H. Takatera, Y. Yamada, *et al.*, J. Phys. Soc. Jpn. **43**, 1509 (1977).
3. Y. Yamada and H. Takatera, Solid State Commun. **21**, 41 (1977).
4. H. P. Hughes and R. A. Pollack, Commun. Phys. **1**, 61 (1976).
5. T. Ishiguro and H. Sato, Phys. Rev. B **44**, 2046 (1991).
6. M. Kuwabara, M. Tomita, H. Hashimoto, *et al.*, Phys. Status Solidi A **96**, 39 (1986).
7. G. v. Tendeloo, J. v. Landuyt and S. Amelinckx, Phys. Status Solidi A **64**, K105 (1981).
8. K. Nakanishi and H. Shiba, J. Phys. Soc. Jpn. **53**, 1103 (1984).
9. S. Tanda, T. Sambongi, T. Tani, *et al.*, J. Phys. Soc. Jpn. **53**, 476 (1984).
10. S. Tanda and T. Sambongi, Synth. Metals **11**, 85 (1985).
11. R. E. Thomson, U. Walter, E. Ganz, *et al.*, J. Microsc. **152**, 771 (1988).
12. R. E. Thomson, U. Walter, E. Ganz, *et al.*, Phys. Rev. B **38**, 10734 (1988).
13. B. Burk, R. E. Thomson, A. Zettl, *et al.*, Phys. Rev. Lett. **23**, (1991).
14. R. L. Withers and J. W. Steeds, J. Phys. C **20**, 4019 (1987).
15. C. B. Scruby, P. M. Willaims and G. S. Parry, Philos. Mag. **31**, 255 (1975).

Chapter 7

Lattice-induced modulation of a CDW far from commensurability in the I phase of 1T-TaS_2

7.1 Introduction

As explained in chapter 4, the CDW wavelength is determined by the nesting properties of the Fermi surface and is not determined by the lattice periodicity alone. In a CDW system where the CDW is almost commensurate with the underlying atomic lattice, the influence of the CDW-lattice interaction on the CDW has been extensively studied theoretically and experimentally[1-11]. In chapters 5 and 6 we described our work on this issue for the NC and T phases of 1T-TaS_2 where the CDW is close to commensurability. Close to commensurability, first McMillan[1] and then others[2-4] theoretically examined the issue and found that an additional periodic modulation of the CDW into commensurate domains should result. An interesting question is the extent to which the CDW-lattice interaction may induce a modulation of the CDW in a system where the CDW wave vectors are far from commensurability.

The incommensurate (I) CDW phase of 1T-TaS_2 provides an excellent system for studying the CDW-lattice interaction in a CDW that is far from commensurability. Through STM and x-ray diffraction, we have investigated whether the CDW and associated periodic lattice distortion (PLD) is purely sinusoidal, rather than phase and/or amplitude modulated. From STM we find satellites near CDW fundamental peaks suggesting a modulation of the CDW analogous to that seen in the NC and T phases. With x-ray diffraction we find second-order CDW satellite intensity in excess of that which can be explained by a purely sinusoidal PLD. The excess intensity is consistent with a phase and amplitude modulation of the CDW induced by the CDW-lattice interaction.

7.2 STM results for the I phase

In the I phase, present between 543 K and 354 K, the CDW in 1T-TaS_2 is aligned with the lattice, as was shown in chapter 4. An early STM study[8] examined the transition between the I phase and the NC phase and determined that the transition between the two phases occurred at the surface at the same temperature as it took place in the bulk of the sample. This is a further indication that the CDW properties in 1T-TaS_2 are identical in the bulk and on the surface, as we found in chapter 6 for the T phase.

Figure 7.1(a) is an STM image of 1T-TaS_2 in the I phase at 360 K. An interesting property of the CDW in the I phase becomes apparent only on examination of the Fourier transform, shown in Fig. 7.1(b). This FT shows a complicated pattern of peaks which are reminiscent of the satellite peaks present in the FTs when the CDW is in the discommensurate NC and T phases. Interestingly, these "satellites" are in a significantly different orientation from those in the NC and T phases. In the case of the NC and T phases, the satellite peaks do not appear on the line through the fundamental CDW peak and the origin of the FT, which is where the "satellite" peaks occur in the case of the I phase. These extra peaks are suggestive of a modulation of the CDW in this phase as well. However, in the I phase, there is no evidence of such a modulation discernible in the real space data. This is because the intensity of the "satellite" peaks in the FT of this phase is only 1% of the fundamental CDW peak, whereas, for instance, in the T and NC phases the satellite peaks are typically about 20% - 30% of the intensity of the fundamental CDW peak.

Because the observed "satellite" peaks are exactly two CDW wave vectors from the atomic lattice peak towards the origin of the FT, it is difficult to determine whether these peaks are simply second-order harmonics of a uniform CDW or if they indicate a weak but true modulation of the CDW. In order to distinguish between these choices a careful comparison of the CDW fundamental and the "satellite" peak intensities is

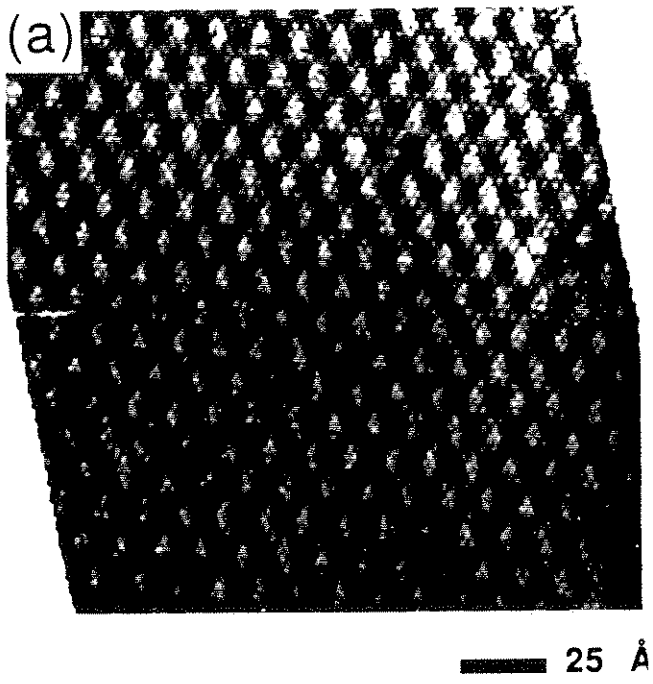

FIG. 7.1 (a) Real space STM image of 1T-TaS_2 in the I phase at 360 K. (b) Fourier transform of (a). Note "satellites" approximately half way between the fundamental CDW peaks and the second-order peaks (located at twice the fundamental peak's distance from the origin).

required. Fourier transforms of STM data are not suitable for the precise determination of intensity ratios of the peaks. In order to resolve this question, we performed a careful x-ray diffraction study to measure the peak intensities.

7.3 X-ray diffraction experimental procedure and results

By x-ray diffraction (Mo kα radiation) we have measured the positions and integrated intensities of the (100) Bragg reflection, one of its first-order CDW satellites, and a second-order CDW satellite referred to the (201) Bragg reflection for a 1T-TaS_2 crystal in the I phase at T = 363 K (Fig. 7.2). The crystal (dimensions $0.4 \times 0.4 \times 0.01$ mm^3) was grown by a standard vapor transport technique[12]. We used a diffractometer with a "point and shoot" technique in which counts were sampled for a fixed time interval at points scanned through each peak parallel to each reciprocal axis. To each line profile a Gaussian function was fitted to extract peak coordinates, widths, and intensities. From the fitted widths and peak intensities of the line profiles, we obtained the integrated intensity[13].

The measured first-order CDW satellite position is consistent with previous x-ray diffraction studies of the I phase[14-16]. For the first-order CDW satellite position we find

$$\mathbf{q}_{cdw1} = 1.282\mathbf{a}^* + 0.002\mathbf{b}^* + 0.333\mathbf{c}^*; \tag{7.1}$$

uncertainties are ± 0.002 for $\mathbf{a}^*$, $\mathbf{b}^*$, and $\mathbf{c}^*$ components.

In order to determine whether the CDW is purely sinusoidal we have investigated a second-order CDW satellite near the first-order satellite. For the second-order CDW satellite position we find

$$\mathbf{q}_{cdw2} = 1.432\mathbf{a}^* + 0.002\mathbf{b}^* + 0.334\mathbf{c}^*; \tag{7.2}$$

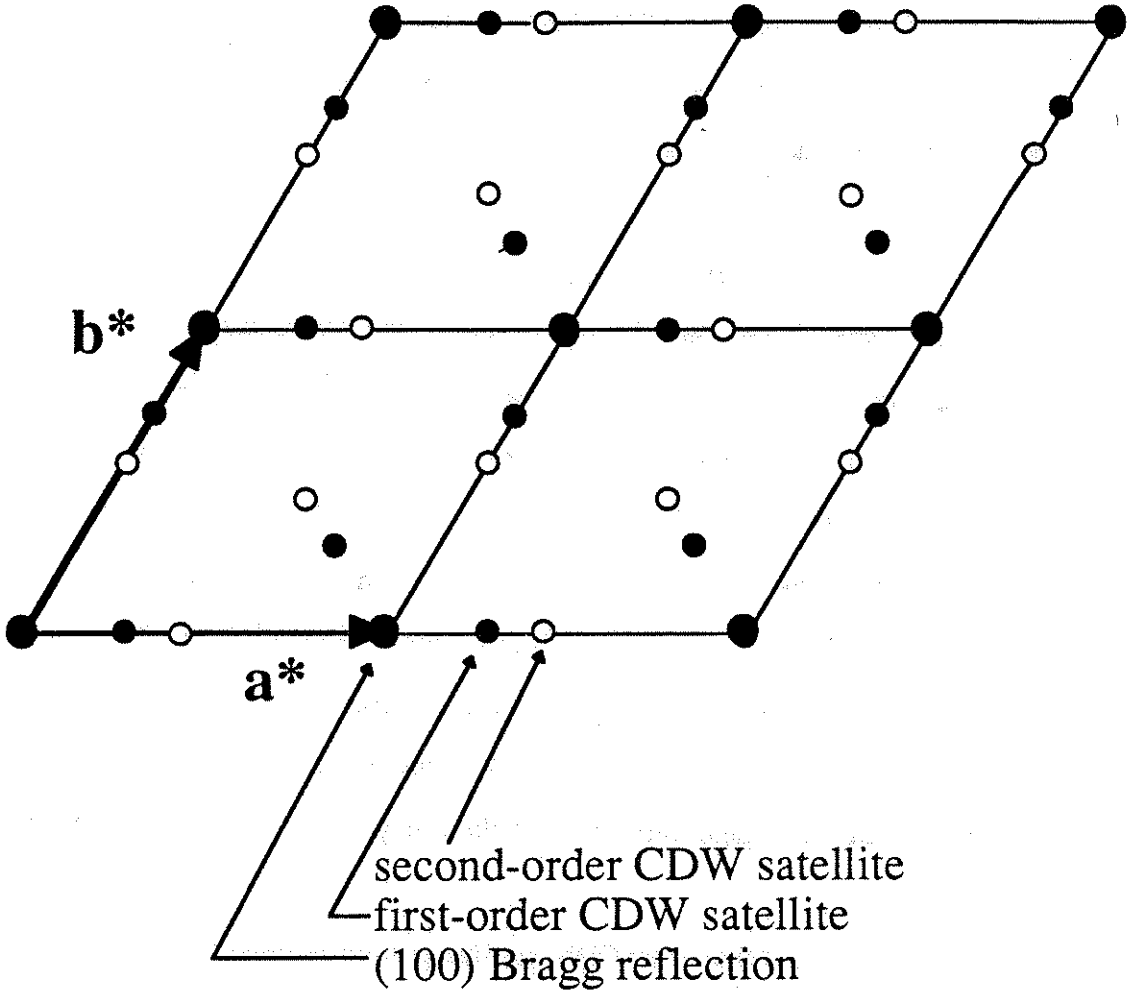

FIG. 7.2 Schematic of the reciprocal lattice projected onto the **a*** - **b*** plane of 1T-TaS_2 in the I phase. Large closed circles indicate Bragg reflections, small closed circles indicate first-order CDW satellites, and small open circles indicate second-order CDW satellites. Only CDW satellites on the (h,k,1/3) plane are shown. Light arrows point to the peaks measured in this study.

On Computer
Brian, Thesis, Chapter 7

uncertainties are ± 0.002 for **a***, **b***, and **c*** components. The observed second-order CDW satellite position is consistent with the measured CDW fundamental wave vectors found in this study. To the best of our knowledge, no intensity at the second-order satellite position in the I phase of 1T-TaS_2 has ever been reported (or perhaps carefully investigated) before this study. The second-order satellite is much weaker than the first-order satellite and so it is more difficult to detect. A line scan profile through the second-order CDW satellite position along the **c*** axis in Fig. 7.3 shows an unmistakable peak.

Throughout this chapter we will state the integrated intensities of CDW satellites relative to the integrated intensity of the (100) Bragg reflection. The experimentally determined first-order CDW satellite integrated intensity $I(q_{cdw1})_{expt} = 3.06 \times 10^{-2}$, and the second-order CDW satellite integrated intensity $I(q_{cdw2})_{expt} = 2.75 \times 10^{-4}$. The uncertainties in intensity are ±10%. The observed satellite intensities are included in Table 7.1 under the "Expt. Intensity" column.

7.4 Comparison of x-ray results with structure factor (with linear phason dispersion)

In order to determine whether these relative intensities are consistent with a purely sinusoidal PLD, one must compare them to the relative intensities calculated from the structure factor. In chapter 4 we briefly described the method of computing the structure factor for a monatomic lattice. There we noted that even a purely sinusoidal PLD should produce some second-order CDW satellite intensity. If the CDW is modulated, then excess intensity should appear in higher order CDW satellites which occur near fundamental CDW peaks. The formula below is developed using the techniques described in chapter 4. For a polyatomic lattice with three equivalent purely sinusoidal CDW's, Chapman and Colella[16] have obtained the following form for the structure factor:

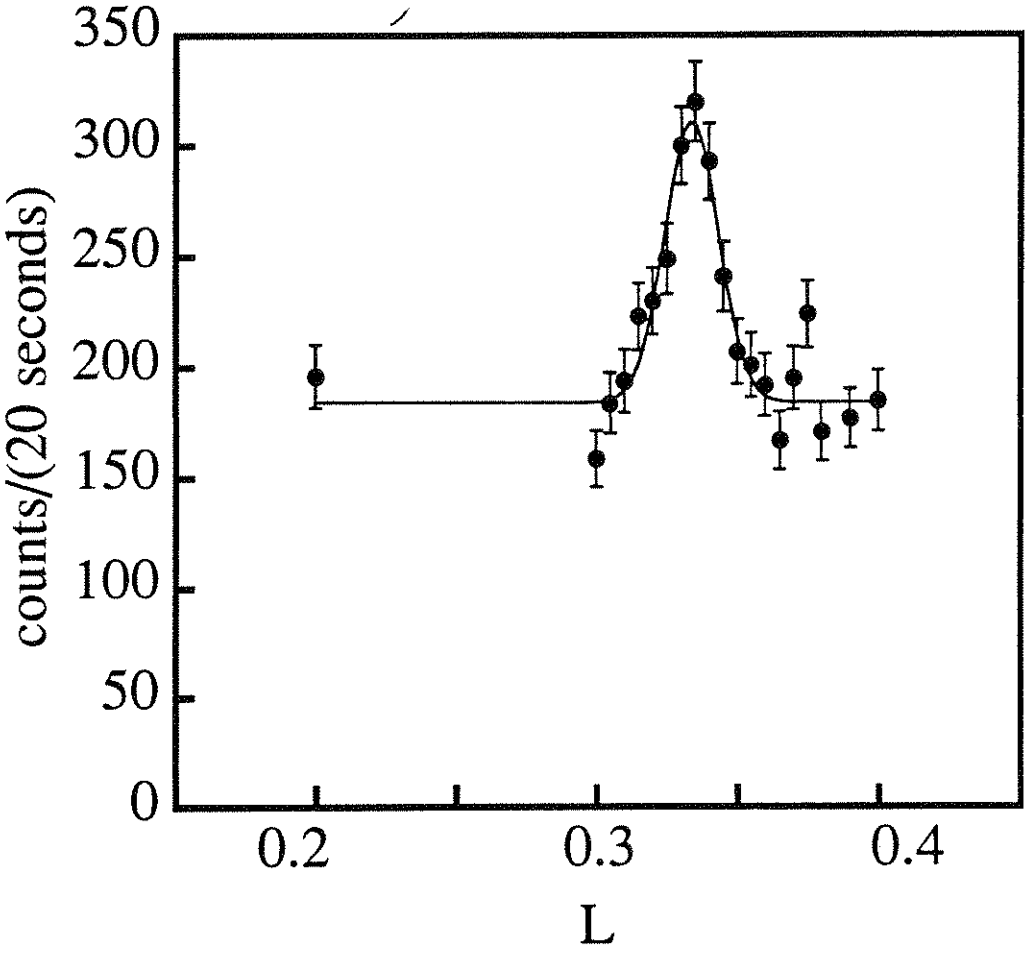

FIG. 7.3 Line scan profile though the second-order CDW satellite parallel to the c* axis obtained from x-ray diffraction at T = 363K in the I phase of 1T-TaS_2.

On Computer

Brian, Thesis, Chapter 7

		Calculated with PTF alone		Calculated with PTF and ATF	
CDW satellite	Expt. Intensity	Calc. Intensity	Ratio of expt. to calc.	Calc. Intensity	Ratio of expt. to calc.
q_{cdw1}	3.06×10^{-2}	2.84×10^{-2}	1.08	2.84×10^{-2}	1.08
q_{cdw2}	2.75×10^{-4}	7.83×10^{-6}	35.1	1.49×10^{-5}	18.4

Table 7.1 Comparison of the integrated intensities of a first and second-order CDW satellite relative to the (100) Bragg peak as measured by x-ray diffraction with the results of our structure factor calculation for 1T-TaS_2 in the I phase.

$$S(\mathbf{q}) = \sum f_i(\mathbf{q})\exp[i(\tau_i \bullet \mathbf{G} + n_1\phi_{i1} + n_2\phi_{i2} + n_3\phi_{i3})]$$
$$\times J_{n1}(\mathbf{q}\bullet\mathbf{A}_{i1})J_{n2}(\mathbf{q}\bullet\mathbf{A}_{i2})J_{n3}(\mathbf{q}\bullet\mathbf{A}_{i3}) \qquad (7.3)$$
$$\times \exp[-C(n_1^2 + n_2^2 + n_3^2)T]$$

where $S(\mathbf{q})$ is the structure factor, $\mathbf{q}$ is the scattering vector for a given CDW satellite with Miller indices n_1, n_2, n_3, $f_i(\mathbf{q})$ is the form factor of the ith atom, τ_i is the basis vector of the ith atom, $\mathbf{G}$ is the reciprocal lattice vector of the CDW satellite's parent Bragg reflection, ϕ_{ij} is the phase of the jth CDW acting on the ith atom, J_{ni} are integer order Bessel functions, and $\mathbf{A}_{ij}$ is the atomic displacement vector of the jth CDW acting on the ith atom. The second exponential factor is the phason temperature factor (PTF)[15]. The PTF is the phason analog of the Debye-Waller factor. It accounts for the diminishment of CDW satellite intensity due to thermally excited CDW phase fluctuations. In the PTF, T is temperature and C is an experimentally determined parameter.

We use Eq. (7.3), along with the values determined by Chapman and Colella[15] for ϕ_{ij}, $\mathbf{A}_{ij}$, and C from their x-ray diffraction study of 1T-TaS_2 in the I phase, to calculate the relative intensities of the first and second-order CDW satellites that we have measured. We obtain atomic form factors and anomalous dispersion corrections from standard tables[17,18]. In Eq. (7.3), for the first-order satellite, $\mathbf{G} = \mathbf{a}^*$, $n_1 = 1$, and $n_2 = n_3 = 0$, and for the second-order satellite, $\mathbf{G} = 2\mathbf{a}^* + \mathbf{c}^*$, $n_1 = -2$, and $n_2 = n_3 = 0$.

The calculated first-order CDW satellite intensity, $I(\mathbf{q}_{cdw1})_{calc} = 2.84 \times 10^{-2}$, and the calculated second-order CDW satellite intensity $I(\mathbf{q}_{cdw2})_{calc} = 7.83 \times 10^{-6}$. In Appendix D we provide a detailed description of the calculation. For the first-order satellite the experimental to calculated intensity ratio $I(\mathbf{q}_{cdw1})_{expt}/I(\mathbf{q}_{cdw1})_{calc} = 1.08$ which is within our stated 10% uncertainty of the expected value of unity for the ratio. Thus for the first-order CDW satellite our results are in excellent agreement with the

results of Chapman and Colella. However, for the second-order satellite the experimental to calculated intensity ratio $I(q_{cdw2})_{expt}/I(q_{cdw2})_{calc} = 35.1$ which is dramatically different from the expected value of unity for the ratio. These results are summarized in Table 7.1 under the "Calculated with PTF alone" column. We observe intensity at the second-order CDW satellite position in excess of that which can be explained by Eq. (7.3) in combination with previously determined parameters ϕ_{ij}, A_{ij}, and C.

The PTF, though experimentally verified by Chapman and Colella between 363 and 423 K, provides an incomplete description of the effect of thermal fluctuations on the intensity of CDW satellite reflections. In addition to thermally excited phasons, thermally excited amplitude fluctuations of the CDW may affect the CDW satellite intensity. Giuliani and Overhauser have proposed a complete CDW thermal fluctuation analysis[19] which includes an ampliton temperature factor (ATF) as well as a PTF. The ATF leads to enhancement of the higher-order CDW peak intensities. The ATF has not been experimentally verified, but its derivation parallels that of the PTF and requires no additional parameters.

In Giuliani and Overhauser's theory the square of the PTF may be written as

$$F_n^{\phi}(T) = \exp[-2n^2 W_{\phi}(T)] \tag{7.4}$$

and the square of the ATF may be written as

$$F_n^{A}(T) = \exp[2|n|(|n| - 1)W_A(T)] \tag{7.5}$$

where n is the order of the CDW satellite. In the high temperature limit ($T >> \theta_{\phi}$ where θ_{ϕ} is the phason analog of the Debye temperature),

$$W_{\phi}(T) = CT \tag{7.6}$$

and

$$W_A(T) = 0.2464CT\,. \tag{7.7}$$

The above expressions for $W_\phi(T)$ and $W_A(T)$ are calculated under the assumption of a linear phason dispersion relation. The parameter, C, in Eq. (7.6) has the same value as the parameter, C, in Eq. (7.3). In this more complete PTF and ATF theory, the second exponential factor in Eq. (7.3) is replaced by $[F_n^{\phi}(T)F_n^{A}(T)]^{1/2}$. For first-order CDW satellites (n = 1), $F_n^{A}(T) = 1$ so that the more complete theory gives the same result as the PTF alone, $I(\mathbf{q}_{cdw1})_{expt}/I(\mathbf{q}_{cdw1})_{calc} = 1.08$. Upon including the ATF for the second-order satellite (n = -2), we find that $I(\mathbf{q}_{cdw2})_{calc} = 1.49 \times 10^{-5}$ and $I(\mathbf{q}_{cdw2})_{expt}/I(\mathbf{q}_{cdw2})_{calc} = 18.4$ (see Appendix D). These results are summarized in Table 7.1 under the "Calculated with PTF and ATF" column. After incorporating the complete PTF and ATF theory to calculate the expected second-order satellite relative intensity, we still find excess intensity.

The excess intensity of the second-order CDW satellite gives evidence that the I phase CDW in 1T-TaS_2 is not purely sinusoidal but rather that the CDW-lattice interaction induces a phase and amplitude modulation of the CDW. As discussed in chapters 5 and 6 we note that the CDW *is* phase and amplitude modulated into periodic domains in the nearly commensurate (NC) and triclinic (T) CDW phases[2,3,5-7,10,11,20,21] where the CDW is close to commensurability. In the NC and T phases the CDW-lattice interaction induces excess intensity in higher-order CDW satellites near first-order satellites. Thus 1T-TaS_2 supports a CDW in which the CDW-lattice interaction is significant. However if the CDW is modulated in the I phase as well, the frequency of the modulation, due to the second-order CDW harmonic, is $\mathbf{q}_{cdw2} - \mathbf{q}_{cdw1} = 0.150\mathbf{a}^* = 0.53(\mathbf{q}_{cdw1} - \mathbf{a}^* - 0.333\mathbf{c}^*)$. This means that the period of the modulation is only about

twice the CDW period and so the modulation is not domain like (in the sense that the modulation period does not contain many CDW wavelengths). We have searched for higher than second-order CDW satellites near the first-order satellite and found none. Since the second-order harmonic is the only harmonic which occurs with significant intensity in the neighborhood of a CDW fundamental, the resulting weak modulation of the CDW should be both phase and amplitude in character with the modulation wave vector parallel to the in-layer component of the CDW fundamental wave vector.

7.5 Alternative interpretation of x-ray results assuming a gapped phason dispersion?

A possible alternative to the periodically modulated CDW to explain the excess second-order satellite intensity arises if one discards the assumption of a linear phason dispersion. The assumption is critical in the calculation of the quantities $W_\phi(T)$ and $W_A(T)$ that enter into the complete PTF and ATF theory. If a gapped phason dispersion is assumed, the PTF and ATF corrections to the calculated CDW peak intensities are altered and, for a suitably chosen gap, the calculated second-order peak intensity might agree with experiment thus allowing a uniformly incommensurate CDW interpretation.

Fortunately $W_\phi(T)$ and $W_A(T)$ can be readily calculated for a gapped phason dispersion. The phason and ampliton dispersion relations are not independent; specifying one determines the other. We have calculated these quantities assuming that

$$\omega_\phi^2 = \omega_o^2 + (v_\phi q)^2 \tag{7.8}$$

where $\omega_\phi(q)$ is the phason frequency at wave vector q, ω_o is the gap in the phason dispersion, and v_ϕ is the large wave vector phason velocity. A gapped phason dispersion results in an ampliton dispersion with relatively lower frequency at small wave vector. Small wave vector amplitons therefore are more readily thermally excited. Amplitons enhance the intensity of second and higher-order CDW peaks [Eq. (7.5)]. Similarly,

phasons are less easily thermally excited, due to the gap, and so the relative intensity of all CDW peaks is enhanced [from Eq. (7.4) phasons diminish all CDW peaks].

Using Eq. (7.8) and the ampliton dispersion relation it implies, we recalculate $W_\phi(T)$ and $W_A(T)$ within Giuliani and Overhauser's theory. Then we compare our newly calculated PTF and ATF with the experimentally determined CDW peak intensities. We present the detailed calculation in Appendix E. We find that there is no physically plausible value of the parameter ω_0 that fits the data under the assumption of a uniformly incommensurate CDW with no *static* phase or amplitude modulation of the CDW. We have calculated $W_\phi(T)$ and $W_A(T)$ for other phason dispersion relations and they fail to fit our data.

7.6 Conclusion

In conclusion, we have measured the intensities of the CDW first and second-order satellites in the I phase of 1T-TaS_2. We have shown that our measurements are inconsistent with the results of a structure factor calculation incorporating a purely sinusoidal PLD, the PTF, the ATF, and a linear phason dispersion. We propose that the observed excess intensity of the second-order CDW satellite is due to a periodic phase and amplitude modulation of the CDW. It should be recognized that this conclusion is based upon the PTF and ATF. If the assumption of a linear phason dispersion relation for the I phase of 1T-TaS_2 is invalid, the PTF and ATF must be modified but our conclusion is not altered. The excess intensity can not all result from enhanced ampliton and diminished phason dynamic fluctuations that a gapped phason dispersion relation would afford. Diffuse x-ray scattering surrounding satellite reflections in 1T-TaS_2 by Minor et al.[22] shows no evidence of a $q = 0$ gap in the phason dispersion relation, although they do not state the upper bound on a gap that their result implies. If the Minor et al. result is rigorously correct, then all the excess intensity we observe results from a phase and amplitude modulation of the CDW.

Refernees

1. W. L. McMillan, Phys. Rev. B **14**, 1496 (1976).
2. K. Nakanishi and H. Shiba, J. Phys. Soc. Jpn. **43**, 1893 (1977).
3. K. Nakanishi, H. Takatera, Y. Yamada, *et al.*, J. Phys. Soc. Jpn. **43**, 1509 (1977).
4. K. Nakanishi and H. Shiba, J. Phys. Soc. Jpn. **53**, 1103 (1984).
5. S. Tanda, T. Sambongi, T. Tani, *et al.*, J. Phys. Soc. Jpn. **53**, 476 (1984).
6. S. Tanda and T. Sambongi, Synth. Metals **11**, 85 (1985).
7. B. Burk, R. E. Thomson, A. Zettl, *et al.*, Phys. Rev. Lett. **23**, (1991).
8. R. E. Thomson, U. Walter, E. Ganz, *et al.*, Phys. Rev. B **38**, 10734 (1988).
9. B. Giambattista, C. G. Slough, W. W. McNairy, *et al.*, Phys. Rev. B **41**, 10082 (1990).
10. X. L. Wu and C. M. Lieber, Science **243**, 1703 (1989).
11. X. L. Wu and C. M. Lieber, Phys. Rev. Lett. **64**, 1150 (1990).
12. F. J. Di Salvo, J. A. Wilson, B. G. Bagley, *et al.*, Phys. Rev. B **12**, 2220 (1975).
13. To precisely determine the integrated intensity a more complicated fully three-dimensional sampling of a peak is required. However the simple line scan technique should provide integrated intensities accurate to within 10%. None of the analysis presented in this paper requires experimental accuracy in integrated intensity exceeding 10%.
14. C. B. Scruby, P. M. Willaims and G. S. Parry, Philos. Mag. **31**, 255 (1975).
15. L. D. Chapman and R. Collela, Phys. Rev. Lett. **52**, 652 (1984).
16. L. D. Chapman and R. Colella, Phys. Rev. B **32**, 2233 (1985).
17. D. T. Crommer and J. B. Mann, Acta Cryst. **A24**, 321 (1968).
18. D. T. Crommer and D. Liberman, J. Chem. Phys. **53**, 1891 (1970).
19. G. F. Giuliani and A. W. Overhauser, Phys. Rev. B **23**, 3737 (1981).
20. B. Burk, R. E. Thomson, J. Clarke, *et al.*, Science **257**, 362 (1992).

21. R. V. Coleman, W. W. McNairy and C. G. Slough, Phys. Rev. B **45**, 1428 (1992).

22. W. Minor, L. D. Chapman, S. N. Ehrlich, *et al.*, Phys. Rev. B **39**, 1360 (1989).

Chapter 8

The rubidium isotope effect in Rb_3C_{60}

8.1 Introduction

The detailed mechanism of superconductivity in alkali-intercalated C_{60} remains controversial, with proposals for both electronic[1,2] and phonon-mediated[3-8] mechanisms. The phonon mechanisms can be further subdivided into models that rely exclusively upon on-ball molecular phonons[3-5] and those which incorporate additional modes such as librons[8], translational modes[9] or alkali-C_{60} optic phonons[6,7]. For any superconducting mechanism, we can write $T_c \propto M_i^{-\alpha_i}$ where M_i is the mass of a given atomic constituent and α_i is the isotope shift exponent for the i th atomic species. Although these models generally predict a carbon isotope effect, a substantial intercalant isotope effect is expected only for models with a significant alkali-C_{60} optic phonon contribution to the pairing mechanism. An accurate measurement of the alkali atom isotope effect would therefore provide a useful constraint on the mechanism of superconductivity.

Earlier isotope effect measurements on A_3C_{60} (A = K, Rb) consist of a single rubidium experiment[10] and several carbon isotope effect experiments[11-15]. There is uncertainty concerning the intrinsic carbon isotope effect in that a more homogeneous carbon isotopic distribution seems to yield a smaller carbon isotope effect[16]. The most complete substitution to date yields $\alpha_C = 0.3 \pm 0.05$ for K_3C_{60} and Rb_3C_{60}[16]. Susceptibility measurements on powder samples of T_c yield an upper limit on the rubidium isotope effect exponent of $\alpha_{Rb} < 0.2$[10]. Ebbesen et al.[10] argue that their result demonstrates rubidium-C_{60} optic phonons do not play a significant role in C_{60} superconductors. This claim is refuted in Appendix F following a simple derivation of an analytic expression for α_{Rb}.

Comparison of the T_c's of K_3C_{60} and Rb_3C_{60} *at equal lattice constant* does not constitute a valid alkali isotope experiment. Since $T_c^{Rb_3C_{60}} > T_c^{K_3C_{60}}$ at equal lattice

constant[17], such an approximation would suggest an inverse isotope effect of rough magnitude $\alpha_{alkali} \approx -0.2 \pm 0.2$. However, this result is clouded by the large difference in ionic radii between K^+ and Rb^+, which could yield a change in vibrational dynamics of the same magnitude as that cause by the change in alkali mass. Considering the present experimental situation, a greater certainty in α_{Rb} is desirable in order to narrow the constraints on plausible pairing mechanisms. We report detailed measurements of the effect of rubidium isotope substitution on the resistive T_c in C_{60} single crystals intercalated with ^{85}Rb, ^{87}Rb, and natural abundance rubidium, ^{na}Rb.

8.2 Experimental procedure

First we describe the intercalation vessel. The considerations that went into the design were that it should be air tight and clean, provide a good thermal link between the sample and temperature sensor, and be able to withstand extended exposure to temperatures up to 300 °C. The vessel consists of a Pyrex to stainless steel tube union, sealed at the Pyrex end, and a Swagelok compression fitting cap modified with a specially designed sample stage that seals the stainless steel end of the tube. A schematic of the vessel is shown in Fig. 8.1. The rubidium metal is placed in the Pyrex end of the tube and the unintercalated C_{60} crystal is placed on the end of the sample stage. The Pyrex segment of the tube has a neck at the midpoint to prevent the rubidium from inadvertently falling onto the crystal. The sample stage is supported by a stainless steel tube that is hard soldered to the cap. The temperature sensor is inserted into the stainless steel tube and screwed into the threaded sample stage. The electrical leads to the sample are 5 mil manganin wire with Kapton insulation.

Since isotopically pure elemental rubidium is not commercially available, we produced all rubidium used in this experiment by extraction of Rb metal from RbCl. We extract Rb metal from isotopically enriched RbCl (RbCl @ 99.2% ^{87}Rb, 0.8% ^{85}Rb and RbCl @99.8% ^{85}Rb, 0.2% ^{87}Rb from US Services) and from natural abundance RbCl

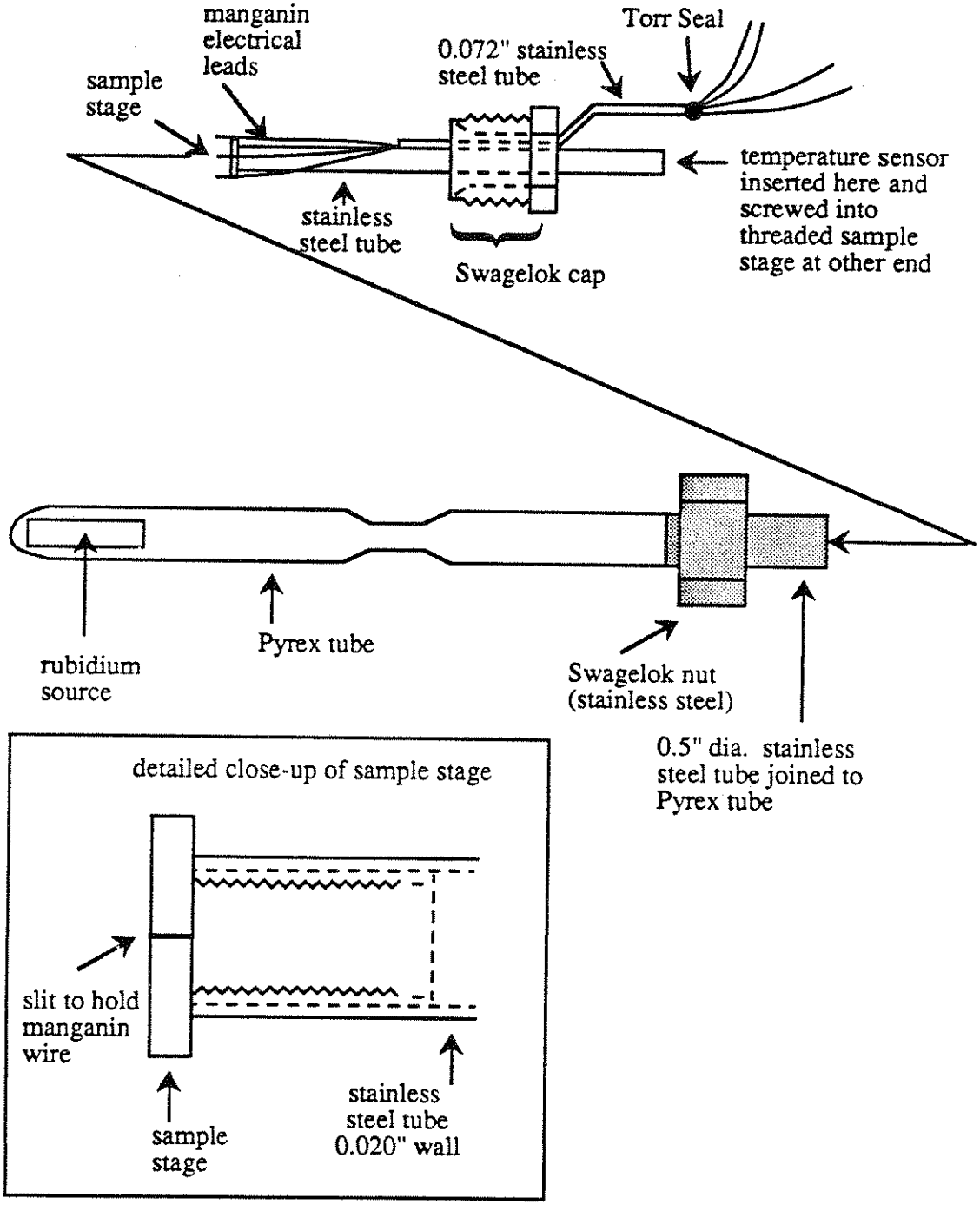

FIG. 8.1 Schematic of the intercalation vessel.

On Computer

Brian, Thesis, Chapter 8

(RbCl @ 72.2% ^{85}Rb, 27.8 ^{87}Rb from Aldrich). We place 177 mg RbCl and approximately 500 mg finely divided calcium into a Pyrex tube that is continuously evacuated by a mechanical pump. The RbCl and calcium mixture at one end of the tube is heated with a flame until the mixture reacts (near the melting point of RbCl, ≈ 718 °C). The reaction produces rubidium vapor and $CaCl_2$. The rubidium vapor rapidly condenses on the cool portion of the tube wall away from the reacting mixture. After reaction completion, the open end of the tube is sealed with a flame and the tube segment with condensed rubidium metal is separated in a glove box and introduced into the intercalation vessel.

The procedure outlined here differs from that described by Ebbesen et al.[10] They reacted lithium with RbCl to liberate rubidium. Initially we used an independently developed lithium reaction method but found separation of rubidium from residual lithium to be difficult. With the calcium reaction, separation is trivial since the calcium vapor pressure is three to four orders of magnitude lower than the rubidium vapor pressure over a wide temperature range. Heating the reaction products with a flame drives the rubidium vapor away from the remaining calcium.

We intercalate single-crystal C_{60} samples (typically 1 mm × 1 mm × 0.1 mm) with rubidium vapor following the technique developed by Xiang et al.[18] C_{60} crystals with electrical contacts are maintained at 250 °C and exposed to rubidium vapor in the intercalation vessel. Vapor exposure is maintained as long as resistance continues to decrease. The samples are annealed at 250 °C without rubidium vapor until the resistance stabilizes. Annealing duration is typically 12 to 24 hours. We repeat the process until no further decrease in resistance is achieved. Usually 10 to 20 cycles are required to achieve complete uniform intercalation. While samples with apparently intrinsic resistance versus temperature behavior may be produced with shorter annealing times and fewer intercalation and anneal cycles, they tend to exhibit broader superconducting transitions.

8.3 Definition of T_c and results

In Fig. 8.2 we show resistance versus temperature data of ^{85}Rb, ^{87}Rb, and ^{na}Rb-intercalated samples near T_c, normalized to the resistance at T = 32 K. The resistive transitions are sharp (for this material), indicating a high degree of homogeneity within a given sample. We define T_c by the maximum in the derivative of the resistance with respect to temperature. Figure 8.3 shows dR/dT for each sample. The data are fitted with a cubic spline, and the maximum of the fit determines T_c (parabolic and gaussian fits yield essentially equivalent results). We measured the resistive transition several times, T_c being reproducible to within 5 mK for a given sample. We define the width of the transition as the separation between the maximum and minimum in the second derivative, yielding transition widths from 140 to 180 mK. We assign an uncertainty to T_c of 0.1 times the transition width. This uncertainty estimate is always greater than the reproducibility spread of T_c for a given sample; it reflects our estimate of the errors introduced by inhomogeneous broadening of the transition.

Before presenting the isotopically shifted results, we note that our measurements provide the most accurate determination for T_c in Rb_3C_{60}. For $^{na}Rb_3C_{60}$ we find T_c = 30.82 ± 0.09 K, where the uncertainty reflects possible temperature calibration errors. This result is 1-2 K higher than reported susceptibility measurements of T_c[11,19] and about 0.6 K higher than previous resistive T_c's[20]. We have verified that temperature gradients between the sample and the temperature sensor (Lakeshore CGR2000) are small. We have measured resistance curves for a sample vessel immersed in a sealed container with liquid neon in which the neon vapor pressure and the temperature sensor provide simultaneous temperature measurements. The temperature sensor calibration agrees with the neon vapor pressure-derived temperature to within 90 mK. Furthermore, the measured T_c (as determined by the temperature sensor) is independent of whether or not the sample vessel is immersed in liquid neon, indicating that the temperature lag

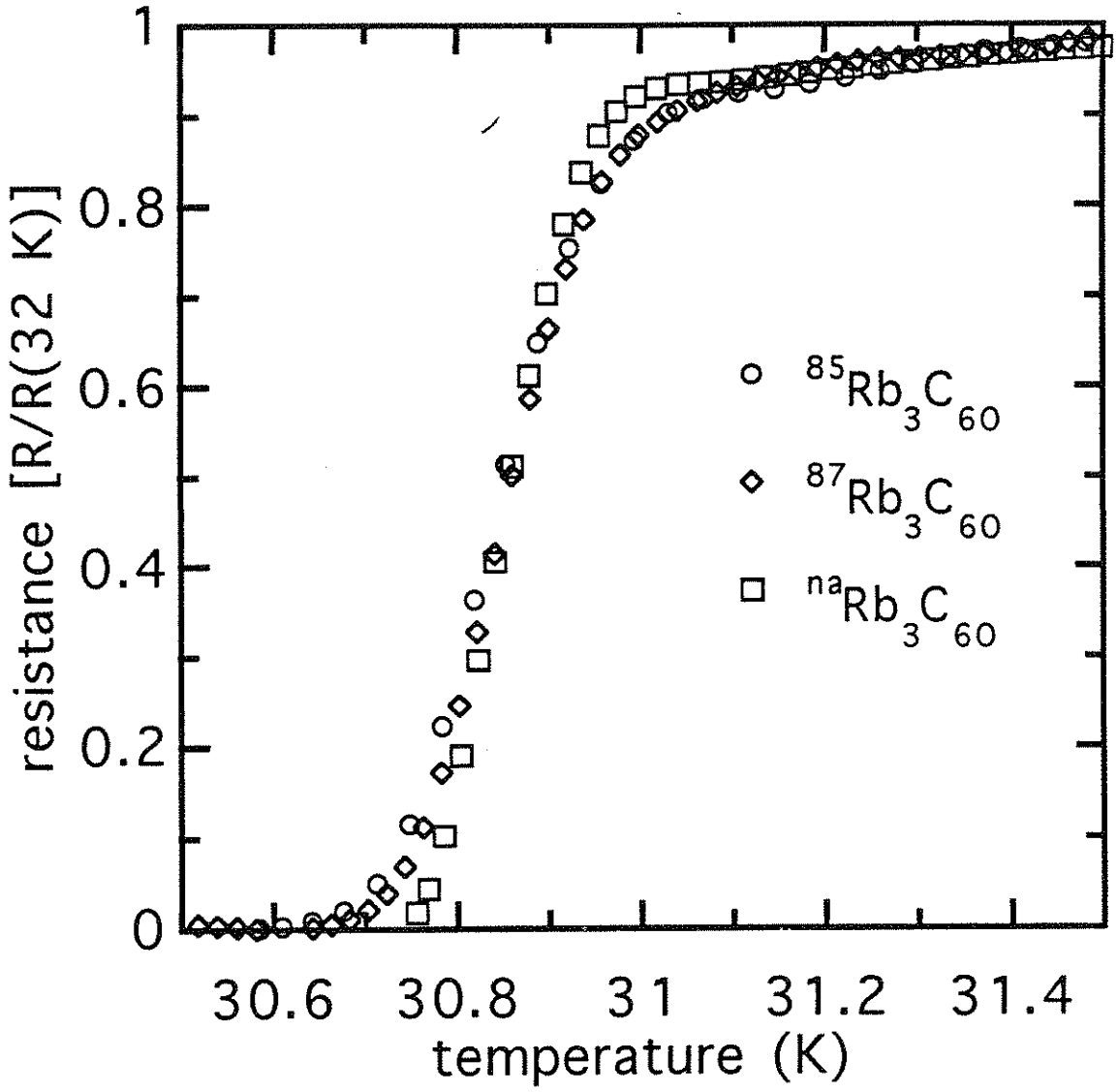

FIG. 8.2 Normalized resistance versus temperature near T_c for $^{85}Rb_3C_{60}$, $^{87}Rb_3C_{60}$, and $^{na}Rb_3C_{60}$.

On Computer Brian, Thesis, Chapter 8

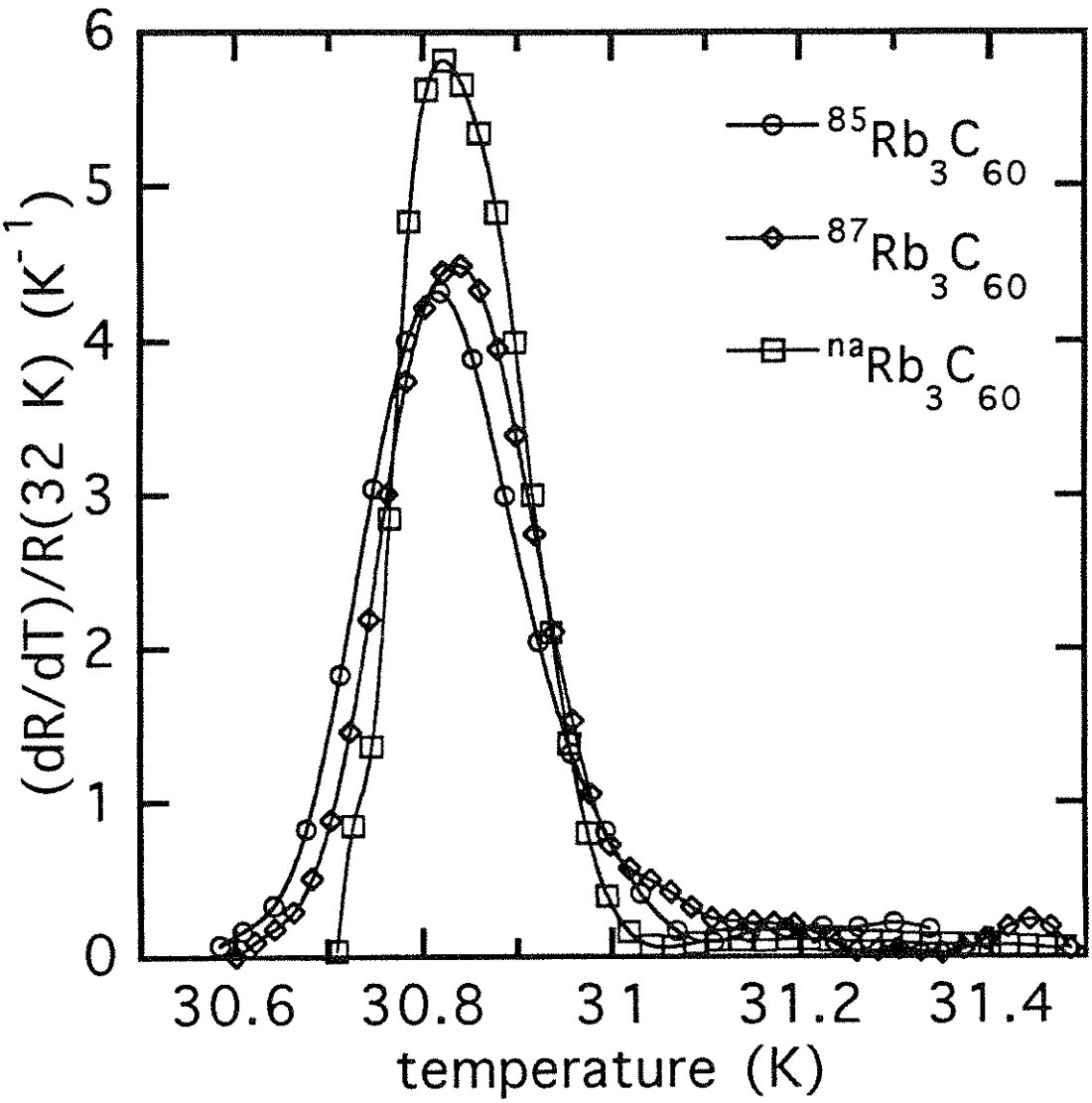

FIG. 8.3 Derivative with respect to temperature of normalized resistance near T_c for $^{85}Rb_3C_{60}$, $^{87}Rb_3C_{60}$, and $^{na}Rb_3C_{60}$. Curves are cubic spline fits to the data. Position of curve fit maximum determines T_c.

On Computer

Brian, Thesis, Chapter 8

between sample and sensor is negligible in the normal measurement configuration without neon.

Figure 8.4 displays our results for T_c measured in $^{85}Rb_3C_{60}$, $^{87}Rb_3C_{60}$, and $^{na}Rb_3C_{60}$. The data are plotted as T_c versus average rubidium mass. For comparison we plot the result for the BCS maximum value of $\alpha_i = 0.5$ normalized to the $^{87}Rb_3C_{60}$ data point. We obtain α_{Rb} = -0.028 ± 0.036, or equivalently ΔT_c = -20 ± 26 mK for $^{87}Rb_3C_{60} \rightarrow {}^{85}Rb_3C_{60}$ (the error bars indicate the 65% confidence interval). To within our experimental uncertainty there is no rubidium isotope effect on T_c in Rb_3C_{60}.

8.4 Analysis with implications for mechanisms

Before discussing the implications of this result for the different pairing mechanisms, we consider an indirect rubidium isotope effect due to a weak dependence of lattice constant on Rb mass. Both electronic[2] and phonon-mediated mechanisms are expected to exhibit an effect of lattice constant on transition temperature. To estimate this effect, we use the experimentally determined lattice constant dependence of T_c, 44 KÅ^{-1}[17,19]. The isotopic shift in lattice constant can be estimated from the fractional change in crystal isotopic mass $\Delta M/M$, the bulk modulus B, the phonon mode energies E_i and Grüneisen constants γ_i[21],

$$\frac{\Delta a}{a} = -\frac{2}{3}\frac{\Delta M}{M}\frac{1}{Ba^3}\sum_i \gamma_i E_i \quad . \tag{8.1}$$

We treat the C_{60} molecule as a single entity, yielding four "atoms" per unit cell. The relevant phonon frequencies are the intermolecular translational and Rb-C_{60} optic modes, with frequencies in the range 50-300 K. An upper limit on the Grüneisen constants can be estimated from the pressure dependence of the bulk modulus[17], which provides information about the hardening of the intermolecular modes with pressure. These estimates yield $\Delta a \approx 0.5 - 2.0 \times 10^{-4}$ Å for $^{87}Rb_3C_{60} \rightarrow {}^{85}Rb_3C_{60}$, which

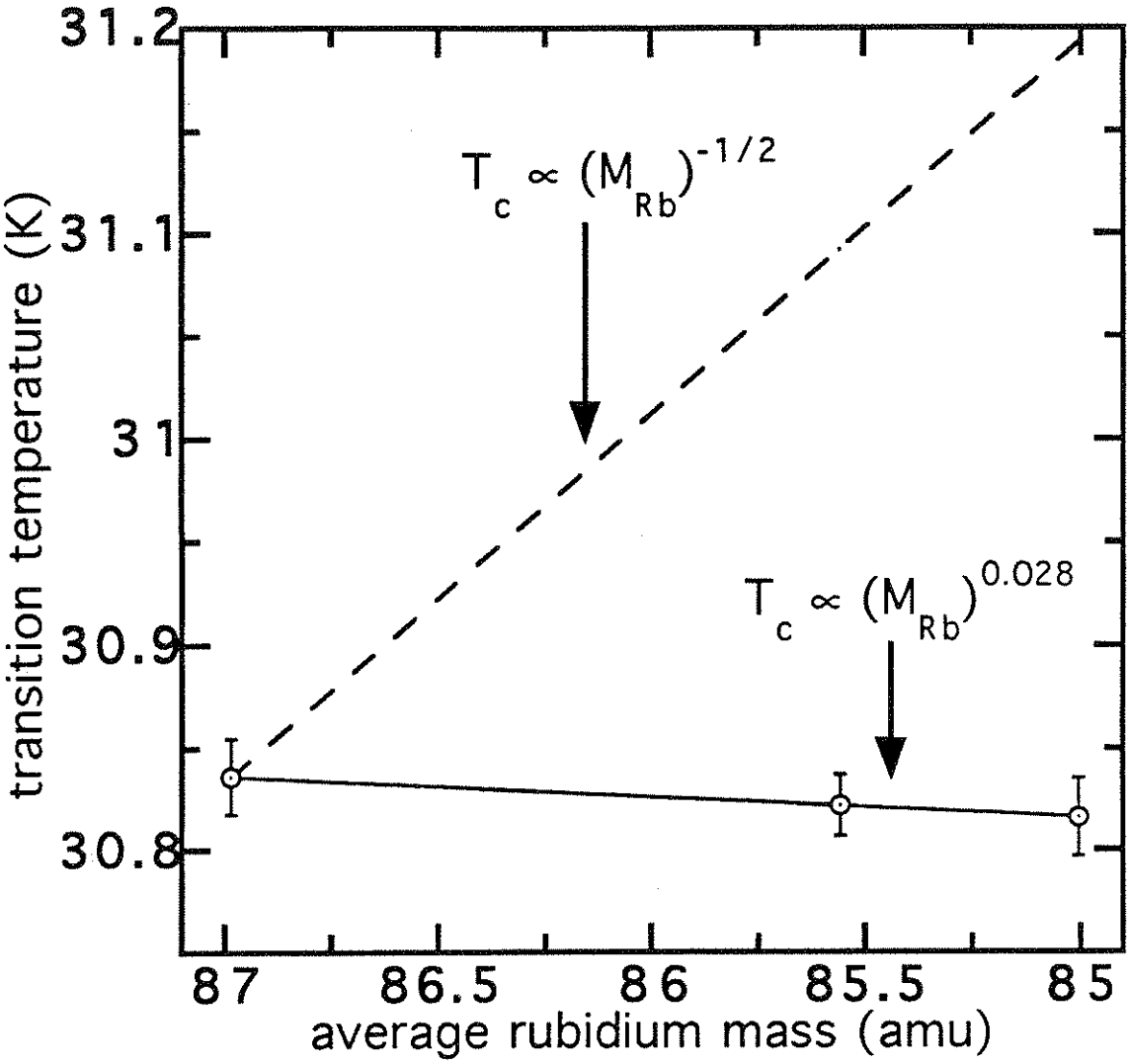

FIG. 8.4 Plot of T_c versus average rubidium mass in Rb_3C_{60}. Solid line is fit of the data to $T_c \propto M_{Rb}^{0.028}$. Dashed line shows $T_c \propto M_{Rb}^{-0.5}$ with proportionality constant chosen so that the line passes through the $^{87}Rb_3C_{60}$ data point.

On computer

Brian, Thesis, Chapter 8

translates into an increase in T_c of 2-9 mK. The entire range of this estimate falls within two standard deviations of the experimental result for α_{Rb}, indicating that the null experimental result is robust under consideration of isotopic shifts in lattice constant.

In addition to increasing the lattice constant, the substitution of ^{85}Rb for ^{87}Rb could harden the librational potential, reducing a possible librational contribution to the electron-phonon coupling. Such an effect can be estimated from the dependence of the librational mode frequency upon the size of the alkali atom[22]. The substitution of Rb for K increases the librational frequency by 8 K. The steric effects of this substitution also increase the lattice constant by 0.15 Å. The $^{87}Rb \rightarrow {}^{85}Rb$ substitution increases the lattice constant by $0.5 - 2.0 \times 10^{-4}$ Å, implying a tiny increase in librational mode frequency on the order of 10^{-2} K, which is a negligible effect.

A model of superconductivity in Rb_3C_{60} incorporating both on-ball carbon phonons and Rb-C_{60} optic modes would predict a direct rubidium isotope effect due to isotopic shift in phonon frequency. The present experiment places limits on the relative contributions of rubidium modes within such a model. First we obtain a simple analytic constraint on the relative contribution of rubidium modes to the electron-phonon coupling. We assume that T_c depends on atomic mass only through the mass dependence of the average phonon frequency,

$$\alpha_i = \frac{1}{2} \frac{d \ln T_c}{d \ln \omega_{log}} \frac{d \ln \omega_{log}^{-2}}{d \ln M_i} , \tag{8.2}$$

where ω_{log} is defined by

$$\omega_{log} = \exp\left(\sum_n \frac{\lambda_n}{\lambda} \ln \omega_n \right) , \tag{8.3}$$

with λ_n the electron-phonon coupling constant to the mode with frequency ω_n and λ is the total coupling constant. The logarithmic frequency average is the most accurate single- frequency approximation for the full spectrum of electron-phonon coupling. Using the McMillan formula for T_c[23] with a spectrum of pure carbon and Rb-C_{60} optic modes we obtain

$$\frac{\alpha_{Rb}}{\alpha_C + \alpha_{Rb}} \frac{3M_{Rb}}{M_{eff}} = \frac{\lambda_{Rb}}{\lambda} \qquad \text{and} \qquad M_{eff} = \frac{3M_{C_{60}}M_{Rb}}{M_{C_{60}} + 3M_{Rb}} \tag{8.4}$$

where M_{eff} is an estimate of the effective optic mode mass. The complete derivation of Eq. (8.4) is given in Appendix F. An upper bound on α_{Rb} yields an upper bound on the fractional contribution of λ_{Rb} to λ. Using the minimal reported value for α_C (α_C =0.3) and two standard deviations above the measured α_{Rb} as an upper bound on α_{Rb} (α_{Rb} < 0.044), this simple analytic model yields $\lambda_{Rb}/\lambda < 0.17$. Adjusting for a possible lattice-constant induced isotope shift of 2-9 mK would decrease this bound by roughly 10%.

In order to examine the effects of the detailed frequency distribution of the electron-phonon coupling we performed numerical solutions of the Eliashberg equations for various electron-phonon coupling spectra. The on-ball carbon phonons were modeled following the results of three theoretical calculations[3-5]. The frequency of the Rb-C_{60} optic modes was varied from 50 to 300 K. Neutron scattering results suggest mode frequencies on the order of 200 K[24], while theoretical treatments[6,25] place these modes in the range from 50 to 200 K. For each electron-phonon coupling spectrum the values of λ, μ, and λ_{Rb} were varied to match experimental constraints of α_C = 0.3, T_c = 30.8, and $\alpha_{Rb} < 0.044$. The results are presented in Fig. 8.5. The three models yield different values of λ and μ^* while the limits on λ_{Rb}/λ remain essentially unchanged. As the frequency of the alkali modes increases from 50 to 300 K, the limit on λ_{Rb}/λ decreases from 0.33 to 0.08 for all three spectra. Although the contribution of the alkali

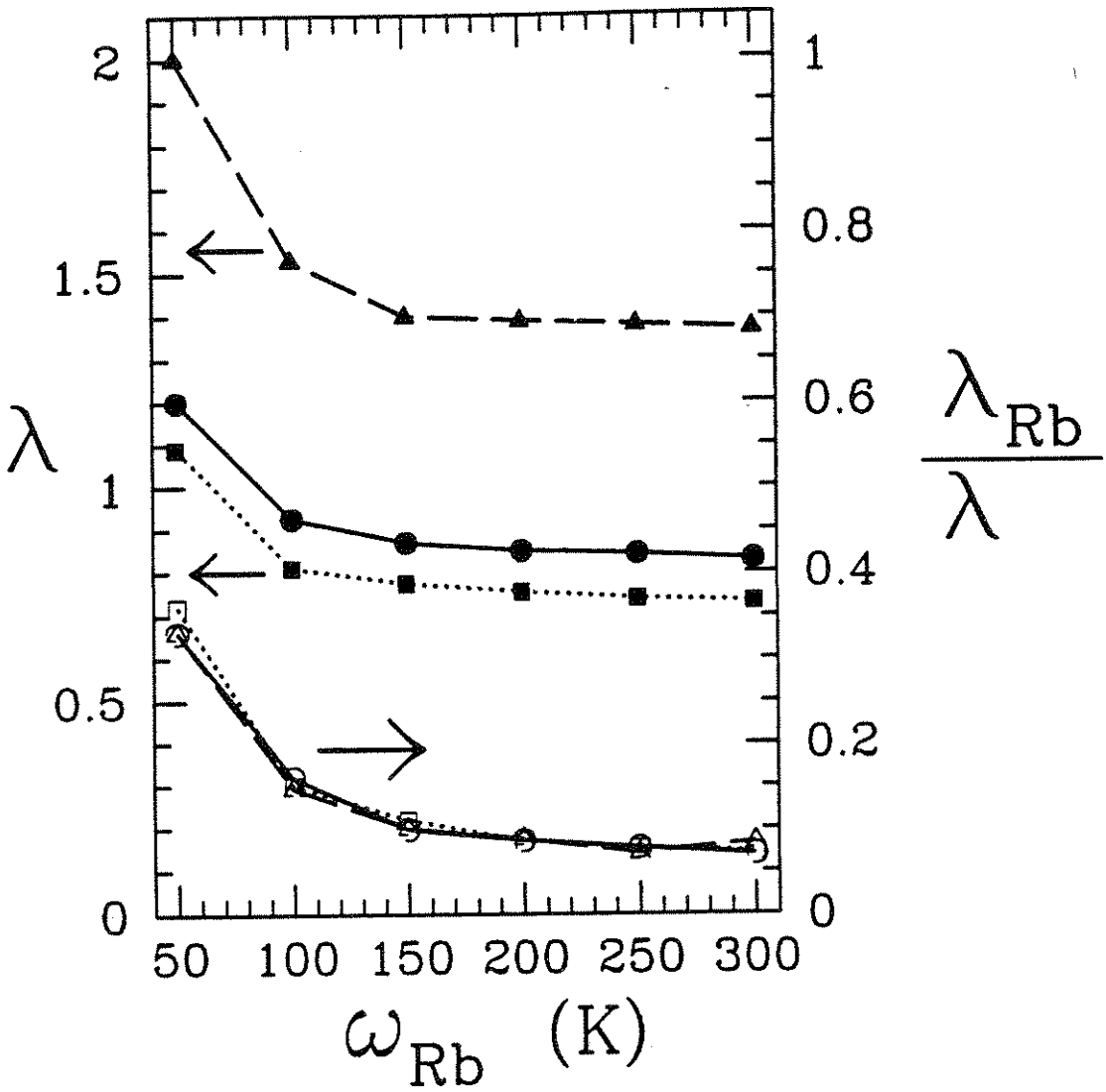

FIG. 8.5 Total electron-phonon coupling strength λ (upper curves, solid symbols) and upper bound on the ratio of Rb-C_{60} optic mode coupling strength to total coupling λ_{Rb}/λ (lower curves, open symbols) as a function of alkali mode frequency for three theoretical models of the on-ball electron-phonon coupling. The values of λ_{Rb}/λ plotted yield $\alpha_{Rb} = 0.044$, the experimentally determined upper bound on the rubidium isotope effect. Dotted curves refer to the model of Varma et al.[3] which has the fitted value $\mu^* = 0.16$. Solid curves refer to the model of Schluter et al.[5] ($\mu^* = 0.17$). Dashed curves refer to the model of Jishi et al.[4] ($\mu^* = 0.23$). (Figure provided by Vin Crespi.)

Ask Vin

modes to T_c is at best small, the contribution of a low frequency alkali mode to λ can be substantial. In contrast to the analytic model, the ratio λ_{Rb}/λ is only weakly dependent on α_C. Decreasing (increasing) the carbon isotope effect exponent to 0.2 (0.4) results in significantly increased (decreased) values of λ and μ^*, but the ratio λ_{Rb}/λ decreases (increases) by only 10%. This reduced sensitivity to α_C is due to the great disparity between the alkali and carbon phonon frequencies. Modifying the electron-phonon coupling spectrum by the addition of substantial coupling to a low-frequency librational mode at 50 K[8] yields a limit on λ_{Rb}/λ roughly 10% larger. In all cases, removal of the maximal allowed alkali-C_{60} optic mode contribution to the coupling function results in a reduction in T_c of 1 - 4 K, indicating that the alkali modes make at most a minor contribution to T_c.

Although the estimated uncertainty in T_c yields a value of isotope exponent consistent with $\alpha_{Rb} = 0$, the actual data points hint at a small inverse isotope effect. An inverse isotope effect is well known for hydrogen at the octahedral interstitial sites of the fcc Pd lattice[26]; it has been interpreted within the framework of anharmonic phonons[27]. Anharmonicity of the alkali vibration in the A_3C_{60} system could conceivably depress or even invert the isotopic signature of the alkali modes, weakening the limit on λ_{Rb}/λ.

In summary, we have made precise measurements of T_c in isotopically substituted Rb_3C_{60} which yield a null result for the rubidium isotope effect in Rb_3C_{60}. This result puts stringent limits on the possible contributions of alkali-C_{60} optic phonons to the superconductivity.

References

1. S. Chakravarty, M. P. Gelfand and S. Kivelson, Science **254**, 970 (1991).
2. S. Chakravarty, S. A. Kivelson, M. K. Salkola, *et al.*, Science **256**, 1306 (1992).
3. C. M. Varma, J. Zaanen and K. Raghavachari, Science **254**, 989 (1991).
4. R. A. Jishi and M. S. Dresselhaus, Phys. Rev. B **45**, 2597 (1992).
5. M. Schluter, M. Lannoo, M. Needels, *et al.*, Phys. Rev. Lett. **68**, 526 (1992).
6. F. C. Zhang, M. Ogata and T. M. Rice, Phys. Rev. Lett. **48**, 3452 (1991).
7. G. H. Chen, Y. J. Guo, N. Karasawa, *et al.*, Phys. Rev. B **48**, 13959 (1993).
8. I. I. Mazin, O. V. Dolgov, A. Golubov, *et al.*, Phys. Rev. B **47**, 538 (1993).
9. V. H. Crespi, J. G. Hou, X.-D. Xiang, *et al.*, Phys. Rev. B **46**, 12064 (1992). A crude estimate of the electron-phonon coupling strength for intermolecular translational modes can be found here.
10. T. W. Ebbesen, J. S. Tsai, K. Tanigaki, *et al.*, Physica C **203**, 163 (1992).
11. C.-C. Chen and C. M. Lieber, J. Am. Chem. Soc. **114**, 3141 (1992).
12. A. P. Ramirez, A. R. Kortan, M. J. Rosseinsky, *et al.*, Phys. Rev. Lett. **68**, 1058 (1992).
13. T. W. Ebbesen, J. S. Tsai, K. Tanigaki, *et al.*, Nature **355**, 620 (1992).
14. A. A. Zakhidov, K. Imaeda, D. M. Petty, *et al.*, Phys. Lett. A **164**, 355 (1992).
15. Auban-Senzier, G. Quirion, D. Jerome, *et al.*, Synth. Met. **56**, 3027 (1993).
16. C.-C. Chen and C. M. Lieber, Science **259**, 655 (1993).
17. O. Zhou, G. B. M. Vaughan, Q. Zhu, *et al.*, Science **255**, 833 (1992).
18. X.-D. Xiang, J. G. Hou, G. Briceno, *et al.*, Science **256**, 1190 (1992).
19. G. Sparn and J. D. Thompson, Phys. Rev. Lett. **68**, 1228 (1992).
20. X.-D. Xiang, J. G. Hou, V. H. Crespi, *et al.*, Nature **361**, 54 (1993).
21. H. Holloway, K. C. Hass, M. A. Tamor, *et al.*, Phys. Rev. B **44**, 7123 (1991).
22. D. A. Neumann, J. R. D. Copley, D. Reznik, *et al.*, , . unpublished.
23. W. L. McMillan, Phys. Rev. **167**, 331 (1968).

24. J. W. White, G. Lindsell, L. Pang, *et al.*, Chem. Phys. Lett. **191**, 92 (1992).

25. W. Zhang, H. Zheng and K. H. Bennemann, Solid State Comm. **82**, 679 (1992).

26. B. Stritzker and W. Buckel, Zeitschrif für Physik **257**, 1 (1972).

27. V. H. Crespi and M. L. Cohen, Solid State Comm. **83**, 427 (1992).

Appendix A

Calculation of the surface CDW structure in blue bronze

We have calculated the projection of the CDW onto the cleavage plane in order to compare the CDW periodicity to the observed periodicity of our STM images. The cleavage plane in blue bronze is defined by the **b** and [102] crystal axes. Our starting point is the CDW wave vector which from Eq. (3.1) is

$$\mathbf{q}^{\pm}_{CDW} = \pm \delta \mathbf{b}^* + 0.5\mathbf{c}^* \quad , \tag{A.1}$$

where δ = 0.737 (0.74) for $K_{0.3}MoO_3$ ($Rb_{0.3}MoO_3$). Projection of the CDW wave vector onto **b** gives

$$\begin{aligned} \mathbf{q}^{\pm}_{CDW} \cdot \frac{\mathbf{b}}{|\mathbf{b}|} &= \left(\pm \delta \mathbf{b}^* + 0.5\mathbf{c}^*\right) \cdot \frac{\mathbf{b}}{|\mathbf{b}|} \\ &= \pm \delta \mathbf{b}^* \cdot \frac{\mathbf{b}}{|\mathbf{b}|} = \pm \frac{2\pi\delta}{|\mathbf{b}|} \quad , \end{aligned} \tag{A.2}$$

while projection of the CDW wave vector onto [102] gives

$$\begin{aligned} \mathbf{q}^{\pm}_{CDW} \cdot \frac{\mathbf{a}+2\mathbf{c}}{|\mathbf{a}+2\mathbf{c}|} &= \left(\pm \delta \mathbf{b}^* + 0.5\mathbf{c}^*\right) \cdot \frac{\mathbf{a}+2\mathbf{c}}{|\mathbf{a}+2\mathbf{c}|} \\ &= \pm \mathbf{c}^* \cdot \frac{\mathbf{c}}{|\mathbf{a}+2\mathbf{c}|} = \pm \frac{2\pi}{|\mathbf{a}+2\mathbf{c}|} \quad . \end{aligned} \tag{A.3}$$

Thus, in the cleavage plane we find

$$\mathbf{q}^{\pm}_{project} = 2\pi \left(\frac{\pm\delta}{|\mathbf{b}|} \frac{\mathbf{b}}{|\mathbf{b}|} + \frac{1}{|\mathbf{a}+2\mathbf{c}|} \frac{\mathbf{a}+2\mathbf{c}}{|\mathbf{a}+2\mathbf{c}|} \right) \quad . \tag{A.4}$$

The translation vectors reciprocal to the projected wave vectors are

$$\mathbf{T}^{\pm}_{\text{project}} = \left(\frac{\pm\mathbf{b}}{2\delta} + \frac{\mathbf{a}+2\mathbf{c}}{2}\right) . \tag{A.5}$$

An equivalent basis for the projected CDW translation vectors is

$$\mathbf{T}^{1}_{\text{project}} = \left(\frac{\mathbf{b}}{\delta}\right);\ \mathbf{T}^{2}_{\text{project}} = \left(\frac{\mathbf{b}}{2\delta} + \frac{\mathbf{a}+2\mathbf{c}}{2}\right) . \tag{A.6}$$

Finally, the vector magnitudes and angle between the vectors are:

$$\begin{aligned} \left|\mathbf{T}^{1}_{\text{project}}\right| &= 10.2\ \text{Å}; \\ \left|\mathbf{T}^{2}_{\text{project}}\right| &= 11.1\ \text{Å}; \quad \theta = 62.6^{\circ} . \end{aligned} \tag{A.7}$$

In Fig. A.1 the CDW surface structure is displayed together with the positions of the "hump" octahedra. The CDW forms a superlattice in the cleavage plane that is commensurate in the [102] direction and nearly commensurate in the **b** direction. In this figure the phase of the CDW with respect to the "hump" octahedra is chosen so that a CDW maximum (open circle) coincides with a "hump" octahedron (closed circle) in the lower-left region of the figure. The choice of the CDW phase is arbitrary in the **b** direction since the CDW is commensurate and the phase is chosen so that commensurability is obvious; however, the phase of the CDW may be offset in the [102] direction so that CDW maxima may not coincide with "hump" octahedra.

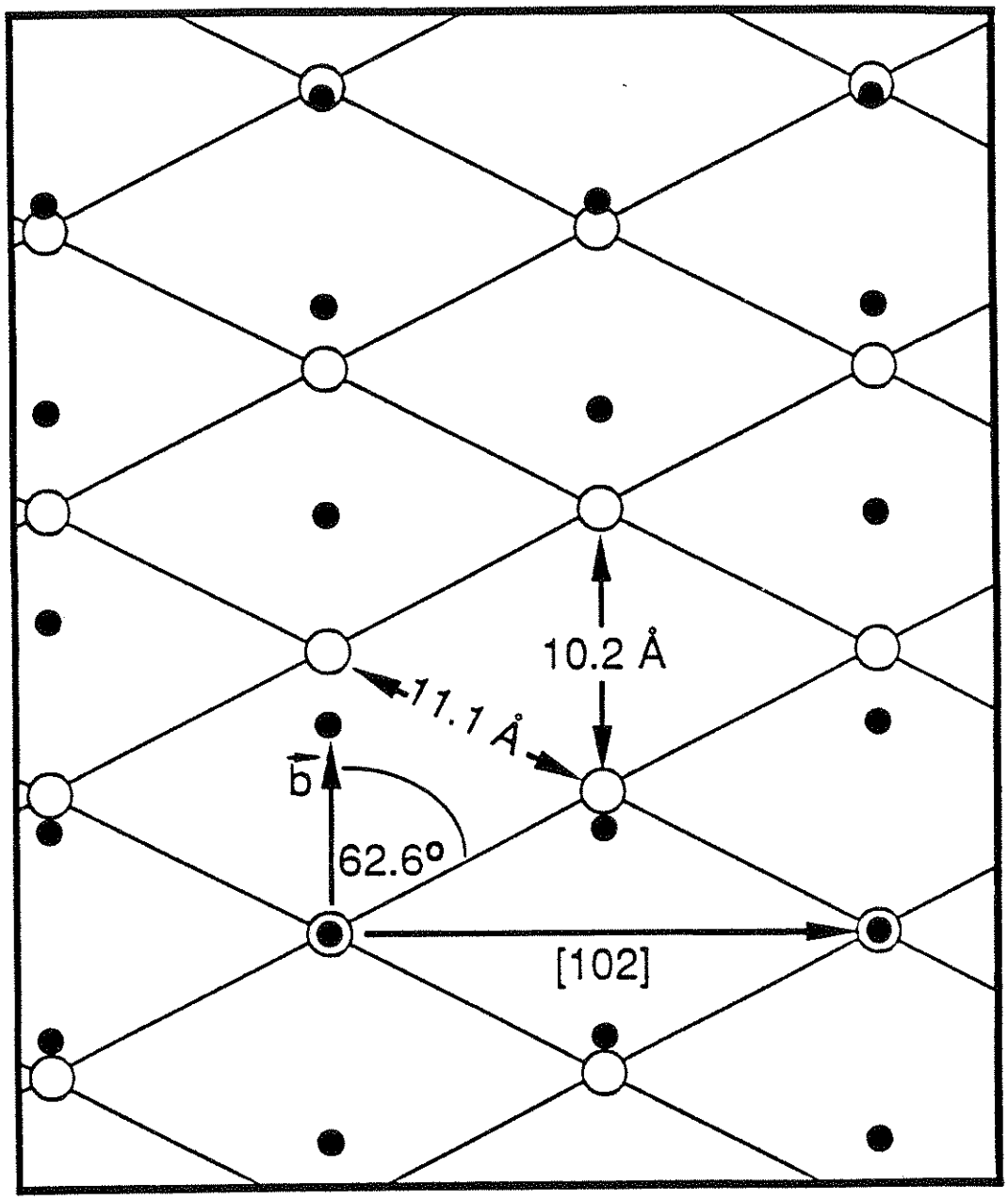

FIG. A.1 The incommensurate charge-density wave of $K_{0.3}MoO_3$ in the **b** and [102] plane calculated from x-ray diffraction and neutron-scattering data. The solid lines indicate the CDW wave front with a wavelength of 9.07 Å, and the open circles indicate the CDW maxima. Closed circles indicate the positions of the "hump" Mo-O octahedra. (Figure provided by Ruth Thomson)

Appendix B

Construction of CDW amplitude and phase modulation envelope from Fourier transforms

The amplitude and phase domain modulation envelopes are extracted from the Fourier transforms (FTs) of the real space STM image. The envelopes shown in Figs. 5.5(a), 5.5(b), 5.7(a), and 5.7(b) reflect the modulation of a single CDW fundamental Fourier component induced by neighboring satellites. The procedure used to obtain and display the modulation envelope is described below.

The contribution to the real space image of a single CDW Fourier component and its associated satellites, $\rho(\mathbf{r})$, may be expressed as

$$\rho(\mathbf{r}) = \rho_o \exp(i\mathbf{k}_o \cdot \mathbf{r}) + \sum_n \rho_n \exp(i\mathbf{k}_n \cdot \mathbf{r}) \ , \tag{B.1}$$

where ρ_o refers to the CDW fundamental Fourier component and ρ_n refers to the satellites. Here ρ_i is a complex number that represents the amplitude and phase of the Fourier component, $\mathbf{k}_i$ is the wave vector, and $\mathbf{r}$ is the real space position. The values of ρ_i and $\mathbf{k}_i$ are obtained directly from the FT of the STM image. Equation (B.1) may be rewritten as

$$\rho(\mathbf{r}) = \rho_o \exp(i\mathbf{k}_c \cdot \mathbf{r}) \left(\exp[i(\mathbf{k}_o - \mathbf{k}_c) \cdot \mathbf{r}] \left(1 + \sum_n \frac{\rho_n}{\rho_o} \exp[i(\mathbf{k}_n - \mathbf{k}_o) \cdot \mathbf{r}] \right) \right) \ , \tag{B.2}$$

where $\mathbf{k}_c$ is the commensurate wave vector and the term in large parentheses is the modulation envelope, $M(\mathbf{r})$. We may express $M(\mathbf{r})$ as

$$M(\mathbf{r}) = A(\mathbf{r}) \exp[i\phi(\mathbf{r})] \ , \tag{B.3}$$

where $M(\mathbf{r})$ and $\phi(\mathbf{r})$ are the amplitude and phase of the modulation envelope. Thus

$$A(\mathbf{r}) = |M(\mathbf{r})| \tag{B.4}$$

and

$$\phi(\mathbf{r}) = \arctan\left\{\frac{\mathrm{Im}\,[M(\mathbf{r})]}{\mathrm{Re}\,[M(\mathbf{r})]}\right\} . \tag{B.5}$$

The functions $A(\mathbf{r})$ and $\phi(\mathbf{r})$ are plotted in Figs. 5.5(a), 5.5(b), 5.7(a), and 5.7(b) for a specifically chosen direction of $\mathbf{r}$. The set of wave vectors $\mathbf{k}_n$ - $\mathbf{k}_o$ are the domain wave vectors. We choose the direction of $\mathbf{r}$ to make a 30° angle with respect to the domain wave vector which connects the CDW fundamental peak to its strongest satellite. The sense of the 30° angle is such that $\mathbf{r}$ is nearly antiparallel to $\mathbf{k}_o$. With this direction chosen for $\mathbf{r}$, the envelopes plotted in Figs. 5.5(a), 5.5(b), 5.7(a), and 5.7(b) reflect the modulation of the CDW along a line parallel to a row of domains, and this line is roughly parallel to the CDW direction of propagation.

Appendix C

Derivation of domain period formula

Here we derive an expression for the beat period between the atomic lattice and the CDW in the NC phase. The beat wave vector is the difference between a reciprocal lattice vector and a sum of CDW wave vectors which nearly equals the reciprocal lattice vector. The beat period is the reciprocal of the magnitude of the beat wave vector.

In Fig. C.1(a) we illustrate the commensurate case. Here $\mathbf{a}^*$ is a reciprocal lattice vector and $\mathbf{k}_c^1$ and $\mathbf{k}_c^3$ are commensurate CDW wave vectors. In the commensurate case three conditions are satisfied: $3\mathbf{k}_c^1 - \mathbf{k}_c^3 = \mathbf{a}^*$, $|\mathbf{k}_c^1| = |\mathbf{k}_c^3|$, and $\mathbf{k}_c^3$ is rotated 120° counterclockwise with respect to $\mathbf{k}_c^1$. In the NC phase the first condition is no longer satisfied although the second two are.

In the NC case, illustrated in Fig. C.1(b), $\mathbf{k}^1$ and $\mathbf{k}^3$ are NC phase CDW wave vectors, $\mathbf{k}_B$ is the beat vector, $\mathbf{s} = 3\mathbf{k}^1 - \mathbf{k}^3$, and $\delta\Phi$ is the deviation angle of $\mathbf{k}^1$ from the commensurate angle. By similarity of triangles in the commensurate and NC cases,

$$|\mathbf{s}| = |\mathbf{a}^*| \frac{\mathbf{k}^1}{\mathbf{k}_c^1} \ . \tag{C.1}$$

By the law of cosines

$$|\mathbf{k}_B| = \sqrt{|\mathbf{a}^*|^2 + |\mathbf{s}|^2 - 2|\mathbf{a}^*||\mathbf{s}|\cos(\delta\Phi)} \ . \tag{C.2}$$

Defining ε as

$$(1+\varepsilon) = \frac{|\mathbf{k}^1|}{|\mathbf{k}_c^1|} = \frac{\lambda_c}{\lambda} = 1 + \frac{\delta\lambda}{\lambda} \ , \tag{C.3}$$

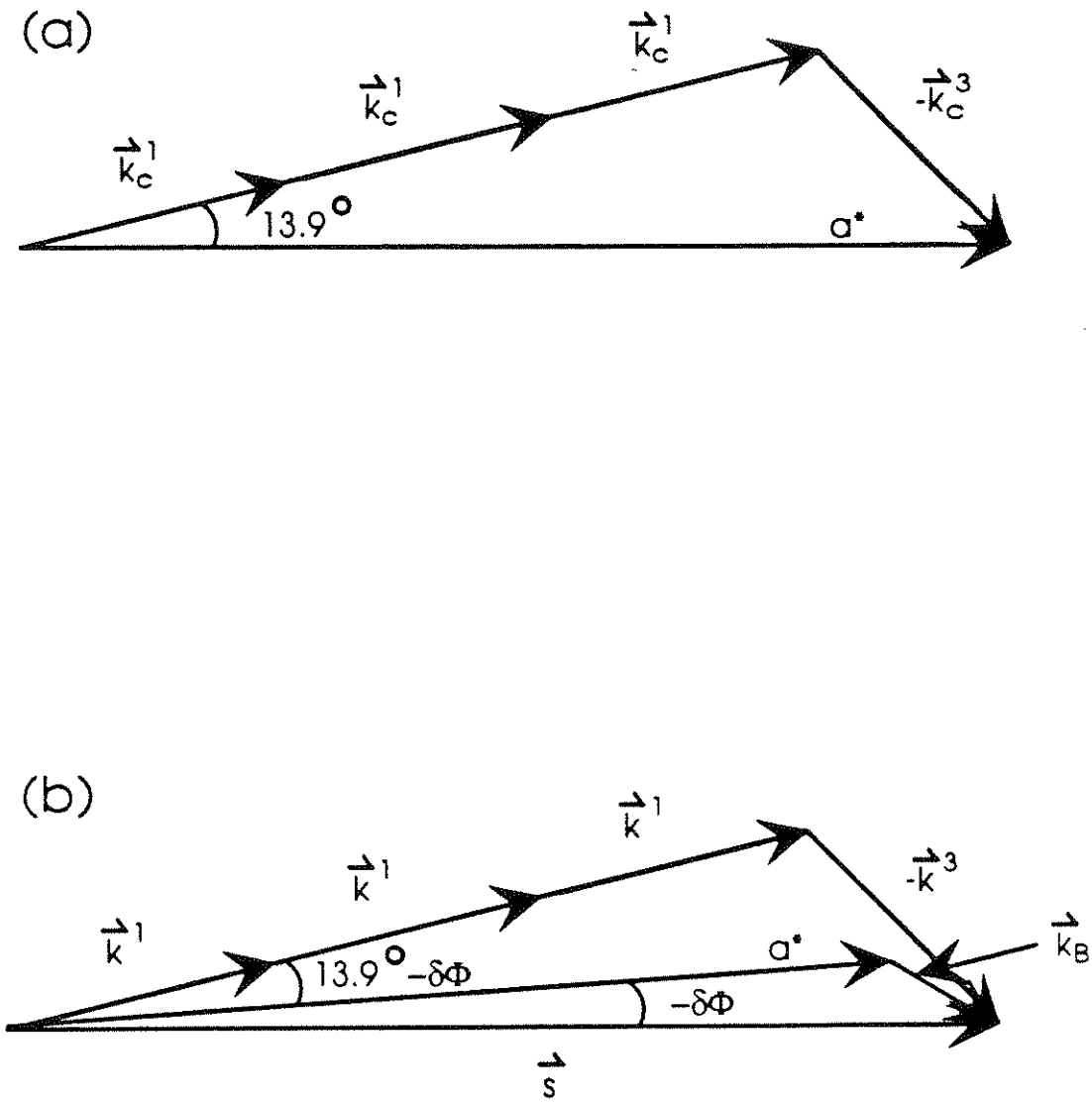

FIG. C.1 (a) Schematic of the relationship between the CDW wave vectors and the reciprocal lattice vectors in the commensurate case. (b) Schematic of the relationship between the CDW wave vectors, the reciprocal lattice vectors, and the domain wave vector in the nearly commensurate case.

XBL 934-435

where λ_c is the commensurate CDW period and λ is the observed NC phase CDW period and $\delta\lambda = \lambda_c - \lambda$, we may write

$$|\mathbf{k}_B| = |\mathbf{a}^*|\sqrt{1 + (1+\varepsilon)^2 - 2(1+\varepsilon)\cos(\delta\Phi)} \ , \tag{C.4}$$

which simplifies to

$$|\mathbf{k}_B| = |\mathbf{a}^*|\sqrt{\varepsilon^2 + (1+\varepsilon)\left[2\sin\left(\frac{\delta\Phi}{2}\right)\right]^2} \ . \tag{C.5}$$

Finally,

$$\text{Beat Period} = \frac{a_o}{\sqrt{\varepsilon^2 + (1+\varepsilon)\left[2\sin\left(\frac{\delta\Phi}{2}\right)\right]^2}} \ , \tag{C.6}$$

where a_o is the atomic lattice constant. Upon making the approximations $(1 + \varepsilon) \approx 1$, since $\varepsilon << 1$, and $\sin(\delta\Phi) \approx \pi\delta\Phi/360$, since $\delta\Phi/2 \approx 1^\circ$, we obtain Eq. (5.1):

$$\text{Domain Period} = \frac{a_o}{\sqrt{\left(\frac{2\pi\delta\Phi}{360}\right)^2 + \left(\frac{\delta\lambda}{\lambda}\right)^2}} \ . \tag{C.7}$$

Appendix D

Evaluation of the structure factor for 1T-TaS_2 in the I phase

D.1 Preliminaries

Here we present a detailed evaluation of the structure factor from chapter 7, Eq. (7.3), at three wave vectors, $\mathbf{a}^*$, $\mathbf{q}_{cdw1}$, and $\mathbf{q}_{cdw2}$. For simplicity, in the following calculation we use

$$\mathbf{q}_{cdw1} = 1.282\mathbf{a}^* + 1/3\mathbf{c}^* \text{ and} \tag{D.1a}$$

$$\mathbf{q}_{cdw2} = 1.436\mathbf{a}^* + 1/3\mathbf{c}^* \ . \tag{D.1b}$$

These values differ slightly from those stated in chapter 7. In Eqs. (D.1a) and (D.1b) we have ignored the small $\mathbf{b}^*$ components of $\mathbf{q}_{cdw1}$ and $\mathbf{q}_{cdw2}$ and increased the $\mathbf{a}^*$ component of $\mathbf{q}_{cdw2}$ by $0.004\mathbf{a}^*$ compared to the values given in chapter 7. The increase of $0.004\mathbf{a}^*$ makes the value of $\mathbf{q}_{cdw2}$ precisely consistent with the value of $\mathbf{q}_{cdw1}$ in Eq. (D.1a). (The values given for $\mathbf{q}_{cdw1}$ and $\mathbf{q}_{cdw2}$ in chapter 7 are consistent with each other to within our experimental uncertainty, however.) The difference between the values for $\mathbf{q}_{cdw1}$ and $\mathbf{q}_{cdw2}$ given above and the values quoted in chapter 7 will produce no significant error in the dot product evaluations that follow. We restate the structure factor formula, [Eq. (7.3)], in a slightly different form,

$$\begin{aligned} S(\mathbf{q}) = \sum f_i(\mathbf{q}) \exp[i(\tau_i \bullet \mathbf{G} + n_1\phi_{i1} + n_2\phi_{i2} + n_3\phi_{i3})] \\ \times J_{n1}(\mathbf{q}\bullet\mathbf{A}_{i1}) J_{n2}(\mathbf{q}\bullet\mathbf{A}_{i2}) J_{n3}(\mathbf{q}\bullet\mathbf{A}_{i3}) \\ \times TF(n_1,n_2,n_3) \end{aligned} \tag{D.2}$$

where $TF(n_1, n_2, n_3)$ is the temperature factor (either PTF or both PTF and ATF) and the other quantities are defined in the discussion following Eq. (7.3).

D.2 Quantities needed to evaluate the structure factor

We require the form factors for Ta and S evaluated at three scattering wave vectors. We use the tables by Crommer et al.[1,2] to calculate form factors including anomolous dispersion corrections. We present our results in Table D.1 with form factor values given in electron units.

Next we require the basis vectors. The unit cell contains one Ta atom and two S atoms. The basis vectors are[3]

$$\tau_{Ta} = \mathbf{0} \text{ and} \tag{D.3a}$$

$$\tau_{S\pm} = \pm(2/3\mathbf{a} + 1/3\mathbf{b} + 1/4\mathbf{c}) \ . \tag{D.3b}$$

Finally, we require the parameters C, A_{ij}, and ϕ_{ij} determined by Chapman and Colella[3-5]. They find $C = 1.8 \times 10^{-3}\ K^{-1}$ and

$$A_{Ta,1} = 0.08593(2/3\mathbf{a} + 1/3\mathbf{b}), \tag{D.4a}$$

$$A_{Ta,2} = -0.08593(1/3\mathbf{a} + 2/3\mathbf{b}), \tag{D.4b}$$

$$A_{Ta,3} = 0.08593(1/3\mathbf{b} - 1/3\mathbf{a}), \text{ and} \tag{D.4c}$$

$$A_{S\pm,j} = 0.1280\mathbf{c},\ j = 1,2,3 \tag{D.4d}$$

Atom	f(a*)	f(1.282a* + 1/3c*)	f(1.436a* + 1/3c*)
Ta	62.324	58.897	56.670
S	12.055	10.721	10.007

Table D.1 Atomic form factors evaluated at the wave vectors investigated in chapter 7.

where we have converted Chapman and Colella's statement of the A_{ij} from a reciprocal lattice basis set to a real space basis set. The real space basis set is more convenient in the calculations which follow. Chapman and Colella state $\phi_{S\pm,j}$ refered to a cosine modulation, but Eq. (D.2) is developed from a sine modulation for all ϕ_{ij}. After suitable adjustment for this phase difference the values of ϕ_{ij} consistent with Eq. (D.2) are

$$\phi_{Ta,j} = 0^\circ \qquad j = 1,2,3 \tag{D.5a}$$

$$\phi_{S\pm,j} = \pm 146^\circ \qquad j = 1,2,3 \tag{D.5b}$$

D.2 Evaluation of the Bragg (100) peak intensity

Here $\mathbf{q} = \mathbf{a}^*$, $n_1 = n_2 = n_3 = 0$, and $\mathbf{G} = \mathbf{a}^*$. We find it convenient to calculate the contribution to the structure factor of each atom type separately here and in the following sections.

Tantalum

$$S_{Ta}(\mathbf{a}^*) = f_{Ta}(\mathbf{a}^*)\exp[i(\tau_{Ta}\bullet\mathbf{a}^*)]J_0(\mathbf{a}^*\bullet\mathbf{A}_{Ta,1})J_0(\mathbf{a}^*\bullet\mathbf{A}_{Ta,2})J_0(\mathbf{a}^*\bullet\mathbf{A}_{Ta,3}) \times TF(0,0,0). \quad (D.6)$$

Here we explicitly evaluate each of the dot products.

$$\tau_{Ta}\bullet\mathbf{a}^* = \mathbf{0}\bullet\mathbf{a}^* = 0$$

$$\mathbf{a}^*\bullet\mathbf{A}_{Ta,1} = \mathbf{a}^*\bullet(0.08593)(2/3\mathbf{a} + 1/3\mathbf{b}) = (0.08593)(2/3)(2\pi) = 0.360$$

$$\mathbf{a}^*\bullet\mathbf{A}_{Ta,2} = \mathbf{a}^*\bullet(-0.08593)(1/3\mathbf{a} + 2/3\mathbf{b}) = (-0.08593)(1/3)(2\pi) = -0.180$$

$$\mathbf{a}^*\bullet\mathbf{A}_{Ta,3} = \mathbf{a}^*\bullet(0.08593)(1/3\mathbf{b} - 1/3\mathbf{a}) = (0.08593)(-1/3)(2\pi) = -0.180$$

$$S_{Ta}(\mathbf{a}^*) = (62.324)\exp[0]J_0(0.360)[J_0(-0.180)]^2TF(0,0,0)$$
$$= 59.352TF(0,0,0).$$

Sulfur

$$S_{S\pm}(\mathbf{a}^*) = f_S(\mathbf{a}^*)\exp[i(\tau_{S\pm}\bullet\mathbf{a}^*)]J_0(\mathbf{a}^*\bullet\mathbf{A}_{S\pm,1})J_0(\mathbf{a}^*\bullet\mathbf{A}_{S\pm,2})J_0(\mathbf{a}^*\bullet\mathbf{A}_{S\pm,3}) \times TF(0,0,0). \quad (D.7)$$

The dot products are

$$\tau_{S\pm}\bullet\mathbf{a}^* = \pm(2/3\mathbf{a} + 1/3\mathbf{b} + 1/4\mathbf{c})\bullet\mathbf{a}^* = \pm 240^\circ$$

$$\mathbf{a}^*\bullet\mathbf{A}_{S\pm j} = \mathbf{a}^*\bullet(0.1280)\mathbf{c} = 0 \qquad \text{for } j = 1,2,3.$$

$$S_{S+}(\mathbf{a}^*) \pm S_{S-}(\mathbf{a}^*) = (12.055)(2)\cos[240^\circ][J_0(0)]^3 TF(0,0,0)$$

$$= -12.055 TF(0,0,0).$$

Total

$$S_{TOT}(\mathbf{a}^*) = (59.352 - 12.055)TF(0,0,0) = 47.297 TF(0,0,0)$$

$$I(\mathbf{a}^*) = 2{,}237.0[TF(0,0,0)]^2. \qquad \text{(D.8)}$$

The dot product evaluations in following sections will not be shown.

D.4 Evaluation of the q_{cdw1} peak intensity

Here $\mathbf{q} = 1.282\mathbf{a}^* + 1/3\mathbf{c}^*$, $n_1 = 1$, $n_2 = n_3 = 0$, and $\mathbf{G} = \mathbf{a}^*$.

Tantalum

$$S_{Ta}(q_{cdw1}) = f_{Ta}(q_{cdw1})\exp[i(\tau_{Ta}\bullet\mathbf{a}^* + \phi_{Ta,1})] \times J_1(q_{cdw1}\bullet A_{Ta,1})J_0(q_{cdw1}\bullet A_{Ta,2})J_0(q_{cdw1}\bullet A_{Ta,3}) \times TF(1,0,0). \quad (D.9)$$

$$S_{Ta}(q_{cdw1}) = (58.897)\exp[0]J_1(0.461)[J_0(-0.231)]^2TF(1,0,0) = 12.867TF(1,0,0).$$

Sulfur

$$S_{S\pm}(q_{cdw1}) = f_S(q_{cdw1})\exp[i(\tau_{S\pm}\bullet\mathbf{a}^* + \phi_{S\pm,1})] \times J_1(q_{cdw1}\bullet A_{S\pm,1})J_0(q_{cdw1}\bullet A_{S\pm,2})J_0(q_{cdw1}\bullet A_{S\pm,3}) \times TF(1,0,0). \quad (D.10)$$

$$S_{S+}(q_{cdw1}) + S_{S-}(q_{cdw1}) = (10.721)(2)\cos(386^\circ)J_1(0.268)[J_0(0.268)]^2 \times TF(1,0,0). = 2.469TF(1,0,0).$$

Total

$$I(q_{cdw1}) = 235.19[TF(1,0,0)]^2. \quad (D.11)$$

D.5 Evaluation of the $\mathbf{q}_{cdw2}$ peak intensity

Here $\mathbf{q} = 1.436\mathbf{a}^* + 1/3\mathbf{c}^*$, $n_1 = -2$, $n_2 = n_3 = 0$, and $\mathbf{G} = 2\mathbf{a}^* + \mathbf{c}^*$.

Tantalum

$$S_{Ta}(\mathbf{q}_{cdw2}) = f_{Ta}(\mathbf{q}_{cdw2})\exp\{i[\tau_{Ta}\bullet(2\mathbf{a}^* + \mathbf{c}^*) - 2\phi_{Ta,1}]\} \times J_{-2}(\mathbf{q}_{cdw2}\bullet\mathbf{A}_{Ta,1})J_0(\mathbf{q}_{cdw2}\bullet\mathbf{A}_{Ta,2})J_0(\mathbf{q}_{cdw2}\bullet\mathbf{A}_{Ta,3}) \times TF(-2,0,0). \quad (D.12)$$

$$S_{Ta}(\mathbf{q}_{cdw2}) = (56.670)\exp\{0\}J_{-2}(0.517)[J_0(-0.258)]^2TF(-2,0,0) = 1.790TF(-2,0,0).$$

Sulfur

$$S_{S\pm}(\mathbf{q}_{cdw2}) = f_S(\mathbf{q}_{cdw2})\exp\{i[\tau_{S\pm}\bullet(2\mathbf{a}^* + \mathbf{c}^*) - 2\phi_{S\pm,1}]\} \times J_{-2}(\mathbf{q}_{cdw2}\bullet\mathbf{A}_{S\pm,1})J_0(\mathbf{q}_{cdw2}\bullet\mathbf{A}_{S\pm,2})J_0(\mathbf{q}_{cdw2}\bullet\mathbf{A}_{S\pm,3}) \times TF(-2,0,0). \quad (D.13)$$

$$S_{S+}(\mathbf{q}_{cdw2}) + S_{S-}(\mathbf{q}_{cdw2}) = (10.007)(2)\cos(278^\circ)J_{-2}(0.268)[J_0(0.268)]^2 \times TF(-2,0,0). = 0.02398TF(-2,0,0).$$

Total

$$I(\mathbf{q}_{cdw2}) = 3.293[TF(-2,0,0)]^2. \quad (D.14)$$

D.6 Evaluation of relative peak intensities

$$I(q_{cdw1})_{calc} = I(q_{cdw1})/I(100) = 0.1051[TF(1,0,0)/TF(0,0,0)]^2 \quad (D.15a)$$

$$I(q_{cdw2})_{calc} = I(q_{cdw2})/I(100) = 1.472 \times 10^{-3}[TF(-2,0,0)/TF(0,0,0)]^2. \quad (D.15b)$$

For the "Calculated with PTF alone" case described by Eq. (7.3)

$$TF(n_1,n_2,n_3) = \exp[-C(n_1^2 + n_2^2 + n_3^2)T].$$

Thus,

$TF(0,0,0) = 1,$

$TF(1,0,0) = \exp[-CT]$, and

$TF(-2,0,0) = \exp[-4CT]$.

At T = 363 K $\exp[-2CT] = 0.27$, $[TF(1,0,0)]^2 = 0.27$, and $[TF(-2,0,0)]^2 = 0.005314$. The temperature factor reduces the intensity of the first-order satellite by a factor of about four and the intensity of the second-order satellite by a factor of nearly 200. Thus,

$$I(q_{cdw1})_{calc} = 2.84 \times 10^{-2}, \quad (D.16a)$$

$$I(q_{cdw2})_{calc} = 7.83 \times 10^{-6}, \quad (D.16b)$$

and so using the experimental values of the intensty from Table 7.1 we find

$$I(\mathbf{q}_{cdw1})_{expt}/I(\mathbf{q}_{cdw1})_{calc} = 1.08 \text{ and} \tag{D.17a}$$

$$I(\mathbf{q}_{cdw2})_{expt}/I(\mathbf{q}_{cdw2})_{calc} = 35.1\ . \tag{D.17b}$$

For the "Calculated with PTF and ATF" case from Eqs. (7.4) -(7.7)

$$TF(n,0,0) = \exp[-n^2 W_\phi(T)] \times \exp[\ |n|\ (\ |n|\ - 1) W_A(T)].$$

$$TF(0,0,0) = 1,$$

$$TF(1,0,0) = \exp[-CT], \text{ and}$$

$$TF(-2,0,0) = \exp[-3.507CT].$$

Thus, $[TF(1,0,0)]^2 = 0.27$ and $[TF(-2,0,0)]^2 = 0.010132$. The temperature factor reduces the intensity of the first-order satellite by a factor of about four and the intensity of the second-order satellite by a factor of nearly 100. Thus,

$$I(\mathbf{q}_{cdw1})_{calc} = 2.84 \times 10^{-2}\ , \tag{D.18a}$$

$$I(\mathbf{q}_{cdw2})_{calc} = 1.49 \times 10^{-5}\ , \tag{D.18b}$$

and so using the experimental values of the intensty from table 7.1 we find

$$I(\mathbf{q}_{cdw1})_{expt}/I(\mathbf{q}_{cdw1})_{calc} = 1.08 \text{ and} \tag{D.19a}$$

$$I(\mathbf{q}_{cdw2})_{expt}/I(\mathbf{q}_{cdw2})_{calc} = 18.4\ . \tag{D.19b}$$

References

1. D. T. Crommer and J. B. Mann, Acta Cryst. **A24**, 321 (1968).

2. D. T. Crommer and D. Liberman, J. Chem. Phys. **53**, 1891 (1970).

3. C. B. Scruby, P. M. Willaims and G. S. Parry, Philos. Mag. **31**, 255 (1975).

4. L. D. Chapman and R. Collela, Phys. Rev. Lett. **52**, 652 (1984).

5. L. D. Chapman and R. Colella, Phys. Rev. B **32**, 2233 (1985).

Appendix E

Calculation of the temperature factor for a gapped phason dispersion relation and implications for CDW modulation in the I phase

E.1 Dispersion relations

Before calculation of $W_\phi(T)$ and $W_A(T)$ can proceed, one must specify the phason and ampliton dispersion relations. In Giuliani and Overhauser's theory[1] they are given by

$$[\omega_A(q)]^2 = \omega_{ph}^2[1 + F(q)] \tag{E.1a}$$

$$[\omega_\phi(q)]^2 = \omega_{ph}^2[1 - F(q)] \tag{E.1b}$$

where ω_{ph} is the frequency of the phonon at the CDW wave vector before the CDW distortion occurs. If the phonon dispersion relation is linear up to the CDW wave vector, before the CDW distortion, then $\omega_{ph} = \omega_D|Q_{CDW}|/|a^*|$ where $|Q_{CDW}|$ is the magnitude of the in-layer CDW wave vector and ω_D is the Debye frequency. Hsieh and Colella[2] report ω_D = 170 K which leads to ω_{ph} = 48 K. The coupling function, F(q), is not known but Giuliani and Overhauser assumed a functional form that produces a linear phason dispersion. They chose that form because they assumed CDW translational invariance which should produce a linear phason dispersion at small q. Exact translational CDW invariance should hold only for perfectly rigid incommensurate CDW however.

A few general properties of F(q) are evident from examination of Eq. (E.1b). First, F(q) must be an even function of q. Next we note that the range of q should be limited to some maximum wave vector, q_{max}, beyond which F(q) = 0. The phonon dispersion, $\omega_{ph}(k)$, is reconstructed into phason and ampliton branches at wave vectors k = Q_{CDW} + q where $-q_{max} < q < q_{max}$. Outside this range the phonon dispersion remains

unaltered by the CDW distortion. This means $\omega_\phi(q_{max}) \approx \omega_{ph}$. Thus $F(q_{max}) \approx 0$. ω_{ph} plays the role of the phason analog of the Debye frequency. Therefore the phason Debye temperature $\Theta_D = 48$ K.

We assume a general quadratic form for F(q) consistent with the properties discussed above. This leads immediately to

$$[\omega_A(q)]^2 = \omega_{ph}^2[2 - \varepsilon^2 - (v_\phi q/\omega_{ph})^2] \tag{E.2a}$$

$$[\omega_\phi(q)]^2 = \omega_{ph}^2[\varepsilon^2 + (v_\phi q/\omega_{ph})^2] \tag{E.2b}$$

$$(v_\phi q_{max}/\omega_{ph}) = (1 - \varepsilon^2)^{1/2} \tag{E.2c}$$

where $\varepsilon = \omega_o/\omega_{ph}$, ω_o is the phason gap, and v_ϕ is the large wave vector phason velocity.

E.2 Calculation of $W_\phi(T)$

In Giuliani and Overhauser's theory,

$$W_\phi(T) = \frac{1}{8} \sum_q |\delta\phi_q|^2 \coth\left(\frac{\hbar\omega_\phi(q)}{2KT}\right) \tag{E.3a}$$

$$\delta\phi_q \propto \left[\frac{1}{\omega_\phi(q)}\right]^{\frac{1}{2}} \tag{E.3b}$$

where $\delta\phi_q$ is the amplitude of the phason mode of wave vector q. In the high temperature limit (since for the I phase T > 353 K and so $T >> \Theta_D$),

$$W_\phi(T) \propto T\sum_q \left[\frac{1}{\omega_\phi(q)}\right]^2 \propto T\int_0^{q_{max}} \frac{q^2dq}{\varepsilon^2 + \left(\frac{v_\phi q}{\omega_{ph}}\right)^2}. \qquad \text{(E.4)}$$

Finally,

$$W_\phi(T) = CTf(\varepsilon) \qquad \text{(E.5a)}$$

$$f(\varepsilon) = \int_0^{\sqrt{1-\varepsilon^2}} \frac{x^2dx}{\varepsilon^2 + x^2} = \sqrt{1-\varepsilon^2} - \varepsilon \tan^{-1}\left(\frac{\sqrt{1-\varepsilon^2}}{\varepsilon}\right). \qquad \text{(E.5b)}$$

The quantity, $Cf(\varepsilon)$, takes the place of the parameter C measured by Chapman and Colella[3,4]. $f(\varepsilon)$ goes from 1 to 0 as ε goes from 0 to 1. Thus the appearance of a gap diminishes $W_\phi(T)$ and thereby reduces the effect of phasons on CDW peak intensities.

E.3 Calculation of $W_A(T)$

In Giuliani and Overhauser's theory,

$$W_A(T) = \frac{1}{8}\sum_q |\delta A_q|^2 \coth\left(\frac{\hbar\omega_A(q)}{2KT}\right) \qquad \text{(E.6a)}$$

$$\delta A_q \propto \left[\frac{1}{\omega_A(q)}\right]^{\frac{1}{2}} \qquad \text{(E.6b)}$$

where δA_q is the amplitude of the ampliton mode of wave vector q. In the high temperature limit,

$$W_A(T) \propto T\sum_q \left[\frac{1}{\omega_A(q)}\right]^2 \propto T\int_0^{q_{max}} \frac{q^2dq}{2-\varepsilon^2-\left(\frac{v_\phi q}{\omega_{ph}}\right)^2}. \qquad \text{(E.7)}$$

Finally,

$$W_A(T) = CTg(\varepsilon) \qquad \text{(E.8a)}$$

$$g(\varepsilon) = \int_0^{\sqrt{1-\varepsilon^2}} \frac{x^2dx}{2-\varepsilon^2-x^2} = -\sqrt{1-\varepsilon^2} + \sqrt{2-\varepsilon^2}\,\tanh^{-1}\left(\frac{\sqrt{1-\varepsilon^2}}{\sqrt{2-\varepsilon^2}}\right), \qquad \text{(E.8b)}$$

where $g(\varepsilon)$ goes from 0.2464 to 0 as ε goes from 0 to 1. Surprisingly, the appearance of a gap diminishes $W_A(T)$ and thereby reduces the effect of amplitions on CDW peak intensities, even though the gap reduces ampliton frequency. The gap also reduces the phase space allowed for amplitons (as well as phasons) and this more than compensates for the lowered ampliton frequency.

E.4 Comparison of x-ray data with the revised $W_\phi(T)$ and $W_A(T)$

We wish to determine the parameter ε such that $I(q_{cdw1})_{calc} = I(q_{cdw1})_{expt}$ and $I(q_{cdw2})_{calc} = I(q_{cdw2})_{expt}$. Using the experimental values in table 7.1, the fact that TF(0,0,0) = 1 for any value of ε, and Eqs. (D.15a) and (D.15b), we obtain $[TF(1,0,0)]^2 = 0.291$ and $[TF(-2,0,0)]^2 = 0.187$ experimentally. Our modified version of Giuliani and Overhauser's theory yields

$$[TF(1,0,0)]^2 = \exp[-2CTf(\varepsilon)] \text{ and} \qquad \text{(E.9a)}$$

$$[TF(-2,0,0)]^2 = \exp[-8CTf(\varepsilon)]\exp[4CTg(\varepsilon)] \; . \qquad \text{(E.9b)}$$

Equating the experimental and theoretical temperature factors leads to the requirement that $g(\varepsilon)/f(\varepsilon) = 1.32$. However using Eqs. (E.5b) and (E.8b) we find that $g(\varepsilon)/f(\varepsilon)$ goes monotonically from 0.2464 to 1 as ε goes from 0 to 1. There is no value of ε that allows a fit to the data. Therefore one cannot attribute the excess intensity we observe to a phason dispersion relation of the form in Eq. (E.2b). We have calculated the ratio $W_A(T)/W_\phi(T)$ for other reasonable forms of the function F(q) and in no case does the ratio exceed 1.

References

1. G. F. Giuliani and A. W. Overhauser, Phys. Rev. B **23**, 3737 (1981).

2. S. M. Hsieh and R. Colella, Solid State Comm. **63**, 237 (1987).

3. L. D. Chapman and R. Collela, Phys. Rev. Lett. **52**, 652 (1984).

4. L. D. Chapman and R. Colella, Phys. Rev. B **32**, 2233 (1985).

Appendix F

Derivation of simple analytic bound on λ_{Rb}/λ from bound on α_{Rb}

Our starting point is the definition of the isotope shift exponent α_i, which is

$$\alpha_i = -\frac{d \ln T_c}{d \ln M_i} , \tag{F.1}$$

where M_i is the mass of atomic species i. If one assumes that T_c depends on M_i only through the T_c dependence on the average phonon frequency, one may apply the chain rule to obtain

$$\alpha_i = \frac{1}{2} \frac{d \ln T_c}{d \ln \omega_{log}} \frac{d \ln \omega_{log}^{-2}}{d \ln M_i} , \tag{F.2}$$

where in the McMillan formula for T_c ω_{log} is defined by,

$$\omega_{log} = \exp\left(\sum_n \frac{\lambda_n}{\lambda} \ln \omega_n \right) , \tag{F.3}$$

with λ_n the coupling to the mode with frequency ω_n, and λ is the total coupling. The first logarithmic derivative in Eq. (F.1) is the same for each atomic species and we treat it as a constant which we do not bother to calculate. The second logarithmic derivative is the important factor. Substituting (F.3) into (F.2) yields

$$\alpha_i = \text{const} \sum_n \frac{\lambda_n}{\lambda} \frac{d \ln \omega_n^{-2}}{d \ln M_i} . \tag{F.4}$$

At this point we consider a special case to produce an equation suitable for use in Chapter 8 in analyzing the importance of Rb-C_{60} optic phonons. We assume that the two

types of phonons which may contribute to superconductivity are on-ball carbon modes and Rb-C_{60} optic modes. Furthermore we assume that the frequency of on-ball modes is independent of Rb mass while we allow Rb-C_{60} mode frequencies to depend on both Rb and C_{60} mass. Thus,

$$\alpha_C = \text{const}\left\langle \frac{\lambda_C}{\lambda} \frac{d \ln \omega_C^{-2}}{d \ln M_C} + \frac{\lambda_{Rb}}{\lambda} \frac{d \ln \omega_{Rb}^{-2}}{d \ln M_C} \right\rangle , \tag{F.5}$$

and

$$\alpha_{Rb} = \text{const}\left\langle \frac{\lambda_{Rb}}{\lambda} \frac{d \ln \omega_{Rb}^{-2}}{d \ln M_{Rb}} \right\rangle , \tag{F.6}$$

where ω_C is the on-ball carbon mode frequency and ω_{Rb} is the Rb-C_{60} optic mode frequency. To proceed further, we make specific assumptions about the mass dependencies of the two phonon frequencies,

$$\omega_C^{-2} \propto M_C , \tag{F.7}$$

and

$$\omega_{Rb}^{-2} \propto \frac{3M_{Rb}M_{C_{60}}}{3M_{Rb} + M_{C_{60}}} \equiv M_{eff} , \tag{F.8}$$

where M_{C60} is the mass of a C_{60} molecule and M_{eff} is an effective mass approximation for three Rb vibrating rigidly against a C_{60} molecule. Equation (F.8) should provide a reasonable lower bound on the sensitivity of ω_{Rb}^{-2} to M_{Rb}. This lower bound will enable us to calculate an upper bound on λ_{Rb}/λ from the measurements of α_C and α_{Rb}. Substituting (F.7) and (F.8) into (F.5) and (F.6) yields,

$$\alpha_C = \text{const}\left\{\frac{\lambda_C}{\lambda} + \frac{\lambda_{Rb}}{\lambda}\left[1 - \frac{M_{eff}}{3M_{Rb}}\right]\right\}, \tag{F.9}$$

and

$$\alpha_{Rb} = \text{const}\left\{\frac{\lambda_{Rb}}{\lambda}\frac{M_{eff}}{3M_{Rb}}\right\}. \tag{F.10}$$

Dividing (F.10) by the sum of (F.10) and (F.9) leads to

$$\frac{\alpha_{Rb}}{\alpha_C + \alpha_{Rb}}\frac{3M_{Rb}}{M_{eff}} = \frac{\lambda_{Rb}}{\lambda} \tag{F.11}$$

where we have used the fact that

$$\frac{\lambda_C}{\lambda} + \frac{\lambda_{Rb}}{\lambda} = 1 \ . \tag{F.12}$$

Equation (F.11) is identical to Eq. (8.4).

Here we refute the claim by Ebbesen et al. that their determination that $\alpha_{Rb} < 0.2$ shows that Rb-C_{60} optic phonons play no role in superconductivity. We put into Eq. (G.11)

$$\alpha_{Rb} = 0.2, \alpha_C = 0.3, \text{ and } \frac{3M_{Rb}}{M_{eff}} \approx \frac{4}{3}$$

and find that

$$\frac{\lambda_{Rb}}{\lambda} = \frac{8}{15} .$$

Their result allows over half the total coupling to come from Rb-C_{60} modes. If one assumes $\lambda_C = 0.7$, $\lambda_{Rb} = 0.8$; $\mu^* = 0.125$, $\omega_C = 500$ K, and $\omega_{Rb} = 200$ K, then removal of the Rb-C_{60} mode would reduce T_c from 31 K to 13 K (within the McMillan formula approximation).